Ab-initio studies of phonon mediated photocarrier thermalization in two-dimensional materials

Dissertation
submitted for the degree of

Doctor of Natural Sciences
(Dr.rer.nat.)

by

Yadav, Dinesh

at the

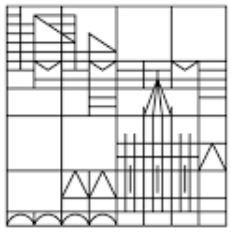

Faculty of Sciences

Department of Physics

Konstanz, 2020

Date of oral examination: May, 11th 2020

1. Referee: Prof. Dr. Fabian Pauly

2. Referee: Prof. Dr. Wolfgang Belzig

Abstract

Van der Waals semiconductor heterostructures could be a platform to harness hot photoexcited carriers in the next generation of optoelectronic and photovoltaic devices. The internal quantum efficiency of hot-carrier devices is determined by the relation between photocarrier extraction and thermalization rates. To improve the performance of the devices based on hot carriers, it will be meaningful to extract the carriers well before thermalization and utilize them to do external work. This requires a deep understanding of the scattering processes through which the hot carriers loose energy. In the case of intrinsic materials, around band edges carriers thermalize mainly via scattering with phonons. We present a theoretical study of photocarrier or hot carrier dynamics in 2D materials namely graphene, transition metal dichalcogenides and cadmium telluride due to electron-phonon interaction. Using the relaxation-time approximation with parameters determined from *ab-initio*, we study the thermalization dynamics over a wide range of excitation energies and temperatures for the photoexcited carriers. Our calculations include contributions arising from all phonon branches in the first Brillouin zone, thus capturing all relevant inter- and intraband carrier transitions due to electron-phonon scattering. Our findings can be inferred by pump-probe spectroscopy.

In the case of graphene, we show that the photocarrier thermalization time changes by orders of magnitude, when the excitation energy is reduced from 1 eV to 100 meV range. Our results are supported by an explicitly solvable model. In detail, the ultrafast thermalization takes place on a femtosecond timescale via optical phonon emission and however, slows down to picoseconds once excitation energy becomes comparable to the optical phonon energy quanta. In the latter regime, thermalization times exhibit a pronounced dependence on temperature. Thanks to the high melting point of graphene we extend our studies up to 2000 K and show that such high temperatures reduce the photocarrier thermalization time through phonon absorption.

In single-layer transition metal dichalcogenides, the photocarrier thermalization times reveal strong dependencies on the peculiarities of the phonon spectrum and the electronic spin-orbit coupling. The lifted spin degeneracy around the band edges suppresses the scattering processes and hence slowing down the thermalization of carriers. Moreover, the hole thermalization time behaves differently in MoS_2 and WSe_2 because spin-orbit interactions differ in these seemingly similar materials. We predict that the internal quantum efficiency of a tunneling van der Waals semiconductor heterostructure depends qualitatively on whether MoS_2 or WSe_2 is used.

For CdTe, we report our theoretical predictions on photocarrier dynamics in an ultimately thin (about 1 nm) CdTe slab and compare with the bulk CdTe crystal. The unit cell of monolayer corresponds to a four-atom-thick slab when the bulk parent crystal in the zinc blende phase is cleaved along the [110] facet. We find that the photocarrier thermalization time is strongly reduced, by one order of magnitude for holes and by three orders of magnitude for electrons, once the CdTe crystal is thinned down from the bulk to a monolayer. Most surprisingly, for monolayer CdTe, the electron thermalization time becomes independent of the electron excess energy up to around 0.5 eV, when counted from the conduction band minimum. We relate this peculiar behavior to the degenerate and parabolic lowest conduction band that yields a constant density of states in the 2D limit.

Zusammenfassung

Van der Waals Halbleiterheterostrukturen könnten in Zukunft in der nächsten Generation optoelektronischer oder photovoltaischer Geräte Anwendung finden um die Energie heißer photonisch angeregter Ladungsträger (engl. hot photoexcited carrier; Im Englischen wird das Wort “hot” verwendet, da die Energieverteilung einer höheren Temperatur als der Umgebungstemperatur entspricht, und deshalb hier mit “heiß” übersetzt.) zu nutzen. Die interne Quanteneffizienz von Bauteilen auf der Basis heißer Ladungsträger ist durch das Verhältnis der Raten der Entnahme und der Thermalisierung der photonisch angeregten Ladungsträger bestimmt. Um die Performance solcher Festkörperbauteile, die mit heißen Ladungsträgern arbeiten, zu verbessern, müssen die Ladungsträger entzogen werden und externe Arbeit verrichten, bevor sie thermalisieren. Dies verlangt ein grundlegendes Verständnis der Streuprozesse, durch die die heißen Ladungsträger Energie verlieren. Im Fall von intrinsischen Materialien, thermalisieren die heißen Ladungsträger im Bereich der Bandkanten vor allem durch Streuung mit Phononen. Wir präsentieren theoretische Betrachtungen der Dynamik von photonisch angeregten Ladungsträgern in 2D-Materialien, nämlich Graphen, Übergangsmetalldichalkogeniden und Cadmiumtellurid unter dem Einfluss der Elektron-Phonon-Wechselwirkung. Mit Hilfe der Relaxationszeit-Näherung, deren Parameter mit der Dichtefunktionaltheorie bestimmt werden, untersuchen wir die Thermalisierungsdynamik über einen großen Temperatur- und Energiebereich der Ladungsträger. Unsere Berechnungen enthalten Beiträge von allen Phononenzweigen der ersten Brillouinzone, also alle relevanten, durch Elektron-Phonon-Streuung auftretenden Übergänge. Unsere Ergebnisse können experimentell mit einer Pump-Probe-Spektroskopie überprüft werden.

Im Falle von Graphen zeigen wir unterstützt durch ein explizit lösbares Modellsystem, dass sich die Thermalisierungszeit der photonisch angeregten Ladungsträger um drei Größenordnungen ändert, wenn die Anregungsenergie von 1 eV auf 100 meV verringert wird. Genauer gesagt, findet die ultraschnelle Thermalisierung auf einer Femtosekunden-Zeitskala durch Emission von optischen Phononen statt, wird aber langsamer und findet im Pikosekunden-Bereich statt, sobald die Anregungsenergie ungefähr so groß ist wie die Energiequanten der optischen Phononen. Im letztgenannten Bereich hängt die Thermalisierungszeit deutlich von der Temperatur ab. Wegen der hohen Schmelztemperatur von Graphen untersuchen wir Temperaturen bis 2000 K und zeigen, dass derart hohe Temperaturen die Thermalisierungszeiten der angeregten Ladungsträger durch die Absorption von Phononen verringern.

In TMDC-Monolagen hängen die Thermalisierungszeiten photonisch angeregter Ladungsträger stark von der Form des Phononenspektrums und der elektronischen Spin-Orbit-Kopplung ab. Dir aufgehobene Spin-Entartung um die Bandkanten unterdrückt die Streuprozesse und verlangsamt dadurch die Thermalisierung der Ladungsträger. Außerdem verhalten sich die Thermalisierungszeiten in MoS_2 und WSe_2 unterschiedlich aufgrund unterschiedlicher Spin-Orbit Wechselwirkungen in diesen scheinbar ähnlichen Materialien. Deshalb erwarten wir, dass die interne Quanteneffizienz einer van der Waals Halbleiter-Tunnel-Heterostruktur (tunneling van der Waals semiconductor heterostructure) qualitativ davon abhängt, welches dieser beiden Materialien benutzt wird.

Für CdTe zeigen wir unsere theoretischen Vorhersagen über die Dynamiken photonisch angeregter Ladungsträger in einem hauchdünnen (etwa 1 nm) CdTe-Stab und vergleichen sie mit den Ergeb-

nissen für einen CdTe-Festkörper. Die Einheitszelle einer Monolage entspricht einer vier Atome dicken Scheibe, die aus dem ursprünglichen Festkörperkristall in der Zinkblenden-Phase entlang der [111]-Ebene herausgeschnitten wurde. Wir finden heraus, dass die Thermalisierungszeit photonisch angeregter Ladungsträger deutlich verringert wird, um eine Größenordnung für die Löcher und drei für die Elektronen, wenn man vom Kristall zur Monolage geht. Überraschenderweise wird die Thermalisierungszeit unabhängig von der überschüssigen Energie der Elektronen (gemessen von der Bandkante aus; engl.: electron excess engery) in einem Bereich bis 0.5 eV gesehen vom Leitungsbandminimum. Wir erklären das mit dem entarteten und parabelförmigen niedrigsten Leitungsband, das im zweidimensionalen Grenzfall zu einer konstanten Zustandsdichte führt.

Contents

Chapter 1

Introduction

The key factor in increasing the performance of a digital electronic device is to increase the number of metal-oxide-semiconductor field-effect transistors (MOSFET). This can be achieved by decreasing the gate length. At present, a single processor can have up to a few billion of MOSFET with a gate length of less than a few ten of nm as shown in Fig. 1.1. Making a device smaller will allow a faster response time which is one of the focuses of present-day technological advancements. The downscaling of transistors based on the conventional materials has reached a fundamental limit due to the current leakage, production costs, etc [1].

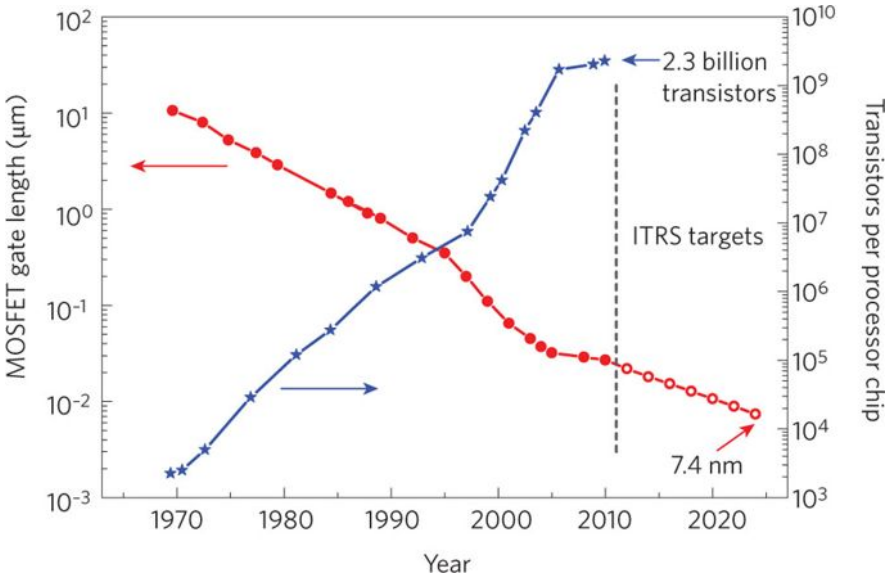

Figure 1.1: Evolution of MOSFET gate length in production-stage integrated circuits (filled red circles) and International Technology Roadmap for Semiconductors targets (open red circles). With decreasing gate lengths the number of transistors per processor incorporated in a chip has increased (blue stars). To maintain these trends new materials like graphene and TMDCs are being investigated. Reprinted by permission from Springer Nature: Springer Nature, Nature Nanotechnology @2002 Ref. [1].

Another drawback of the conventional materials can be seen in the photovoltaic (PV) solar panels. The present-day solar cell market is dominated by silicon, due to its abundance and low manufacturing cost [2]. In the lab, the maximum PV conversion efficiency recorded for various silicon based solar cells is less than 30% [3]. Silicon being an indirect band gap semiconductor is a poor light emitter as a result its efficiency is limited. This hurdle can be improved by replacing silicon with a direct-

gap and ultrathin absorbing material which can absorb more light and is cost effective. Continuous improvements in technology motivate the search of novel materials which can surpass the challenges and meet today's needs of ultrafast devices.

Dynamics of nonequilibrium carriers in semiconductors greatly impact the performance of solid-state devices because of the high excess energy that they can transfer [4, 5]. The phenomenon is especially interesting in low dimensional structures [6], where carriers can be extracted well before thermalization and potentially be exploited in external circuits [7]. The term "hot carriers" refers to electrons or holes that are out of equilibrium. The carriers are either described by a Fermi-Dirac distribution with a temperature hotter than those of the lattice or, in the strong nonequilibrium state when the concept of temperature becomes meaningless, they are instead characterized by a certain excess energy. The simplest way to generate such hot carriers in a semiconductor is the interband excitation of electron-hole pairs by light absorption or external electric field. The study of hot carriers has been a major focus of semiconductor physics dating back to early 1950's [4]. Hot carrier's properties are governed by interaction with the other carriers and elementary excitations (phonons, plasmons, etc.) leading to various scattering processes and eventually loss of energy before thermalization. To increase the efficiency of devices, either the fast extraction of the carriers before thermalization is required or slow down the cooling process or find a material with long thermalization time.

Recent progress in nanotechnology has made it possible to fabricate high-quality materials that are only one atom or a few atom thick and hence reach the fundamental two-dimensional (2D) limit for solid crystals [8–11]. This has lead to the emergence of a new class of materials called 2D materials and they provide a possibility for employing fast extraction and long thermalization of hot carriers. There are a wide number of techniques available to prepare 2D materials, like surface growth, mechanical exfoliation, vapor deposition, solution-phase growth, etc [8, 12–17] and can be characterized using fluorescence microscopy, transmission electron microscopy, scanning tunneling microscopy, Raman spectroscopy and X-ray diffraction etc [18–23]. To this date, many hundreds of new 2D materials have been reported [24]. Due to their ultimate thinness, these materials demonstrate various properties that are qualitatively different from their three-dimensional parent crystals. They provide an ideal playground to explore new physics and opportunities for better performances of ultrafast devices.

Geim and Novoselov reported discovery of graphene, the first 2D material at ambient conditions in 2004 [8]. They were awarded the Noble Prize in physics in 2010 for their discovery and groundbreaking experiments on graphene. Graphene, a single layer of carbon atoms arranged in a honeycomb lattice whose electronic properties are determined by the relativistic Dirac-equation with carriers having zero effective mass and Fermi velocity around the 0.01 times the speed of light [8, 25]. It possesses zero band gap and a very high carrier mobility [26]. The zero band gap of graphene results in the low $I_{\rm on}/I_{\rm off}$ ratio [27], which can be tuned by introducing a band gap in the graphene but it also makes graphene optically transparent. Another class of 2D materials which is well studied after graphene is transition metal dichalcogenides (TMDCs). They demonstrate a transition from the indirect to direct band gap when reduced from the bulk to a monolayer [28] and exhibit strong excitonic peaks in the photoluminescence spectrum [10, 29] due to the weak screening at monolayer level. Broken inversion symmetry and spin degeneracy allows selective excitations of the carriers in the semiconducting TMDCs [30, 31]. First MoS_2 transistor was made in laboratory in 2011, achieving $I_{\rm on}/I_{\rm off} \simeq 10^8$ and mobility of 200 $\rm cm^2\ V^{-1}\ s^{-1}$ at room temperature [32]. On the other hand, the opposite behavior of a direct to indirect band gap transition can be observed in metal monochalcogenides, leading to a vanishing of the excitonic absorption in stacks that are less than 8 atom thick [11]. All together this amazing properties has attracted the scientific community to explore their transport and optical properties and fabricate novel devices based on hot carriers [33–35].

These materials might have a potential to replace the conventional materials but that would need a deep understanding of the material properties and manufacturing control. There are several challenges

present in manufacturing layered 2D materials like controlling thickness, defects, orientation, and composition etc. Till now the devices based on 2D heterostructures have been realized and improving their manufacturing quality and efficiency have been a constant challenge. It must be pointed out that in less than a decade from its discovery, graphene's manufacturing has been revolutionized from micro-flakes to roll-to-roll sheets (30 inches wide) [8, 36]. Interestingly, 2D materials have become so popular that the number of academic publications has increased tremendously since their discovery [37, 38].

In perfect crystals, the dominant mechanisms involved in hot carrier thermalization are electron-electron and electron-phonon (EP) scattering [6, 39]. It is well established by means of *ab-initio* methods that the EP scattering plays a major role near the band edges [40–42]. EP interaction has a rich history in solid-state physics. It determines the electrical resistivity, carrier mobility, conventional superconductivity, indirect optical excitations, and hot carrier thermalization. Theoretically, EP interaction was mainly studied using semi-empirical model Hamiltonian which used the EP matrix elements as [43]

$$g_{\lambda}^{nm}(\mathbf{k},\mathbf{q}) = -i\left(\frac{\hbar}{2N_p M_k \omega_{\mathbf{q}\lambda}}\right)^{1/2} \mathbf{q}\cdot\mathbf{e}_{\kappa\lambda}(\mathbf{q})V_0. \tag{1.1}$$

In Eq. (1.1), N_p is the number of unit cells in Born-von Kàrmàn supercell, M_κ is the mass of κ^{th} nucleus, $\mathbf{e}_{\kappa\lambda}(\mathbf{q})$ is the polarization vector of the phonon of wave vector $\mathbf{q}$ and branch λ of κ^{th} nuclei and V_0 is the effective potential of the unit cell. The choice of V_0 was highly system-dependent and there was no general form for it. For metals, rigid-ion approximation was used by Bloch [43] where $V_0 = \hbar^2/(16 m_e a_0^2)$ [a_0 is the Bohr radius]. Bloch's approximation was further modified by Nordheim *et al.* who replaced V_0 by Fourier component $V_\kappa(\mathbf{q})$ of Coulomb potential [44] and later on Bardeen *et al.* introduced dielectric screening to $V_\kappa(\mathbf{q})$ [45]. For semiconductors, deformation potential defined by Bardeen and Shockley was used [46, 47]. Ionic crystals provided with the challenge of long-range electric fields generated by atomic displacements and Fröhlich *et. al* showed in case of isotropic ionic crystals $V_0 \propto |\mathbf{q}|^{-2}$ [48]. With the arrival of density functional theory (DFT) and density functional perturbation theory (DFPT), Dacorogna *et al.* were the first one to calculate the EP matrix elements by means of *ab-initio* methods [49]. The EP matrix element was defined in the following form

$$g_{\lambda}^{nm}(\mathbf{k},\mathbf{q}) = \langle u_{m\mathbf{k}+\mathbf{q}} | \partial_{\lambda\mathbf{q}} V^{\text{KS}} | u_{m\mathbf{k}} \rangle, \tag{1.2}$$

where, $u_{n\mathbf{k}}$ is the Bloch periodic part of Kohn-Sham wavefunction and, $\partial_{\lambda\mathbf{q}} V^{\text{KS}}$ is the derivative of the self-consistent Kohn-Sham potential with respect to displacements of nuclei along the phonon mode λ and momentum $\mathbf{q}$. Accurate mapping of EP scattering events in the first Brillouin zone (BZ) requires the evaluation of hundreds of million of EP matrix elements as defined in Eq. (1.2) making it computationally extremely expensive approach. Semi-empirical models used to study EP interaction either neglected acoustical phonons or considered only few points in the BZ [50–55]. This hinders the full understanding of EP scattering events.

We present an *ab-initio* method which combines DFT with many-body perturbation theory to calculate carrier's self-energy from EP interaction to the lowest order. We use an interpolation scheme based on Wannier functions (WF) developed by Giustino *et al.* for interpolating EP matrix elements on fine $\mathbf{k}$,$\mathbf{q}$ grids to reduce the computational cost adequately [56]. We take into account the electronic and phononic band structures and calculate the band and momentum resolved scattering times along with its temperature dependence. The information about the EP scattering processes is intact in the form of EP matrix elements. We use scattering times obtained from the *ab-inito* methods in the Boltzmann equation under the relaxation time approximation (RTA) to calculate the thermalization time. The novelty of this method lies in the fact that it includes the contributions arising from all the optical and acoustical phonon branches and maps it on the whole BZ. Moreover, we include inter- and intraband

processes due to EP scattering (see Fig. 1.2). Our approach provides access to the microscopic details involved in photocarrier thermalization processes which is otherwise very challenging to extract from experiments.

In summary, we study the thermalization of hot carriers due to EP interaction in different 2D materials using *ab-initio* methods. Our fundamental studies can help for a better understanding of the thermalization processes around the band edges. We focus on graphene, MoS_2, WSe_2, bulk and monolayer CdTe due to their distinctive electronic, optoelectronic and PV properties.

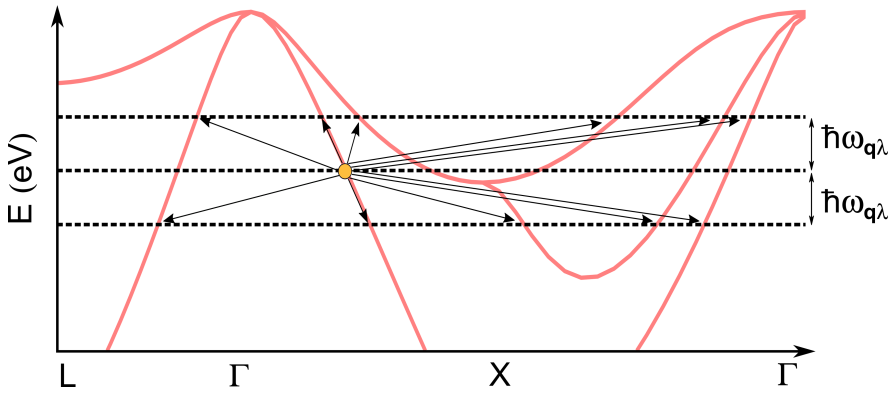

Figure 1.2: Schematic representation of our model used in this work. It shows a carrier (orange bullet) can scatter to any other state via phonon of energy $\hbar\omega_{\mathbf{q}\lambda}$ at a certain temperature. All the inter- and intraband transitions (shown by arrows) are captured by Eq. (1.2). Here, we used silicon valance band structure as an example.

Outline Ch. 2 explains the theoretical framework used in this thesis. We briefly discuss the DFT and lattice dynamics in Sec. 2.1 and 2.2 respectively. It is followed by the detailed derivation of the self-energy of a carrier from EP interaction using Matsubara Green's function formalism in Sec. 2.3. This chapter ends with the derivation of the Boltzmann equation under RTA in Sec. 2.4.

In Ch. 3, we develop a deep understanding of the photocarrier thermalization in graphene based on the formalism described in Ch. 2 along with an explicitly solvable model. We explore thermalization times for range of temperatures and excitation energies. A clear proof of existence of thermalization bottleneck for photoexcited carriers in graphene is provided.

We extend our formalism by introducing the spin-orbit coupling (SOC) in our calculations and study its effect on the EP scattering processes in Ch. 4. We choose MoS_2 and WSe_2 monolayer due to their potential device applications. We compare the carrier dynamics of the monolayers with and without SOC. Additionally, the thermalization time based on optical and acoustical phonons scattering processes is separated and compared with the total thermalization time. Using an analytical model, tunneling time is estimated and ratio of thermalization and tunneling time is calculated for both the monolayers.

In Ch. 5, we will make prediction on the existence of stable monolayer CdTe based on its dynamical stability through phonon calculations. We present a comparison between the thermalization times of electrons and holes of the bulk CdTe and monolayer CdTe. In the next Ch.6, we investigate the absorption properties of GaSe as a function of number of layers. The experiment has been performed at University of Konstanz and details are presented in the PhD thesis of Dr. Budweg. All the chapters include a short introduction and summary of the current chapter. A general summary of the whole thesis is given in Ch.7 with an outlook. At the end of thesis a complete list of abbreviations used in all the chapters is provided.

Chapter 2

Theoretical approach

In the present chapter, we will provide the outline of theoretical approach used in this work. We will start with the Hohenberg-Kohn theorems [57] and Kohn-Sham approach [58] in Sec. 2.1 which is used to implement DFT. Then, we will shortly discuss the basic formalism for lattice vibrations in Sec. 2.2. Using Green's function approach in perturbative series expansion in Sec. 2.3, we will derive the self-energy of the carrier from EP interaction in an elaborate way [59]. We will end this chapter with discussion on the Boltzmann equation within RTA in Sec. 2.4 which is used to study the time evolution of the photoexcited carriers and compute the thermalization times.

2.1 Density functional theory

2.1.1 Hohenberg-Kohn theorems

The quest of finding new materials to meet the technological advancements has always been the center of solid-state and condensed matter physics. With the current development of computational methods, it has been possible to envision the existence of new compounds/materials and investigate their properties fairly well [60, 61], by merely providing the geometrical structures. This reduces the burden of synthesising each and every material in the lab which is very challenging task especially in case of 2D and lower dimensional materials. One can pick up the materials of their interest directly. The driving force behind the success of creating materials database [60, 61] is the first principle methods like DFT which has made it possible to estimate thermodynamic and dynamical stability of systems without any adjustable parameters. Now a days, DFT is the most popular quantum mechanical approach to study the material properties in physics and chemistry. In 1998, Walter Kohn was awarded Nobel Prize in chemistry for his contribution in the development of the DFT. Having said that let us have a look on the formalism of DFT.

To study the properties of the system, it involves solving time independent Schrödinger's equation with the many-body Hamiltonian defined as

$$\begin{aligned} H_{tot} &= -\sum_{I} \frac{P_I^2}{2M_I} - \sum_{i} \frac{p_i^2}{2} + \frac{1}{2}\sum_{I\neq I'} \frac{Z_I Z_{I'}}{|\mathbf{R}_I - \mathbf{R}_{I'}|} + \frac{1}{2}\sum_{i\neq i'} \frac{1}{|\mathbf{r}_i - \mathbf{r}_{i'}|} - \sum_{i,I} \frac{Z_I}{|\mathbf{R}_I - \mathbf{r}_i|}, \\ &= T_N + T_e + E_N + E_{ee} + E_{\text{ext}}. \end{aligned} \tag{2.1}$$

We have used the atomic units i.e. $\hbar = m_e = e = 4\pi\epsilon_0 = 1$. The sum I and i run over the number of nuclei and the electrons respectively and both are fixed in the system. T_N and T_e are the total kinetic energy of nuclei and electrons systems respectively. The mass of the I^{th} nuclei is represented by M_I. E_N, E_{ee} and E_{ext} are the Coulomb interaction between nucleus-nucleus, electron-electron and

nucleus-electron respectively. Since the $m_e/M = 1/1836$, the electrons move much faster than nuclei. For this reason, the kinetic energy of nuclei T_N can be neglected as compared with the kinetic energy T_e of electrons. This simplification is called as Born-Oppenheimer approximation. With the fixed positions of nuclei, E_N becomes a classical additive which is a constant in total energy and hence can be neglected. Hence, we are left with the electronic Hamiltonian which reads

$$\begin{aligned} H &= -\sum_i \frac{p_i^2}{2} + \frac{1}{2}\sum_{i\neq i'} \frac{1}{|\mathbf{r}_i - \mathbf{r}_{i'}|} - \sum_{i,I} \frac{Z_I}{|\mathbf{R}_I - \mathbf{r}_i|}, \\ &= T_e + E_{ee} + \sum_i V_{\text{ext}}(\mathbf{r}_i). \end{aligned} \tag{2.2}$$

In the Eq. 2.2, $V_{\text{ext}}(\mathbf{r})$ is the potential field created by the nuclei. For a given Hamiltonian H, Schrödinger's equation can be written as

$$H|\Psi(\mathbf{r_1}, \mathbf{r_2}, \ldots, \mathbf{r_N})\rangle = E|\Psi(\mathbf{r_1}, \mathbf{r_2}, \ldots, \mathbf{r_N})\rangle. \tag{2.3}$$

The basic principle of quantum mechanics is that once we have obtained the eigenfunctions of the system $\Psi(\mathbf{r_1}, \mathbf{r_2}, ..., \mathbf{r_N})$ all the observable of the system can be evaluated. It should be noted that even after simplifying the $H_{tot} \rightarrow H$, it is not straight forward to tackle this problem because of many-body interactions involved in it. Additionally $\Psi(\mathbf{r_1}, \mathbf{r_2}, ..., \mathbf{r_N})$ is a function of 3N degrees of freedoms which provides computational bottleneck for evaluating the Eq. 2.3 directly. Hohenberg-Kohn gave a formalism to solve the Eq. (2.3) called DFT [57]. It is based on two theorems called Hohenberg-Kohn theorems stated as follows:

Theorem I: The external potential, V_{ext} is uniquely determined up to a constant by the ground state density $\rho(\mathbf{r})$. In other words, $\rho(\mathbf{r})$ fixes the V_{ext} and hence the Hamiltonian H, which implies that all the properties of the system can be determined by the ground state electronic density only.

Theorem I can be checked with the proof of contradiction. Let us say that the $|\Psi\rangle$ is the ground state wavefunction of the Hamiltonian H with $\rho(\mathbf{r}) = \langle\Psi|\sum_i \delta(\mathbf{r} - \mathbf{r_i})|\Psi\rangle$. We make a claim that there exists another Hamiltonian H' with the ground state wavefunction $|\Psi'\rangle$. Both ground state wavefunctions $|\Psi\rangle$ and $|\Psi'\rangle$ lead to the same ground state density i.e. $\rho(\mathbf{r})$. The Hamiltonian H and H' are related via relation $H' = H + V'_{\text{ext}} - V_{\text{ext}}$ and differ by more than a constant. Both the Hamiltonian satisfy different Schrödinger's equation:

$$H|\Psi\rangle = E|\Psi\rangle, \tag{2.4}$$

$$H'|\Psi'\rangle = E'|\Psi'\rangle. \tag{2.5}$$

The ground state energy for the H' is

$$E' = \langle\Psi'|H'|\Psi'\rangle < \langle\Psi|H'|\Psi\rangle, \tag{2.6}$$

and using the relation between H and H'

$$\begin{aligned} \langle\Psi|H'|\Psi\rangle &= \langle\Psi|H|\Psi\rangle + \langle\Psi|H' - H|\Psi\rangle, \\ &= E + \int [V'_{\text{ext}}(\mathbf{r}) - V_{\text{ext}}(\mathbf{r})]\rho(\mathbf{r})\mathrm{d}^3\mathbf{r}. \end{aligned} \tag{2.7}$$

On putting Eq. (2.6) in Eq. (2.7) we have

$$E' < E + \int [V'_{\text{ext}}(\mathbf{r}) - V_{\text{ext}}(\mathbf{r})]\rho(\mathbf{r})\mathrm{d}^3\mathbf{r}. \tag{2.8}$$

Similarly, if we consider H in the same way as above, we get

$$E < E' + \int [V_{\text{ext}}(\mathbf{r}) - V'_{\text{ext}}(\mathbf{r})]\rho'(\mathbf{r})\mathrm{d}^3\mathbf{r}. \tag{2.9}$$

On adding Eq. (2.8) and (2.9) we arrive at

$$E + E' < E' + E. \tag{2.10}$$

This inequality proves that there can not be two different external potentials V_{ext} and V'_{ext} which can give rise to the same ground state charge density $\rho(\mathbf{r})$.

Theorem II: The total energy functional E[$\rho(\mathbf{r})$] can be minimized for the true ground state density $\rho(\mathbf{r})$ only. The ground state density integrated over space will give the particle number $N = \int \rho(\mathbf{r})d\mathbf{r}$.

This theorem can be proved with the help of variational principle. The total energy functional E[ρ] can be written as

$$\begin{aligned} E[\rho] &= T_e[\rho] + E_{ee}[\rho] + \int V_{\text{ext}}(\mathbf{r})\rho(\mathbf{r})\mathrm{d}^3\mathbf{r}, \\ &= F_{\text{HK}}[\rho] + \int V_{\text{ext}}(\mathbf{r})\rho(\mathbf{r})\mathrm{d}^3\mathbf{r}, \end{aligned} \tag{2.11}$$

where, $F_{\text{HK}}[\rho]$ is a universal functional of $\rho(\mathbf{r})$, that includes the kinetic and potential energies of the interacting electronic system. Let's say that E and E' are the total energy of the same system derived from the two ground state densities $\rho(\mathbf{r})$ and $\rho'(\mathbf{r})$ respectively corresponding to the wavefunctions Ψ and Ψ'. It is evident that

$$E[\rho] = \langle\Psi|H|\Psi\rangle < \langle\Psi'|H|\Psi'\rangle = E'[\rho]. \tag{2.12}$$

The Eq. (2.12) implies that for a known $F_{\text{HK}}[\rho]$, total energy functional E can be minimized with respect to the density $\rho(\mathbf{r})$ only. The major accomplishment of the Hohenberg-Kohn theorems is that now the problem Eq. (2.3) which initially depended upon 3N degrees of freedom is now reduced to finding the ground state $\rho(\mathbf{r})$ which depends upon three degrees of freedom.

2.1.2 Kohn-Sham approach

In the last Sec. 2.1.1, we saw how the total energy of the system can be written as a functional of ground state density $\rho(\mathbf{r})$. But Hohenberg-Kohn theorems did explain how $\rho(\mathbf{r}$ can be obtained. In 1965, Kohn and Sham derived a formalism to obtain ground state density in their seminal paper Ref. [58]. It should be noted that $\rho(\mathbf{r})$, itself does not give any information on the system's properties but provides a subtle way to calculate it. The most burdensome term to deal in the Eq.(2.2) is the electron-electron interaction E_{ee} and the kinetic energy operator T_e of electrons because of many-body effects. Kohn-Sham approach is based on the *anstaz* that the interacting many-body system Eq.(2.2) can be replaced by auxiliary non-interacting system whose ground state density $\rho(\mathbf{r})$ can be determined exactly [58]. The many-body interacting is replaced by non-interacting or auxiliary system and all the many-body effects are approximated by local or semi-local functional of density ρ. The density of the electrons is calculated from the single particle wavefunctions $\psi_i(\mathbf{r})$ as

$$\rho(\mathbf{r}) = \sum_{i}^{occ} \psi_i^*(\mathbf{r})\psi_i(\mathbf{r}). \tag{2.13}$$

In its simplest form E_{ee} energy can be defined with classical Hartree form

$$E_{\text{Hartree}}[\rho] = \frac{1}{2}\int \frac{\rho(r)\rho(r')}{|\mathbf{r}-\mathbf{r}'|}\mathrm{d}^3\mathbf{r}\,\mathrm{d}^3\mathbf{r}'. \tag{2.14}$$

The kinetic energy of the interacting electrons is divided into two parts i) non-interacting or single particles term $T_s[\rho]$ and ii) $T_c[\rho]$ which contains the correlation effects from the many-body system. The single particle kinetic energy can be obtained with wavefunctions $\psi_i(\mathbf{r})$ by

$$T_s[\rho] = -\frac{1}{2}\sum_i^{occ}\int \psi_i^*(\mathbf{r})\nabla^2\psi_i(\mathbf{r})\mathrm{d}^3\mathbf{r}. \tag{2.15}$$

The total energy of the interacting system defined via Eq. (2.11) is rewritten in terms of auxiliary Kohn-Sham system as

$$E_{\text{KS}}[\rho] = T_s[\rho] + E_{\text{ext}}[\rho] + E_{\text{Hartree}}[\rho] + E_{\text{xc}}[\rho], \tag{2.16}$$

and

$$\begin{aligned} E_{\text{xc}}[\rho] &= F_{\text{HK}}[\rho] - T_s[\rho] - E_{\text{Hartree}}[\rho], \\ E_{\text{xc}}[\rho] &= (T_e - T_s[\rho]) + (E_{ee} - E_{\text{Hartree}}[\rho])\,. \end{aligned} \tag{2.17}$$

The exchange-correlation energy $E_{\text{xc}}[\rho]$ contains all the many-body effects which are ignored by simplifying the $F_{\text{HK}}[\rho]$ in terms of $E_{\text{Hartree}}(\mathbf{r})$ and $T_s[\rho]$. The exchange correlation term is approximated by parameterization of homogeneous electron gas. To find the ground state of the system under study, one has to minimize the Eq. (2.16) with respect to the electron density or alternatively wavefunctions with the help of variational principle. Here we use $\psi_i^\dagger((r))$ as variational parameter for minimization

$$\frac{\delta E_{\text{KS}}}{\delta\psi_i^\dagger(\mathbf{r})} = \frac{\delta T_s[\rho]}{\delta\psi_i^\dagger(\mathbf{r})} + \left[\frac{\delta E_{\text{ext}}[\rho]}{\delta\rho(\mathbf{r})} + \frac{\delta E_{\text{Hartree}}[\rho]}{\delta\rho(\mathbf{r})} + \frac{\delta E_{\text{xc}}[\rho]}{\delta\rho(\mathbf{r})}\right]\frac{\delta\rho(\mathbf{r})}{\delta\psi_i^\dagger(\mathbf{r})} = 0. \tag{2.18}$$

From the Eq. (2.15) and definition of $\rho(\mathbf{r})$ it is evident that

$$\frac{\delta T_s[\rho]}{\delta\psi_i^\dagger(\mathbf{r})} = -\frac{1}{2}\nabla^2\psi_i(\mathbf{r}), \qquad \frac{\delta\rho(\mathbf{r})}{\delta\psi_i^\dagger(\mathbf{r})} = \psi_i(\mathbf{r}). \tag{2.19}$$

In addition to the above equations, we introduce Lagrange multiplier ε_i to satisfy the constraint $\langle\psi_i|\psi_j\rangle = \delta_{ij}$. Eq. (2.18) becomes

$$\left[-\frac{1}{2}\nabla^2 + V_{\text{ext}}(\mathbf{r}) + V_{\text{Hartree}}(\mathbf{r}) + V_{\text{xc}}(\mathbf{r})\right]\psi_i(\mathbf{r}) = \varepsilon_i\psi_i(\mathbf{r}), \tag{2.20}$$

where

$$\begin{aligned} V_{\text{Hartree}}(\mathbf{r}) &= \int \frac{\rho(\mathbf{r}')}{|\mathbf{r}-\mathbf{r}'|}\mathrm{d}^3\mathbf{r}', \qquad V_{\text{xc}}(\mathbf{r}) = \frac{\delta E_{\text{xc}}[\rho]}{\delta\rho}, \\ V^{\text{KS}}(\mathbf{r}) &= V_{\text{ext}}(\mathbf{r}) + V_{\text{Hartree}}(\mathbf{r}) + V_{\text{xc}}(\mathbf{r}). \end{aligned} \tag{2.21}$$

The Eq. (2.20) and (2.21) are known as Kohn-Sham equations for the auxiliary system. It can be solved in a self-consistent way without introducing any adjustable parameters. Special comment on the exchange-correlation energy E_{xc} is needed.

The $E_{\rm xc}[\rho]$ can be written as a functional of $\rho(\mathbf{r})$ and $\mathbf{r}$ as

$$E_{\rm xc}[\rho] = \int \rho(\mathbf{r})\epsilon_{\rm xc}\left([\rho],\mathbf{r}\right)\mathrm{d}^3\mathbf{r}, \tag{2.22}$$

where, $\epsilon_{\rm xc}[\rho]$ is the exchange-correlation energy per electron. If the exact form of the $E_{\rm xc}$ or alternatively $\epsilon_{\rm xc}[\rho]$ was known then DFT can provide the exact solution. Unfortunately that is not the case. There are various ways to estimate this term, namely local density approximation (LDA), generalized gradient approximation (GGA) and hybrid functional. In this work, we have used LDA only so we will describe this approximation briefly here. Within LDA, the Eq. (2.22) can be written as

$$\delta E_{\rm xc}[\rho] = \int \left[\epsilon_{\rm xc}^{\rm hom} + \rho\frac{\partial\epsilon_{\rm xc}^{\rm hom}}{\partial\rho}\right]\delta\rho\mathrm{d}^3\mathbf{r}. \tag{2.23}$$

On comparing Eq. (2.21) with Eq. (2.22), the $V_{\rm xc}(\mathbf{r})$ takes the form

$$V_{\rm xc}(\mathbf{r}) = \left[\epsilon_{\rm xc}^{\rm hom} + \rho\frac{\partial\epsilon_{\rm xc}^{\rm hom}}{\partial\rho}\right]. \tag{2.24}$$

Within LDA, the exchange term is simply defined through the homogeneous electron gas and varies as $\rho(\mathbf{r})^{\frac{1}{3}}$

$$V_{\rm x}(\mathbf{r}) = \frac{4}{3}\epsilon_x(\rho) \qquad \text{with} \qquad \epsilon_{\rm x}(\rho) = -\frac{3}{4}\left(\frac{6\rho(\mathbf{r})}{\pi}\right)^{\frac{1}{3}}, \tag{2.25}$$

whereas, the correlation term $\epsilon_c(\mathbf{r})$ arises from the repulsion between the electrons with the opposite spins reducing the electronic energy. Unlike $\epsilon_x(\mathbf{r})$ there is no exact known form of $\epsilon_c(\mathbf{r})$. The correlation part is basically fitted to the correlation energies of the homogeneous electron gas to find an analytical form. One of the example which we used frequently in our work is derived by Perdew and Zunger [62],

$$\epsilon_c^{\rm PZ}(r_s) = \begin{cases} -0.0480 + 0.031\ln(r_s) - 0.0116r_s + 0.0020r_s\ln(r_s), & r_s < 1, \\ -0.1423/(1 + 1.0529\sqrt{r_s} + 0.3334r_s), & r_s > 1, \end{cases} \tag{2.26}$$

here, r_s is the average distance between the electrons $r_s = (3/4\pi\rho)^{1/3}$.

In this section, we have provided a basic outline of DFT a powerful tool to access the electronic structures of many-body systems using quantum mechanical scheme based on Hohnberg-Kohn theorems and Kohn-Sham approach. We use an open source package QUANTUMESPRESSO [63] for DFT simulations. Further details and current developments in DFT can be found in [64–66].

2.2 Lattice vibrations

Phonons are the collective excitations of atoms or molecules in crystals and liquids. These vibrations are caused either through the temperature or the external fields. In general, the motion of atoms/nuclei are much slower than the electrons, so it is possible to neglect the effect of electronic energy on the nuclear motion and is called Born-Oppenheimer approximation which we have used previously. This problem is treated in a classical way. The notation used in this section is adapted from Ref. [67].

The position of a nucleus is defined as

$$\begin{aligned}\mathbf{R}_{l,j}(t) &= \mathbf{R}_l^0 + \boldsymbol{b}_j + \boldsymbol{\xi}_{l,j}(t),\\ &= \mathbf{R}_{l,j}^0 + \boldsymbol{\xi}_{l,j}(t),\end{aligned} \tag{2.27}$$

where, $\mathbf{R}_l^0$ is the lattice point and $\mathbf{b}_j$ is basis vectors of j^{th} unit cell in the system. $\boldsymbol{\xi}_{l,j}$ is the displacement of the atoms from their equilibrium position. The ground state potential energy $E^{\mathrm{P}}(\mathbf{R})$ of the system can be expanded as Taylor series expansion in term of displacement $\boldsymbol{\xi}_{l,j}$,

$$\begin{aligned}E^{\mathrm{P}}(\mathbf{R}) &= E_0^{\mathrm{P}}(\mathbf{R}) + \frac{1}{2}\sum_{\substack{n,\alpha\\ n,\alpha'}} \frac{\partial^2 E^{\mathrm{P}}(\mathbf{R})}{\partial\xi_n^\alpha \partial\xi_{n'}^{\alpha'}}\xi_n^\alpha \xi_{n'}^{\alpha'} + ...,\\ E^{\mathrm{P}}(\mathbf{R}) &= E_0^{\mathrm{P}}(\mathbf{R}) + \frac{1}{2}\sum_{\substack{n,\alpha\\ n,\alpha'}} A_{nn'}^{\alpha\alpha'}\xi_n^\alpha \xi_{n'}^{\alpha'}.\end{aligned} \tag{2.28}$$

We have suppressed the indices (l, j) to n. The quantity $A_{jj'}^{\alpha\alpha'}(\mathbf{R}_l - \mathbf{R}'_l)$ is the interatomic force constant (IFC) and obeys the symmetry rules of the crystal. The indices $\alpha, \alpha' =$ x, y and, z. The equation of motion of the nuclei can be written as

$$\begin{aligned}\dot{\mathbf{P}}_n &= -\nabla_{\xi_n} E^{\mathrm{P}}(\mathbf{R}).\\ M_n\ddot{\xi}_n^\alpha &= -\sum_{n'\alpha'} A_{nn'}^{\alpha\alpha'}\xi_{n'}^{\alpha'}.\end{aligned} \tag{2.29}$$

If we assume that every nucleus is moving periodically with same frequency ω, the solution for $\xi_{lj}^\alpha(t)$ can be written as

$$\xi_{lj}^\alpha(t) = C_{lj}^\alpha \frac{1}{\sqrt{M_j}} e^{i\omega t}, \tag{2.30}$$

here, C_{lj}^α is the amplitude of vibration. Using the definition of ξ_{lj} from Eq. (2.30) and inserting it Eq. (2.29). we get

$$\omega^2 C_{ij}^\alpha = \sum_{l'j'\alpha'} \frac{1}{\sqrt{M_j M_{j'}}} A_{jj'}^{\alpha\alpha'}(\mathbf{R}_l - \mathbf{R}'_l) C_{l'j'}^{\alpha'}. \tag{2.31}$$

We define $D_{jj'}^{\alpha\alpha'}(\mathbf{R}_l - \mathbf{R}'_l) = \frac{1}{\sqrt{M_j M_{j'}}} A_{jj'}^{\alpha\alpha'}(\mathbf{R}_l - \mathbf{R}'_l)$ which is a square matrix with dimension $[3 \times b_n \times N]^2$ where b_n is the number of basis atoms and N is the number of unit cells. It will have $3b_nN$ real eigenvalues ω_i^2. The solution for the vibrational amplitude C can be written in Bloch form

$$C_{lj}^\alpha = C_j^\alpha e^{-i\mathbf{q}.(\mathbf{R}_l^0 + \mathbf{b}_j)}. \tag{2.32}$$

Using Eq. (2.32), Eq. (2.31) transforms to

$$\omega^2 C_j^\alpha = \sum_{j'\alpha'} \left[e^{i\mathbf{q}.(\boldsymbol{b}_j - \boldsymbol{b}_{j'})} \sum_l D_{jj'}^{\alpha\alpha'}(\mathbf{R}_l - \mathbf{R}'_l) e^{i\mathbf{q}.(\mathbf{R}_l^0 - \mathbf{R}_{l'}^0)} \right] C_{j'}^{\alpha'}. \tag{2.33}$$

The term in the square bracket is nothing just the Fourier transformation of IFC in $\mathbf{q}$-space and can be written in the determinant form as

$$\det \left| D_{jj'}^{\alpha\alpha'}(\mathbf{q}) - \omega_{\mathbf{q}\lambda}^2 \right| = 0, \tag{2.34}$$

here, $D_{jj'}^{\alpha\alpha'}(\mathbf{q})$ is called dynamical matrix and Eq. (2.34) will have $3b_n$ set of eigenfrequencies for each $\mathbf{q}$ point in the first BZ and $\lambda = 1$ to $3b_n$. First, $\omega_{\mathbf{q}\lambda}$ is calculated on the uniform $\mathbf{q}$ mesh and then interpolated on the desired path or fine grids. If we translate the crystal, the energy of the crystal must be invariant. Due to the use of real space grids in evaluating E_{xc} this rule is broken at the zone center i.e. Γ point. This is fixed by imposing a constraint called acoustic sum rule on the dynamical matrix at Γ point such that

$$\sum_{j'} D_{jj'}^{\alpha\alpha'}(\mathbf{q} = \mathbf{0}) = 0. \tag{2.35}$$

In case of the polar materials, long range nature of the Coulomb interaction $(1/|\mathbf{q}|^2)$ causes splitting between longitudinal optical (LO) and transverse optical (TO) modes at Γ point. This is taken into account by adding non-analytical in the dynamical matrix around Γ point as [68]

$$\begin{aligned} D_{jj'}^{\alpha\alpha'}(\mathbf{k} \to 0) &= D_{jj'}^{\alpha\alpha'}(\mathbf{k} = 0) + \tilde{D}_{jj'}^{\alpha\alpha'}(\mathbf{k} \to 0), \\ \tilde{D}_{jj'}^{\alpha\alpha'}(\mathbf{k} \to 0) &= \frac{4\pi}{\Omega} \frac{(\sum_\gamma q_\gamma Z_j^{*\gamma\alpha}) \sum_{\gamma'} (q_{\gamma'} Z_j^{*\gamma'\alpha'})}{\sum_{\alpha\alpha'} q_\alpha \epsilon_{\alpha\alpha'}^\infty q_{\alpha'}}, \end{aligned} \tag{2.36}$$

where $Z_j^{*\gamma\alpha}$, the Born effective charge tensor. Quoting the definition from Ref. [68] $Z_j^{*\gamma\alpha}$ is defined as "proportionality coefficient relating, at linear order, the polarization per unit cell, created along the direction γ, and the displacement along the direction α of the atoms belonging to the sublattice j, under the condition of a zero electric field". It is always a real quantity and * in the superscript does not denote the complex conjugate. $\epsilon_{\alpha\alpha'}^\infty$ is the dielectric permitivity tensor along direction $\alpha\alpha'$ in long wavelength limit and Ω is the volume of unit cell.

2.3 Self-energy of carrier from electron-phonon interaction

In last two sections, we have discussed how to calculate ground state eigenvectors and eigenvalues for electrons and phonons using *ab-inito* methods. Now, we intend to use these quantities to study self-energy of the carriers from EP interaction. Self-energy is defined as contribution to the carrier's energy due to the interaction between other particles and system which it is part of. From self-energy one can deduce a very important quantity called scattering time which is the average time spent by the particle in a state before scattering. In this section, we derive the self-energy expression within Matsubara Green's function formalism. We use the grand canonical ensemble to for quantum mechanical averages. The notations we have used here can be found in many text books like G.D. Mahan and F. Han [59, 69]. A very detailed review on EP interaction is given by Giustino in Ref. [70]. Before discussing the derivation of the self-energy, here we provide some useful formulas that will be used in this section.

2.3.1 Useful relations

We use Matsubara Green's function method and the advantage of this method lies in the fact that time evolution of the system can be seen in terms of temperature or vice-versa which we will be clear later in this section. Let's have a look on the series expansion of phonon occupation $N(\omega_{\mathbf{q}\lambda})$ and Fermi occupation $f(\varepsilon_{n\mathbf{k}})$ at temperature T

$$\begin{aligned} N(\omega_{\mathbf{q}\lambda}, T) &= \frac{1}{e^{\beta\omega_{\mathbf{q}\lambda}} - 1} = -\frac{1}{2} + \frac{1}{\beta}\sum_{m=-\infty}^{\infty} \frac{1}{2m\pi i/\beta - \omega_{\mathbf{q}\lambda}}, \\ f(\varepsilon_{n\mathbf{k}}, T) &= \frac{1}{e^{\beta\varepsilon_{n\mathbf{k}}} + 1} = \frac{1}{2} + \frac{1}{\beta}\sum_{m=-\infty}^{\infty} \frac{1}{(2m+1)\pi i/\beta - \varepsilon_{n\mathbf{k}}}, \end{aligned} \tag{2.37}$$

here, the factor $\beta = 1/kT$ is used. $\omega_{\mathbf{q}\lambda}$ is the phonon energy of wave vector $\mathbf{q}$ and branch λ respectively. Similarly $\varepsilon_{n\mathbf{k}}$ is the electron energy of band n and wave vector $\mathbf{k}$. For simplification, we omit the T in $N(\omega_{\mathbf{q}\lambda}, T)$ and $f(\varepsilon_{n\mathbf{k}}, T)$. The idea here is that any meromorphic function can be expanded as a summation of its poles and residues at those poles. $N(\omega_{\mathbf{q}\lambda})$ has poles at $\omega_{\mathbf{q}\lambda} = 2\pi i m/\beta$. $f(\varepsilon_{n\mathbf{k}})$ has poles at $\varepsilon_{n\mathbf{k}} = (2m+1)\pi i m/\beta$ and $\varepsilon_{n\mathbf{k}}$ is measured with respect to the chemical potential μ. The summation in Eq. (2.37) can be written as

$$\begin{aligned} &\sum_m \frac{1}{i\omega_m - \omega_{\mathbf{q}\lambda}} && \omega_m = 2\pi m/\beta, \\ &\sum_m \frac{1}{i\omega_m - \varepsilon_{n\mathbf{k}}} && \omega_m = (2m+1)\pi/\beta. \end{aligned} \tag{2.38}$$

The above equations look like Green's function with imaginary frequencies $i\omega_m$. This formulation is helpful when taking the Fourier transformation, then we need to sum over even multiple of π/β for bosons and odd multiple of π/β for fermions. Now, we define the Fourier transformation of a function $\mathscr{F}$ in the time (τ) and energy (ω_m) domain as

$$\begin{aligned} \mathscr{F}(i\omega_m) &= \int_0^\beta d\tau e^{i\omega_m\tau}\mathscr{F}(\tau), \\ \mathscr{F}(\tau) &= \frac{1}{\beta}\sum_m e^{-i\omega_m\tau}\mathscr{F}(i\omega_m), \end{aligned} \tag{2.39}$$

where, ω_m can take only discrete values according to Eq. (2.38) depending upon whether $\mathscr{F}$ is a fermionic or bosonic function. Following are some useful identities regarding Fourier transformation

$$\begin{aligned} \frac{1}{\beta}\int_0^\beta d\tau e^{\pm i(\omega_m-\omega_{m'})\tau} &= \delta_{m,m'}, \\ \frac{1}{\beta}\sum_m e^{\pm i\omega_m(\tau-\tau')} &= \delta(\tau-\tau'). \end{aligned} \tag{2.40}$$

2.3.2 Electron Green's function

Consider a system with Hamiltonian K which is in contact with the thermal reservoir at temperature T. The average of an operator A in grand canonical ensemble is calculated as

$$\langle A\rangle = \frac{\mathrm{Tr}[Ae^{-\beta K}]}{Z}. \tag{2.41}$$

where Tr is the trace of the matrix enclosed by the square bracket and Z is the grand partition function given by $Z = \mathrm{Tr}[e^{-\beta K}]$. The Hamiltonian, $K = H - \mu N$ with N being the number operator defined by $\sum_{n\mathbf{k}} f_{n\mathbf{k}}$ and $f_{n\mathbf{k}} = 0, 1$ is a single particle occupation. The chemical potential is given by μ. H is defined as

$$\begin{aligned} H &= H_0 + V, \\ H_0 &= H_{el} + H_{ph}, \\ H_{el} &= \sum_{n\mathbf{k}} \varepsilon_{n\mathbf{k}} c^\dagger_{n\mathbf{k}} c_{n\mathbf{k}}, \\ H_{ph} &= \sum_{\mathbf{q}\lambda} \omega_{\mathbf{q}\lambda} a^\dagger_{\mathbf{q}\lambda} a_{\mathbf{q}\lambda}. \end{aligned} \tag{2.42}$$

It will be convenient to separate K into solvable(K_0) and perturbation part (V) i.e. $K = K_0 + V$ where $K_0 = H_0 - \mu N$. The ground state i.e. eigenfunctions ($|\rangle_0$) and eigenenergies $\{\varepsilon_{n\mathbf{k}}, \omega_{\mathbf{q}\lambda}\}$ of K_0 are known. H_0 is further divided into electronic H_{el} and phononic H_{ph} Hamiltonians. The operators $c^\dagger_{n\mathbf{k}}$ and $c_{n\mathbf{k}}$ are the fermion creation and annihilation operator for state $|n\mathbf{k}\rangle$ respectively. Similarly, $a^\dagger_{\mathbf{q}\lambda}$ and $a_{\mathbf{q}\lambda}$ are the creation and annihilation operators for bosons corresponding to state $|\mathbf{q}\lambda\rangle$. V is the perturbation Hamiltonian which can be external potential, electron-electron or EP interaction depending upon the problem of interest.

Evaluating the average values of an operator as defined in Eq. (2.41) is not simple due to the perturbation hidden in K. So we rewrite Eq. (2.41)

$$\begin{aligned} \mathrm{Tr}[Ae^{-\beta K}] &= \mathrm{Tr}\left[e^{-\beta K_0}(e^{\beta K_0}Ae^{-\beta K_0})e^{\beta K_0}e^{-\beta K}\right], \\ &= \mathrm{Tr}\left[e^{-\beta K_0}A(\beta)S(\beta,0)\right]. \end{aligned} \tag{2.43}$$

Now, Tr is mostly expressed in solvable part i.e. K_0 and perturbation is treated in terms of $S(\beta, 0)$ called S-matrix. The term $e^{\beta K_0}Ae^{-\beta K_0}$ can be seen as time evolution of operator A with time $\beta = it = \tau$ [71]. $S(\beta, 0)$ contains the time evolution of the system when the perturbation is applied. It can be written for the two general imaginary times as $S(\tau, \tau') = e^{\tau K_0}e^{-\tau K}e^{\tau' K}e^{-\tau' K_0}$. The equation of motion of the S-matrix is given by

$$\begin{aligned} \frac{\partial S(\tau,\tau')}{\partial\tau} &= -e^{\tau K_0}Ve^{-\tau K}e^{\tau' K}e^{-\tau' K_0}, \\ &= -V(\tau)S(\tau,\tau'), \end{aligned} \tag{2.44}$$

and it has solution

$$\begin{aligned} S(\tau,\tau') &= \mathscr{T}\exp\left[-\int_{\tau'}^{\tau} d\tau_1 V(\tau_1)\right], \\ &= 1-\int_{\tau'}^{\tau} d\tau_1 V(\tau_1)+\frac{1}{2}\int_{\tau'}^{\tau} d\tau_1 d\tau_2 \mathscr{T}\{V(\tau_1)V(\tau_2)\}+\ldots, \\ &= \sum_{p=0}^{\infty}(-1)^p\frac{1}{p!}\int_{\tau'}^{\tau} d\tau_1\cdots\int_{\tau'}^{\tau} d\tau_p \mathscr{T}\{V(\tau_1)V(\tau_2)\ldots V(\tau_p)\}. \end{aligned} \tag{2.45}$$

We introduce $\mathscr{T}$ a time ordering operator. Its function will be explained belows. The system evolves from initial state $|\rangle_0$ at $\tau\to-\infty$ to the final state $|\rangle$ at $\tau=0$. This transformation is captured through S-matrix as $|\rangle = S(0,-\infty)|\rangle_0$. Generally speaking, though S-matix contains the V, yet it makes it possible to write the rest of the quantities in terms of known wavefunctions $|\rangle_0$. The grand partition function Z can be written for any general Hamiltonian K in S- matrix form as

$$\begin{aligned} Z &= \mathrm{Tr}[e^{-\beta K}], \\ &= \mathrm{Tr}[e^{-\beta K_0}e^{\beta K_0}e^{-\beta K}], \\ &= \mathrm{Tr}[e^{-\beta K_0}S(\beta,0)], \\ &= Z_0\langle|S(\beta,0)|\rangle_0, \end{aligned} \tag{2.46}$$

where $Z_0=\mathrm{Tr}[e^{-\beta K_0}]$ is the grand partition function for the unperturbed Hamiltonian. One can switch between Tr and quantum mechanical averages via $\langle|(...)|\rangle_0 = Z_0^{-1}\mathrm{Tr}[e^{-\beta K_0}(\ldots)]$.

Within the second-quantization, Green's function in the Heisenberg picture can be defined as follows

$$\mathscr{G}(n\mathbf{k},\tau-\tau') = -\langle|\mathscr{T}\{\tilde{c}_{n\mathbf{k}}(\tau)\tilde{c}^{\dagger}_{n\mathbf{k}}(\tau')\}|\rangle, \tag{2.47}$$

and

$$\mathscr{T}\{\tilde{c}_{n\mathbf{k}}(\tau)\tilde{c}^{\dagger}_{n\mathbf{k}}(\tau')\} = \left[\Theta(\tau-\tau')\tilde{c}_{n\mathbf{k}}(\tau)\tilde{c}^{\dagger}_{n\mathbf{k}}(\tau') - \Theta(\tau'-\tau)\tilde{c}^{\dagger}_{n\mathbf{k}}(\tau')\tilde{c}_{n\mathbf{k}}(\tau)\right]. \tag{2.48}$$

Now, we explain the action of time ordering operator $\mathscr{T}$. It arranges the time dependent operators from right to left in increasing order of time and $\Theta(\tau)$ is the heavyside step function. Whenever two fermion operators are interchanged, a minus sign is introduced. The physical interpretation of the Eq. (2.47) for the time ($\tau>\tau'$) is that operator $\tilde{c}^{\dagger}_{n\mathbf{k}}(\tau')$ adds a carrier in the system in state $|n\mathbf{k}\rangle$ at time τ'. It propagates in the system and interacts with the other particles. Later at time τ the same carrier is extracted from the state $|n\mathbf{k}\rangle$ with the operation of $\tilde{c}_{n\mathbf{k}}(\tau)$. $\mathscr{G}_{n\mathbf{k}}(\tau,\tau')$ eventually gives the probability/amplitude of the carrier in state $|n\mathbf{k}\rangle$ at time $\tau-\tau'$. The tilde $\tilde{}$ represents the operator in Heisenberg picture. It will be convenient to write Eq. (2.47) in interaction picture because operators and wavefunctions evolve as H_0 or K_0 there which can be solved and the unknown part V can be dealt with S-matrix. The operator in Heisenberg picture $\tilde{A}(\tau)$ is related to the operator in interaction picture $A(\tau)$ by

$$\tilde{A}(\tau) = e^{K\tau}e^{-K_0\tau}A(\tau)e^{K_0\tau}e^{-K\tau}. \tag{2.49}$$

Using the above transformation and the definition of averages in grand canonical ensembles from Eq. (2.41), $\mathscr{G}(\tau-\tau')$ of Eq.(2.47) can be rewritten as

$$\begin{aligned} \mathscr{G}(n\mathbf{k},\tau-\tau') &= -\frac{1}{Z}\mathrm{Tr}\left[e^{-\beta K}\mathscr{T}\{\tilde{c}_{n\mathbf{k}}(\tau)\tilde{c}^{\dagger}_{n\mathbf{k}}(\tau')\}\right], \\ &= -\frac{1}{Z}\mathrm{Tr}\Big[e^{-K_0\beta}\mathscr{T}\Big\{e^{K_0\beta}e^{-K\beta}e^{K\tau}e^{-K_0\tau}c_{n\mathbf{k}}(\tau)e^{K_0\tau}\times \\ &\qquad e^{-K\tau}e^{K\tau'}e^{-K_0\tau'}c^{\dagger}_{n\mathbf{k}}(\tau')e^{K_0\tau'}e^{-K\tau'}\Big\}\Big]. \end{aligned} \tag{2.50}$$

With the definition $S(\tau,\tau') = e^{\tau K_0}e^{-\tau K}e^{\tau' K}e^{-\tau' K_0}$, we write the Eq. (2.50) in terms of S-matrix that reads

$$\begin{aligned}\mathscr{G}(n\mathbf{k},\tau-\tau') &= -\frac{1}{Z}\mathrm{Tr}\left[e^{-K_0\beta}\mathscr{T}\{S(\beta,\tau)c_{n\mathbf{k}}(\tau)S(\tau,\tau')c^{\dagger}_{n\mathbf{k}}(\tau')S(\tau',0)\}\right],\\ &= -\frac{1}{Z}\mathrm{Tr}\left[e^{-K_0\beta}\mathscr{T}\{c_{n\mathbf{k}}(\tau)c_{n\mathbf{k}}(\tau')S(\beta,0)\}\right],\\ &= -\frac{Z_0}{Z}\langle|\mathscr{T}\left\{c_{n\mathbf{k}}(\tau)c_{n\mathbf{k}}(\tau')S(\beta,0)\right\}|\rangle_0.\end{aligned} \tag{2.51}$$

We used the property of S-matrix $S(\tau,\tau'') = S(\tau,\tau')S(\tau',\tau'')$, Eq. (2.46) and changing the Tr to average, we have

$$\mathscr{G}(n\mathbf{k},\tau-\tau') = -\frac{1}{\langle S(\beta,0)\rangle}\langle|\mathscr{T}\{\tilde{c}_{n\mathbf{k}}(\tau)\tilde{c}^{\dagger}_{n\mathbf{k}}(\tau')S(\beta,0)\}|\rangle_0, \tag{2.52}$$

and

$$\frac{1}{\langle|S(\beta,0)|\rangle_0} = 1 - \frac{1}{2!}\int_0^{\beta} d\tau d\tau'\langle|\mathscr{T}\{V(\tau)V(\tau')\}|\rangle_0 + \ldots. \tag{2.53}$$

It is very cumbersome to solve the Eq. (2.52) directly and instead it is solved using perturbative expansions of $\mathscr{G}(n\mathbf{k},\tau-\tau')$ in terms of S-matrix. For this we need to know the ground state Green's function for electrons and phonons before hand.

2.3.3 Bare electron Green's function

First, we consider the case of unperturbed system. With $V = 0$ and $S(\beta,0)$ becomes unity. Green's function for bare electron from Eq.(2.52) can be written as

$$\mathscr{G}^0(n\mathbf{k},\tau-\tau') = -\langle|\mathscr{T}\{c_{n\mathbf{k}}(\tau)c^{\dagger}_{n\mathbf{k}}(\tau')\}|\rangle_0. \tag{2.54}$$

The part of the Hamiltonian that matters for the bare electron is $H_{el} - \mu N$. The state of the electron corresponding to energy $\sum_{n\mathbf{k}} f_{n\mathbf{k}}\varepsilon_{n\mathbf{k}}$ is given by $\{f_{n\mathbf{k}}\}$. The ensemble average of right side of Eq. (2.54) is given by

$$\begin{aligned}\langle|\mathscr{T}c_{n\mathbf{k}}(\tau)c^{\dagger}_{n\mathbf{k}}(\tau')|\rangle_0 &= Z_{el}^{-1}\sum_{\{f_{n'\mathbf{k}'}\}}\langle\{f_{n'\mathbf{k}'}\}|e^{-\beta(H_{el}-\mu N)}\mathscr{T}\{c_{n\mathbf{k}}(\tau)c^{\dagger}_{n\mathbf{k}}(\tau')\}|\{f_{n'\mathbf{k}'}\}|\rangle_0,\\ &= Z_{el}^{-1}\sum_{\{f_{n'\mathbf{k}'}\}} e^{-\beta\sum_{n'\mathbf{k}'}f_{n'\mathbf{k}'}\varepsilon_{n'\mathbf{k}'}}e^{-\varepsilon_{n\mathbf{k}}(\tau-\tau')}\times\\ &\qquad \langle|\Theta(\tau-\tau')c_{n\mathbf{k}}(\tau)c^{\dagger}_{n\mathbf{k}}(\tau') - \Theta(\tau'-\tau)c^{\dagger}_{n\mathbf{k}}(\tau')c_{n\mathbf{k}}(\tau)|\rangle_0,\\ &= Z_{el}^{-1}\sum_{\{f_{n'\mathbf{k}'}\}} e^{-\beta\sum_{n'\mathbf{k}'}f_{n'\mathbf{k}'}\varepsilon_{n'\mathbf{k}'}}e^{-\varepsilon_{n\mathbf{k}}(\tau-\tau')}\times\\ &\qquad \left[\left(\Theta(\tau-\tau')(1-f_{n\mathbf{k}}\right) - \Theta(\tau'-\tau)f_{n\mathbf{k}}\right].\end{aligned} \tag{2.55}$$

The grand partition function Z_{el} is

$$\begin{aligned} Z_{el} &= \mathrm{Tr}[e^{-\beta(H_{el}-\mu N)}], \\ &= \sum_{\{f_{n\mathbf{k}}\}} \langle\{f_{n\mathbf{k}}\}|e^{-\beta(H_{el}-\mu N)}|\{f_{n\mathbf{k}}\}\rangle, \\ &= \sum_{\{f_{n\mathbf{k}}\}} e^{-\beta\sum_{n\mathbf{k}} f_{n\mathbf{k}}\varepsilon_{n\mathbf{k}}}, \\ &= \prod_{n\mathbf{k}}\sum_{f_{n\mathbf{k}}} e^{-\beta f_{n\mathbf{k}}\varepsilon_{n\mathbf{k}}}, \\ &= \prod_{n\mathbf{k}}(1+e^{-\beta\varepsilon_{n\mathbf{k}}}). \end{aligned} \tag{2.56}$$

First, we perform the sum over all $f_{n'\mathbf{k}'}$ except $f_{n'\mathbf{k}'} = f_{n\mathbf{k}}$ in the final term of Eq. (2.55) because of the presence of $n\mathbf{k}$. That would give us $\prod_{n\mathbf{k}}(1+e^{-\beta\varepsilon_{n\mathbf{k}}})/(1+e^{-\beta\varepsilon_{n\mathbf{k}}})\times$ the term containing summation over $n\mathbf{k}$. Putting Z_{el} from Eq. (2.56), Eq. (2.55) becomes

$$\begin{aligned} \langle|\mathscr{T}c_{n\mathbf{k}}(\tau)c^{\dagger}_{n\mathbf{k}}(\tau')|\rangle_0 = \frac{e^{-\beta\varepsilon_{n\mathbf{k}}}(\tau-\tau')}{1+e^{-\beta\varepsilon_{n\mathbf{k}}}}\sum_{\{f_{n\mathbf{k}}\}} e^{-f_{n\mathbf{k}}\beta\varepsilon_{n\mathbf{k}}}\times \\ [(1-f_{n\mathbf{k}})\Theta(\tau-\tau') - f_{n\mathbf{k}}\Theta(\tau'-\tau)]. \end{aligned} \tag{2.57}$$

Now, we perform sum over $f_{n\mathbf{k}} = 0$ and 1 and we have bare Green's function in imaginary time domain (τ)

$$\mathscr{G}^0(n\mathbf{k},\tau-\tau') = -e^{\varepsilon_{n\mathbf{k}}(\tau-\tau')}[\Theta(\tau-\tau') - f(\varepsilon_{n\mathbf{k}})]. \tag{2.58}$$

We take Fourier transformation of the Eq. (2.58) in energy domain, we get

$$\mathscr{G}^0(n\mathbf{k},\tau-\tau') = -[1-f(\varepsilon_{n\mathbf{k}})]\int_0^{\beta} d(\tau-\tau')e^{(i\omega_m-\varepsilon_{n\mathbf{k}})(\tau-\tau')}, \tag{2.59}$$

It should be noted that in case of fermions $\omega_m = (2m+1)\pi/\beta$ [Eq. (2.38)] which makes $e^{i\omega_m\beta} = -1$ and the numerator becomes 1 $\left[(e^{-\beta\varepsilon_{n\mathbf{k}}}+1) = (1-f(\varepsilon_{n\mathbf{k}}))^{-1}\right]$ and we finally arrive at

$$\mathscr{G}^0(n\mathbf{k},i\omega_m) = \frac{1}{i\omega_m - \varepsilon_{n\mathbf{k}}}. \tag{2.60}$$

Eq. (2.60) is the non-interacting Green's function for bare electrons and depends upon temperature through ω_m. Two properties of Green's function can be immediately seen from the above equation

- The poles of the Green's function give eigenenergies in non-interacting case and quasi particle excitations in case of interacting Green's function.
- Imaginary part of Green's function is directly proportional to the electronic DOS.

2.3.4 Bare phonon Green's function

Next, we define the Green's function for bare phonon within the Harmonic approximation as

$$\mathscr{D}^0(\mathbf{q}\lambda,\tau-\tau') = -\langle|\mathscr{T}\{A_{\mathbf{q}\lambda}(\tau)A_{-\mathbf{q}\lambda}(\tau')\}|\rangle_0. \tag{2.61}$$

where, $A_{\mathbf{q}\lambda}(\tau)$ is a phonon operator defined in terms of boson creation and annihilation operators as $A_{\mathbf{q}\lambda}(\tau) = a_{\mathbf{q}\lambda}(\tau) + a^{\dagger}_{-\mathbf{q}\lambda}(\tau)$. The time evolution of the operator is given by

$$A_{\mathbf{q}\lambda}(\tau) = e^{-\omega_{\mathbf{q}\lambda}\tau}a_{\mathbf{q}\lambda}(0) + e^{\omega_{\mathbf{q}\lambda}\tau}a^{\dagger}_{-\mathbf{q}\lambda}(0). \tag{2.62}$$

The grand partition function for the phonon is defined as $Z_{ph} = \mathrm{Tr}[e^{-\beta H_{ph}}]$ and H_{ph} is used instead of $H_0 - \mu N$. The terms with the combination of $\langle|a_{\mathbf{q}\lambda}a_{\mathbf{q}\lambda}|\rangle_0$ and $\langle|a^\dagger_{\mathbf{q}\lambda}a^\dagger_{\mathbf{q}\lambda}|\rangle_0$ in Eq. (2.61) will vanish and only the terms containing $\langle|a_{\mathbf{q}\lambda}a^\dagger_{\mathbf{q}\lambda}|\rangle_0$ and $\langle|a^\dagger_{\mathbf{q}\lambda}a_{\mathbf{q}\lambda}|\rangle_0$ will survive. Following exactly the similar procedure as in case of bare electron's Green function, we arrive at The bare phonon Green's function take the form

$$\begin{aligned}\mathscr{D}^0(\mathbf{q}\lambda, \tau - \tau') = &-\Theta(\tau - \tau')\left[(N(\omega_{\mathbf{q}\lambda}) + 1)e^{-\omega_{\mathbf{q}\lambda}(\tau-\tau')} + N(\omega_{\mathbf{q}\lambda})e^{\omega_{\mathbf{q}\lambda}(\tau-\tau')}\right] \\ &-\Theta(\tau' - \tau)\left[(N(\omega_{\mathbf{q}\lambda}) + 1)e^{-\omega_{\mathbf{q}\lambda}(\tau'-\tau)} + N(\omega_{\mathbf{q}\lambda})e^{\omega_{\mathbf{q}\lambda}(\tau'-\tau)}\right].\end{aligned} \tag{2.63}$$

On taking the Fourier transformation of the Eq. (2.63) in energy space, we get for the bare phonon Green's function

$$\mathscr{D}^0(\mathbf{q}\lambda, i\omega_m) = -\left[(N(\omega_{\mathbf{q}\lambda}) + 1)\frac{(e^{-(\omega_{\mathbf{q}\lambda} - i\omega_m)\beta} - 1)}{i\omega_m - \omega_{\mathbf{q}\lambda}} + N(\omega_{\mathbf{q}\lambda})\frac{(e^{(\omega_{\mathbf{q}\lambda} + i\omega_m)\beta} - 1)}{i\omega_m + \omega_{\mathbf{q}\lambda}}\right]. \tag{2.64}$$

From Eq. (2.38), we know that in case of bosons $\omega_m = 2\pi m/\beta$, which makes $e^{(i\omega_m\beta)} = 1$. We also use the $N(\omega_{\mathbf{q}\lambda}) + 1 = 1/1 - e^{-\beta\omega_{\mathbf{q}\lambda}}$ and finally arrive at the non-interacting phonon Green's function.

$$\begin{aligned}\mathscr{D}^0(\mathbf{q}\lambda, \omega) &= -\left[-\frac{1}{i\omega_m - \omega_{\mathbf{q}\lambda}} + \frac{1}{i\omega_m + \omega_{\mathbf{q}\lambda}}\right], \\ &= -\frac{2\omega_{\mathbf{q}\lambda}}{\omega_m^2 + \omega_{\mathbf{q}\lambda}^2}.\end{aligned} \tag{2.65}$$

2.3.5 Electron-phonon interaction

So far, we have defined the bare Green's function for electron and phonon. Let's have a look on the perturbative expansion of Eq. (2.52). For this purpose, we choose EP interaction as a perturbation V defined by

$$V = \sum_{\substack{\mathbf{kq}\\ \lambda nm}} g^{nm}_\lambda(\mathbf{k}, \mathbf{q}) c^\dagger_{m\mathbf{k}+\mathbf{q}}(\tau) c_{n\mathbf{k}}(\tau)(a_{\mathbf{q}\lambda}(\tau) + a^\dagger_{-\mathbf{q}\lambda}(\tau)), \tag{2.66}$$

where the EP matrix elements are described as [49]

$$g^{nm}_\lambda(\mathbf{k}, \mathbf{q}) = \langle|u_{m\mathbf{k}+\mathbf{q}}|\triangle V^{\mathrm{KS}}_{\mathbf{q}\lambda}|u_{n\mathbf{k}}|\rangle_0. \tag{2.67}$$

It provides information about the scattering of the state $|n\mathbf{k}\rangle$ to $|m\mathbf{k} + \mathbf{q}\rangle$ via scattering potential $\triangle V^{\mathrm{KS}}_{\mathbf{q}\lambda}$. The scattering is accompanied by either absorption or emission of a phonon of energy $\omega_{\mathbf{q}\lambda}$. We are interested in the perturbative expansion of Eq. (2.52) in terms of S-matrix [see Eq. (2.53)] up to second order only and it leads to

$$\begin{aligned}\mathscr{G}(n\mathbf{k}, \tau - \tau') = \mathscr{G}^0(n\mathbf{k}, \tau - \tau') + (-1)^2 \int_0^\beta d\tau_1 \langle|\mathscr{T}\left\{c_{n\mathbf{k}}(\tau)V(\tau_1)c^\dagger_{n\mathbf{k}}(\tau')\right\}|\rangle_0 + \\ \frac{(-1)^3}{2!}\int_0^\beta d\tau_1 \int_0^\beta d\tau_2 \langle|\mathscr{T}\left\{c_{n\mathbf{k}}(\tau)V(\tau_1)V(\tau_2)c^+_{n\mathbf{k}}(\tau')\right\}|\rangle_0 - \\ \frac{1}{2}\mathscr{G}^0(n\mathbf{k}, \tau - \tau')\int_0^\beta d\tau_1 d\tau_2 \langle|\mathscr{T}\left\{V(\tau_1)V(\tau_2)\right\}|\rangle_0 \ldots\end{aligned} \tag{2.68}$$

The second term on the left hand side of the Eq. (2.68) containing $V(\tau_1)$ will have $\langle|a_{\mathbf{q}\lambda}(\tau_1)|\rangle_0$ which will vanish. Fermionic and bosonic operators commute with each other. It is possible to separate these

operators without any pairing. For the time being, let us focus on the third term of right hand side. The fourth term arises from $1/\langle|S(\beta,0)|\rangle_0$ and we will get back to it later.

$$\langle|\mathscr{T}\left\{c_{n\mathbf{k}}(\tau)V(\tau_1)V(\tau_2)c^\dagger_{n\mathbf{k}}(\tau')\right\}|\rangle_0 = \sum_{\substack{\mathbf{k_1q_1}\\ \lambda_1 n_1 m_1}}\sum_{\substack{\mathbf{k_2q_2}\\ \lambda_2 n_2 m_2}} g^{n_1m_1}_{\lambda_1}(\mathbf{k_1},\mathbf{q_1})g^{n_2m_2}_{\lambda_2}(\mathbf{k_2},\mathbf{q_2}) \langle|\mathscr{T}\left\{A_{\mathbf{q}_1\lambda_1}(\tau_1)A_{\mathbf{q}_2\lambda_2}(\tau_2)\right\}|\rangle_0 \times \underbrace{\langle|\mathscr{T}\left\{c_{n\mathbf{k}}(\tau)c^\dagger_{m_1\mathbf{k_1+q_1}}(\tau_1)c_{m_1\mathbf{k_1}}(\tau_1)c^\dagger_{m_2\mathbf{k_2+q_2}}(\tau_2)c_{m_2\mathbf{k_2}}(\tau_2)c_{n\mathbf{k}}(\tau')\right\}|\rangle_0}_{\mathscr{P}}. \tag{2.69}$$

The product of phonon operators gives bare phonon Green's function with $\mathbf{q_1} = -\mathbf{q_2} = \mathbf{q}$

$$\langle|T\{A_{\mathbf{q}_1\lambda_1}(\tau_1)A_{\mathbf{q}_2\lambda_2}(\tau_2)\}|\rangle_0 = -\delta_{\mathbf{q_1+q_2=0}}\mathscr{D}^0(\mathbf{q}\lambda,\tau_1-\tau_2). \tag{2.70}$$

The Eq. (2.70) is simple, we have only two operators. This scenario becomes complicated when there are many operators and several combinations are possible. $\mathscr{P}$ contains 3 creation and three annihilation operators with four different times. It is not possible to arrange the operators randomly. Pairing of creation and annihilation operators is done using Wick's theorem. Here, we summarize some rules of Wick's theorem

- There must be same number of creation and annihilation operators so that system is brought back to the ground state after all the operations. The pairing is done between creation and annihilation operators only, no two same type of operators can be paired together.
- Whenever two fermionic operators are interchanged, a minus sign is introduced. This is important because one has to keep track of changes made with respect to the original assembly of operators to reach at final pairing. Though this is not required for bosonic operators.
- When two paired operators have the same time argument, it leads to the number operator $f(\varepsilon_{n\mathbf{k}})$ or $N(\omega_{\mathbf{q}\lambda})$ depending upon the operators. For example:

$$\langle|\mathscr{T}\{c_{n\mathbf{k}_1}(\tau)c^\dagger_{m\mathbf{k}_2}(\tau)\}|\rangle_0 = -\delta_{n,m}\delta_{\mathbf{k_1=k_2=k}}f(\varepsilon_{n\mathbf{k}}). \tag{2.71}$$

Using the above rules, $\mathscr{P}$ will have 3! combinations as shown below

$$\begin{aligned}
\mathscr{P} = {} & \langle|\mathscr{T}\{c_{n\mathbf{k}}(\tau)c^\dagger_{m_1\mathbf{k_1+q_1}}(\tau_1)\}|\rangle_0\ \langle|\mathscr{T}\{c_{n_1\mathbf{k_1}}(\tau_1)c^\dagger_{m_2\mathbf{k_2+q_2}}(\tau_2)\}|\rangle_0\ \langle|\mathscr{T}\{c_{n_2\mathbf{k_2}}(\tau_2)c^\dagger_{n\mathbf{k}}(\tau')\}|\rangle_0 \\
& + \langle|\mathscr{T}\{c_{n\mathbf{k}}(\tau)c^\dagger_{m_2\mathbf{k_2+q_2}}(\tau_2)\}|\rangle_0\ \langle|\mathscr{T}\{c_{n_2\mathbf{k_2}}(\tau_2)c^\dagger_{m_1\mathbf{k_1+q_1}}(\tau_1)\}|\rangle_0\ \langle|\mathscr{T}\{c_{n_1\mathbf{k_1}}(\tau_1)c^\dagger_{n\mathbf{k}}(\tau')\}|\rangle_0 \\
& + \langle|\mathscr{T}\{c_{n\mathbf{k}}(\tau')c^\dagger_{m_1\mathbf{k_1+q_1}}(\tau_1)\}|\rangle_0\ \langle|\mathscr{T}\{c_{n_1\mathbf{k_1}}(\tau_1)c^\dagger_{n\mathbf{k}}(\tau)\}|\rangle_0\ \langle|\mathscr{T}\{c_{n_2\mathbf{k_2}}(\tau_2)c^\dagger_{m_2\mathbf{k_2+q_2}}(\tau_2)\}|\rangle_0 \\
& + \langle|\mathscr{T}\{c_{n\mathbf{k}}(\tau')c^\dagger_{m_2\mathbf{k_2+q_2}}(\tau_2)\}|\rangle_0\ \langle|\mathscr{T}\{c_{n_1\mathbf{k_1}}(\tau_1)c^\dagger_{m_1\mathbf{k_1+q_1}}(\tau_1)\}|\rangle_0\ \langle|\mathscr{T}\{c_{n_2\mathbf{k_2}}(\tau_2)c^\dagger_{n\mathbf{k}}(\tau)\}|\rangle_0 \\
& + \langle|\mathscr{T}\{c_{n\mathbf{k}}(\tau)c^\dagger_{n\mathbf{k}}(\tau')\}|\rangle_0\ \langle|\mathscr{T}\{c_{n_1\mathbf{k_1}}(\tau_1)c^\dagger_{m_1\mathbf{k_1+q_1}}(\tau_1)\}|\rangle_0\ \langle|\mathscr{T}\{c_{n_2\mathbf{k_2}}(\tau_2)c^\dagger_{m_2\mathbf{k_2+q_2}}(\tau_2)\}|\rangle_0 \\
& - \langle|\mathscr{T}\{c_{n\mathbf{k}}(\tau)c^\dagger_{n\mathbf{k}}(\tau')\}|\rangle_0\ \langle|\mathscr{T}\{c_{n_1\mathbf{k_1}}(\tau_1)c^\dagger_{m_2\mathbf{k_2+q_2}}(\tau_2)\}|\rangle_0\ \langle|\mathscr{T}\{c_{n_2\mathbf{k_2}}(\tau_2)c^\dagger_{m_1\mathbf{k_1+q_1}}(\tau_1)\}|\rangle_0.
\end{aligned} \tag{2.72}$$

With the definition of electron Green's function from Eq. (2.54) and Eq. (2.71) $\mathscr{P}$ can be written in terms of Green's function and number operator $f(\varepsilon_{n\mathbf{k}})$ as

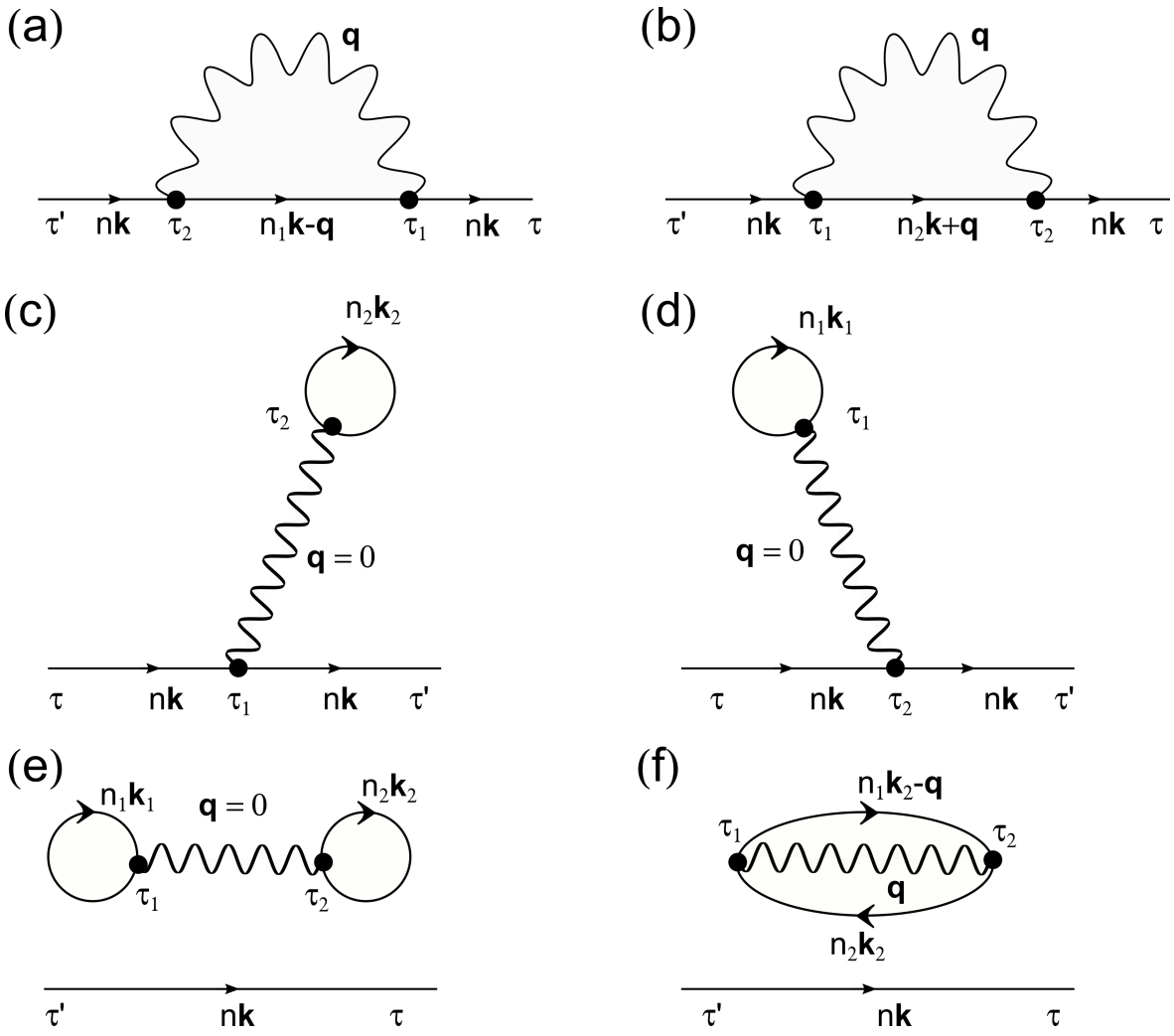

Figure 2.1: Feynman diagrams for electron Green's function for second order in EP interaction.

$$
\begin{aligned}
\mathscr{P} = \\
&- \mathscr{G}^0(n\mathbf{k}, \tau - \tau_1)\delta_{n,m_1}\delta_{\mathbf{k},\mathbf{k_1}+\mathbf{q}}\, \mathscr{G}^0(n_1\mathbf{k_1}, \tau_1 - \tau_2)\delta_{n_1,m_2}\delta_{\mathbf{k_1},\mathbf{k_2}-\mathbf{q}}\, \mathscr{G}^0(n_2\mathbf{k_2}, \tau_2 - \tau')\delta_{n_2,n}\delta_{\mathbf{k_2},\mathbf{k}} \\
&- \mathscr{G}^0(n\mathbf{k}, \tau - \tau_2)\delta_{n,m_2}\delta_{\mathbf{k},\mathbf{k_2}-\mathbf{q}}\, \mathscr{G}^0(n_2\mathbf{k_2}, \tau_2 - \tau_1)\delta_{n_2,m_1}\delta_{\mathbf{k_2},\mathbf{k_1}+\mathbf{q}}\, \mathscr{G}^0(n_1\mathbf{k_1}, \tau_1 - \tau')\delta_{n_1,n}\delta_{\mathbf{k_1},\mathbf{k}} \\
&- \mathscr{G}^0(n\mathbf{k}, \tau' - \tau_1)\delta_{n,m_1}\delta_{\mathbf{k},\mathbf{k_1}+\mathbf{q}}\, \mathscr{G}^0(n_1\mathbf{k_1}, \tau_1 - \tau)\delta_{n_1,n}\delta_{\mathbf{k_1},\mathbf{k}}\, f(\varepsilon_{n_2\mathbf{k_2}})\delta_{n_2,m_2}\delta_{\mathbf{k_2},\mathbf{k_2}-\mathbf{q}} \\
&- \mathscr{G}^0(n\mathbf{k}, \tau' - \tau_2)\delta_{n,m_2}\delta_{\mathbf{k},\mathbf{k_2}-\mathbf{q}}\, f(\varepsilon_{n_1\mathbf{k_1}})\delta_{n_1,m_1}\delta_{\mathbf{k_1},\mathbf{k_1}+\mathbf{q}}\, \mathscr{G}^0(n_2\mathbf{k_2}, \tau_2 - \tau)\delta_{n_2,n}\delta_{\mathbf{k_2},\mathbf{k}} \\
&- \mathscr{G}^0(n\mathbf{k}, \tau - \tau')\, f(n_1\mathbf{k_1})\delta_{n_1,m_1}\delta_{\mathbf{k_1},\mathbf{k_1}+\mathbf{q}}\, f(\varepsilon_{n_2\mathbf{k_2}})\delta_{n_2,m_2}\delta_{\mathbf{k_2},\mathbf{k_2}+\mathbf{q}} \\
&+ \mathscr{G}^0(n\mathbf{k}, \tau - \tau')\, \mathscr{G}^0(n_1\mathbf{k_1}, \tau_1 - \tau_2)\delta_{n_1,m_2}\delta_{\mathbf{k_1},\mathbf{k_2}-\mathbf{q}}\, \mathscr{G}^0(n_2\mathbf{k_2}, \tau_2 - \tau_1)\delta_{n_2,m_1}\delta_{\mathbf{k_2},\mathbf{k_1}+\mathbf{q}}.
\end{aligned}
\tag{2.73}
$$

After having $\mathscr{P}$ in terms of Green's function, it can be represented in Feynman diagrams for better visualization. We explain the notations for Feynman diagrams briefly. The Green's function $\mathscr{G}^0(n\mathbf{k}, (\tau - \tau')$ is shown by a straight line going from $\tau' \to \tau$. Phonon Green's function is shown by wiggled line without any arrow because a phonon can travel both forward and backward in time due to presence of $a_{\mathbf{q}\lambda}$ and $a_{-\mathbf{q}\lambda}$ in $A_{\mathbf{q}\lambda}$. The occupation number is drawn by a circle with the arrow on it. The bullet ($\bullet$) in our case represents the EP matrix elements $g^{mn}_{\lambda}(\mathbf{k}, \mathbf{q})$. We simplify all the delta functions in Eq.(2.73) and express main quantities in terms of initial momentum $\mathbf{k}$ whenever possible.

Feynman diagrams of whole Eq.(2.73) are shown in the Fig. 2.1 and diagrams are ordered in the same way as the right side of Eq.(2.73) is written.

Fig. 2.1(a)-(d) are called connected Feynman diagrams and Fig. 2.1(e)-(f) are called disconnected Feynman diagrams. Let's have a look on these diagrams one by one. Fig. 2.1(a) which corresponds to the first term Eq.(2.73) describes a particle entering the system at initial time τ' in state $|n\mathbf{k}\rangle$ and travels to time τ_2 keeping the same initial state. At time τ_2 it emits a phonon with momentum $\mathbf{q}$ into the system. This leads to the transition of particle's state from $|n\mathbf{k}\rangle \rightarrow |n\mathbf{k}-\mathbf{q}\rangle$ and it continues to propagate till time τ_1. At τ_1, it absorbs the same phonon and returns to its initial state i.e. $|n\mathbf{k}-\mathbf{q}\rangle \rightarrow |n\mathbf{k}\rangle$ and finally it is taken out of system at time τ. It should be noted that the EP matrix elements at time τ_1 and τ_2 must be complex conjugate of each other because they lead to same transitions once out of state $|n\mathbf{k}\rangle$ and secondly into the state $|n\mathbf{k}\rangle$. Fig. 2.1(b) is same as that of (a) because here the carrier first absorbs a phonon and later emits and they differ in labelling only. This is related to the property of EP matrix elements $g_\lambda^{mn}(\mathbf{k},\mathbf{q}) = g_\lambda^{mn}(\mathbf{k},-\mathbf{q})$. Such diagrams are called topologically equal diagrams.

Fig. 2.1(c),(d) and (e) involves phonon with zero momentum, these diagrams don't involve particle's interaction with phonon since particle stays in the same state $|n\mathbf{k}\rangle$ between time $|\tau-\tau'|$. This introduces static strain in the system which is not included in the Hamiltonian. Finally, Fig. 2.1(f) implies that at time τ_1 an electron and phonon with the momentum $\mathbf{k_2}-\mathbf{q}$ and $\mathbf{q}$ are created respectively and at time τ_2 an electron with momentum $\mathbf{k_2}$ is destroyed. Speaking in terms of mathematical expressions, Fig. 2.1(c) and (d) are topologically same and end up giving constant times bare electron Green's function. This will give us an additive constant in the Eq. (2.68) which is set to zero. On the other hand, Fig. 2.1(e) and (f) will cancel with the fourth term of Eq. (2.68). We are simply left with the first two topologically same Feynman diagrams. On adding they cancel the factor of 2 in Eq. (2.68) and we have

$$\begin{aligned}\mathscr{G}(n\mathbf{k},\tau-\tau') = \mathscr{G}^0(n\mathbf{k},\tau-\tau') - \sum_{\mathbf{q}\lambda n_1}\int_0^\beta d\tau_1\int_0^\beta d\tau_2 \mathscr{D}^0(\mathbf{q}\lambda,\tau_1-\tau_2)\times \\ \left[g_\lambda^{nn_1}(\mathbf{k}-\mathbf{q},\mathbf{q})g_\lambda^{n_1 n}(\mathbf{k},-\mathbf{q})\mathscr{G}^0(n\mathbf{k},\tau-\tau_1)\right. \\ \left.\mathscr{G}^0(n_1\mathbf{k}-\mathbf{q},\tau_1-\tau_2)\mathscr{G}^0(n\mathbf{k},\tau_2-\tau')\right].\end{aligned} \tag{2.74}$$

It can be shown that

$$g_\lambda^{nn_1}(\mathbf{k},\mathbf{q}) = \langle u_{n_1\mathbf{k}}|\triangle V_{\mathbf{q}\lambda}^{\mathrm{KS}}|u_{n\mathbf{k}+\mathbf{q}}\rangle = g_\lambda^{\dagger n_1 n}(\mathbf{k}+\mathbf{q},-\mathbf{q}). \tag{2.75}$$

where, (†) denotes the complex conjugate. For simplification, we change the index $n_1 \rightarrow m$ and Eq. (2.74) reduces to

$$\begin{aligned}\mathscr{G}(n\mathbf{k},\tau-\tau') = \mathscr{G}^0(n\mathbf{k},\tau-\tau') - \sum_{\mathbf{q}\lambda m}|g_{\lambda,nm}(\mathbf{k},\mathbf{q})|^2\int_0^\beta d\tau_1\int_0^\beta d\tau_2 \mathscr{D}^0(\mathbf{q}\lambda,\tau_1-\tau_2)\times \\ \mathscr{G}^0(n\mathbf{k},\tau-\tau_2)\mathscr{G}^0(m\mathbf{k}+\mathbf{q},\tau_2-\tau_1)\mathscr{G}^0(n\mathbf{k},\tau_1-\tau').\end{aligned} \tag{2.76}$$

On taking the Fourier transformation of the above equation using the definition from Eq. (2.39)

$$\begin{aligned}\frac{1}{\beta}\sum_{j} e^{-i\omega_j(\tau-\tau')}\mathscr{G}(n\mathbf{k},i\omega_j) = \frac{1}{\beta}\sum_{l} e^{-i\omega_l(\tau-\tau')}\mathscr{G}^0(n\mathbf{k},i\omega_l) - \frac{1}{\beta^4}\sum_{\mathbf{q}\lambda m}|g_{\lambda,nm}(\mathbf{k},\mathbf{q})|^2\times \\ \Bigg[\int_0^\beta d\tau_1\int_0^\beta d\tau_2\sum_p e^{-i\omega_p(\tau_1-\tau_2)}\mathscr{D}^0(\mathbf{q}\lambda,i\omega_p)\times \\ \sum_y e^{-i\omega_y(\tau-\tau_2)}\mathscr{G}^0(n\mathbf{k},i\omega_y)\sum_r e^{-i\omega_r(\tau-\tau_2)}\mathscr{G}^0(m\mathbf{k}+\mathbf{q},i\omega_r)\times \\ \sum_s e^{-i\omega_s(\tau_1-\tau')}\mathscr{G}^0(n\mathbf{k},i\omega_s)\Bigg].\end{aligned} \tag{2.77}$$

After collecting the exponents of τ_1 and τ_2. Using delta function definition from Eq. (2.40), the integral over τ_1 will lead to $\beta\delta(\omega_p+\omega_s-\omega_r)$ and for τ_2 we will have $\beta\delta(\omega_r-\omega_p-\omega_y)$. We change $\omega_r\to\omega_p+\omega_s$ and $\omega_y=\omega_s$, Eq. (2.77) can be simplified to

$$\begin{aligned}\sum_j e^{i\omega_j(\tau-\tau')}\mathscr{G}(n\mathbf{k},i\omega_j) = \sum_l e^{i\omega_l(\tau-\tau')}\mathscr{G}^0(n\mathbf{k},i\omega_l) - \\ \sum_{\mathbf{q}\lambda m}|g_\lambda^{nm}(\mathbf{k},\mathbf{q})|^2\sum_s e^{-i\omega_s(\tau-\tau')}\mathscr{G}^0(n\mathbf{k},i\omega_s)\times \\ \left[\frac{1}{\beta}\sum_p \mathscr{D}^0(\mathbf{q}\lambda,i\omega_p)\mathscr{G}^0(m\mathbf{k}+\mathbf{q},i(\omega_s+\omega_p))\right]\mathscr{G}^0(n\mathbf{k},i\omega_s).\end{aligned} \tag{2.78}$$

We again change indices $l,j\to s$, we can write Eq. (2.78) as

$$\mathscr{G}(n\mathbf{k},i\omega_s) = \mathscr{G}^0(n\mathbf{k},i\omega_s) + \mathscr{G}^0(n\mathbf{k},i\omega_s)\Sigma(n\mathbf{k},i\omega_s)\mathscr{G}^0(n\mathbf{k},i\omega_s), \tag{2.79}$$

here, $\Sigma(n\mathbf{k},i\omega_s)$ is called particle's self-energy from EP interaction.

$$\Sigma(n\mathbf{k},i\omega_s) = -\frac{1}{\beta}\sum_{\mathbf{q}\lambda m}|g_\lambda^{nm}(\mathbf{k},\mathbf{q})|^2\sum_p \mathscr{D}^0(\mathbf{q}\lambda,i\omega_p)\mathscr{G}^0(m\mathbf{k}+\mathbf{q},i(\omega_s+\omega_p)). \tag{2.80}$$

Let's denote the term in $\Sigma(n\mathbf{k},i\omega_s)$ which involves the summation over imaginary frequency p by $\mathscr{S}$. We will evaluate the sum using contour integration and residue theorems. We consider here sum over p as sum over Bose-Einstein occupation $N(z)=1/(e^{\beta z}-1)$, which has poles at the points $z_p=2\pi ip/\beta$ with $p=0,\pm1,\pm2,\ldots$ Eq. (2.37).

$$\begin{aligned}\mathscr{S}(z) &= \mathscr{D}^0(\mathbf{q}\lambda,z)\mathscr{G}^0(m\mathbf{k}+\mathbf{q},i\omega_s+z), \\ &= \frac{2\omega_{\mathbf{q}\lambda}}{z^2-\omega_{\mathbf{q}\lambda}^2}\times\frac{1}{i\omega_s+z-\varepsilon_{m\mathbf{k}+\mathbf{q}}}.\end{aligned} \tag{2.81}$$

However, $\mathscr{S}$ has three poles at $z=\pm\omega_{\mathbf{q}\lambda},\varepsilon_{m\mathbf{k}+\mathbf{q}}-i\omega_s$. These poles don't coincide with the poles of $N(z)$, so the summation can be changed into integration by

$$\sum_p \mathscr{S}(z) = \frac{\beta}{2\pi i}\oint_C dz\mathscr{S}(z)N(z), \tag{2.82}$$

where, C is the circle enclosing all the residues. $\mathscr{S}(z)$ goes to zero as $|z| \to \infty$ because of its $1/|z|^2$ dependence. The integral over the contour is given $(-2\pi i)$ times the sum over the residues. We denote the residues $\mathscr{R}_1$, $\mathscr{R}_3$ and $\mathscr{R}_3$ originating from the poles $+\omega_{\mathbf{q}\lambda}$, $-\omega_{\mathbf{q}\lambda}$ and $\varepsilon_{m\mathbf{k}+\mathbf{q}} - i\omega_s$

$$\begin{aligned}
\mathscr{R}_1 &= \frac{N(\omega_{\mathbf{q}\lambda})}{i\omega_s - \varepsilon_{m\mathbf{k}+\mathbf{q}} + \omega_{\mathbf{q}\lambda}}, \\
\mathscr{R}_2 &= \frac{N(\omega_{\mathbf{q}\lambda}) + 1}{i\omega_s - \varepsilon_{m\mathbf{k}+\mathbf{q}} - \omega_{\mathbf{q}\lambda}}, \\
\mathscr{R}_3 &= \frac{-2\omega_{\mathbf{q}\lambda} N(\varepsilon_{m\mathbf{k}+\mathbf{q}} - i\omega_p)}{(i\omega_s - \varepsilon_{m\mathbf{k}+\mathbf{q}})^2 - \omega_{\mathbf{q}\lambda}^2}, \\
&= \left[\frac{f(\varepsilon_{m\mathbf{k}+\mathbf{q}})}{i\omega_s - \varepsilon_{m\mathbf{k}+\mathbf{q}} + \omega_{\mathbf{q}\lambda}} - \frac{f(\varepsilon_{m\mathbf{k}+\mathbf{q}})}{i\omega_s - \varepsilon_{m\mathbf{k}+\mathbf{q}} - \omega_{\mathbf{q}\lambda}} \right].
\end{aligned} \tag{2.83}$$

The boson occupation and Fermi occupation are related through

$$\begin{aligned}
N(\varepsilon_{m\mathbf{k}+\mathbf{q}} - i\omega_p) &= 1/(e^{\beta(\varepsilon_{m\mathbf{k}+\mathbf{q}} - i\omega_p)} - 1), \\
&= -1/e^{\beta\varepsilon_{m\mathbf{k}+\mathbf{q}}} + 1, \\
&= -f(\varepsilon_{m\mathbf{k}+\mathbf{q}}).
\end{aligned} \tag{2.84}$$

On adding all the residues, and plugging it in Eq. (2.82) becomes

$$\sum_p \mathscr{S}(i\omega_p) = -\beta \left[\frac{N(\omega_{\mathbf{q}\lambda}) - f(\varepsilon_{m\mathbf{k}+\mathbf{q}}) + 1}{i\omega_s - \varepsilon_{m\mathbf{k}+\mathbf{q}} - \omega_{\mathbf{q}\lambda}} + \frac{N(\omega_{\mathbf{q}\lambda}) + f(\varepsilon_{m\mathbf{k}+\mathbf{q}})}{i\omega_s - \varepsilon_{m\mathbf{k}+\mathbf{q}} + \omega_{\mathbf{q}\lambda}} \right]. \tag{2.85}$$

Using Eq. (2.85) into the Eq. (2.80), self-energy $\Sigma(n\mathbf{k}, i\omega_s)$ can be written as

$$\Sigma(n\mathbf{k}, i\omega_s) = \sum_{\mathbf{q}\lambda m} |g_\lambda^{nm}(\mathbf{k}, \mathbf{q})|^2 \left[\frac{N(\omega_{\mathbf{q}\lambda}) - f(\varepsilon_{m\mathbf{k}+\mathbf{q}}) + 1}{i\omega_s - \varepsilon_{m\mathbf{k}+\mathbf{q}} - \omega_{\mathbf{q}\lambda}} + \frac{N(\omega_{\mathbf{q}\lambda}) + f(\varepsilon_{m\mathbf{k}+\mathbf{q}})}{i\omega_s - \varepsilon_{m\mathbf{k}+\mathbf{q}} + \omega_{\mathbf{q}\lambda}} \right]. \tag{2.86}$$

For the analytical continuation of Eq. (2.86) on the real axis $i\omega_s$ is changed to $\omega_s + i\delta$ where $i\delta$ is a small positive number. We evaluate the Eq. (2.86) for the energies of the state $|n\mathbf{k}\rangle$ only i.e $\omega_s = \varepsilon_{n\mathbf{k}}$. We change the notation from $\Sigma(n\mathbf{k}, \varepsilon_{n\mathbf{k}})$ to $\Sigma_{n\mathbf{k}}(T)$ and temperature (T) enters from the bosons and fermion occupation.

$$\Sigma_{n\mathbf{k}}(T) = \sum_{\mathbf{q}\lambda m} |g_\lambda^{nm}(\mathbf{k}, \mathbf{q})|^2 \left[\frac{N(\omega_{\mathbf{q}\lambda}, T) - f(\varepsilon_{m\mathbf{k}+\mathbf{q}}, T) + 1}{\varepsilon_{n\mathbf{k}} - \varepsilon_{m\mathbf{k}+\mathbf{q}} - \omega_{\mathbf{q}\lambda} + i\delta} + \frac{N(\omega_{\mathbf{q}\lambda}, T) + f(\varepsilon_{m\mathbf{k}+\mathbf{q}}, T)}{\varepsilon_{n\mathbf{k}} - \varepsilon_{m\mathbf{k}+\mathbf{q}} + \omega_{\mathbf{q}\lambda} + i\delta} \right]. \tag{2.87}$$

The Eq. (2.87) is a complex quantity and its imaginary part can be separated

$$\begin{aligned}
\mathrm{Im}[\Sigma_{n\mathbf{k}}(T)] = \sum_{\mathbf{q}\lambda m} |g_\lambda^{nm}(\mathbf{k}, \mathbf{q})|^2 \, &[(N(\omega_{\mathbf{q}\lambda}, T) + f(\varepsilon_{m\mathbf{k}+\mathbf{q}}, T)\delta(\varepsilon_{n\mathbf{k}} - \varepsilon_{m\mathbf{k}+\mathbf{q}} + \omega_{\mathbf{q}\lambda})] + \\
&[(N(\omega_{\mathbf{q}\lambda}, T) + 1 - f(\varepsilon_{m\mathbf{k}+\mathbf{q}}, T))\delta(\varepsilon_{n\mathbf{k}} - \varepsilon_{m\mathbf{k}+\mathbf{q}} - \omega_{\mathbf{q}\lambda})] \,.
\end{aligned} \tag{2.88}$$

It is clear from the above equation that $\mathrm{Im}[\Sigma_{n\mathbf{k}}(T)]$ will follow the electronic DOS as it provides the available phase space for the EP scattering events to take place. The behavior of $\mathrm{Im}[\Sigma_{n\mathbf{k}}(T)]$ can be understood with the following argument. Let's consider low temperatures and electrons with $\varepsilon_{n\mathbf{k}} \geq 0$. In this case both $f(\varepsilon_{n\mathbf{k}}, T)$ and $N(\omega_{\mathbf{q}\lambda}, T)$ are vanishingly small, and thus only the second term of the Eq. ((2.87)) contributes. For this reason, excited electrons relax via emission of phonons. But as

temperature increases, we get $0 \leq f(\varepsilon_{n\mathbf{k}}, T) \leq 1$ and $N(\omega_{\mathbf{q}\lambda}, T) > 0$, and both terms in Eq. (2.88) start contributing. An analogous argumentation can be carried out for holes. The EP scattering time is computed from inverse of the $\mathrm{Im}[\Sigma_{n\mathbf{k}}(T)]$ as

$$\tau_{n\mathbf{k}}(T) = \frac{\hbar}{2\mathrm{Im}[\Sigma_{n\mathbf{k}}(T)]}. \tag{2.89}$$

2.4 Time-evolution of excited charge carriers

Boltzmann transport equation is used to calculate the distribution of carriers $f(\mathbf{r}, \mathbf{p}, t)$ in phase space, which is in turn important to calculate the properties like mobility, velocities of the carriers and current density through the device. The change in the distribution function $f(\mathbf{r}, \mathbf{p}, t)$ through the phase space of volume $\mathbf{d^3rd^3p}$ in time dt can be simply written in the form

$$\frac{df}{dt} = -\mathbf{v} \cdot \nabla_r f - \mathbf{F} \cdot \nabla_p f + s(\mathbf{r}, \mathbf{p}, t) + \left.\frac{\partial f}{\partial t}\right|_{coll} \tag{2.90}$$

where $\mathbf{v}$ is the velocity of the particles, $\mathbf{F}$ is the force exerted by external field, $s(\mathbf{r}, \mathbf{p}, t)$ is the generation-recombination through defects and the $\left.\frac{\partial f}{\partial t}\right|_{coll}$ incorporate the collisions encountered by the carriers. We simplify Eq. (2.90) by assuming that the number of particles in the system is conserved, the system is subjected to no external field and is defect free. These assumptions make first three terms on the right side of Eq. (2.90) vanish and we are left with only collision term. We use Boltzmann transport equation in the context of materials where each carrier is designated by the band index n and wave vector $\mathbf{k}$. We change our notation of distribution function from $f(\mathbf{r}, \mathbf{p}, t)$ to $f_{n\mathbf{k}}(t, T)$. T comes into the argument of distribution function because the most common choice of the distribution function is Fermi-Dirac or Maxwellian distribution function, both of them are temperature dependent. The collision term is defined as

$$\frac{df_{n\mathbf{k}}(t,T)}{dt} = \left.\frac{\partial f_{n\mathbf{k}}}{\partial t}\right|_{coll} = -\frac{f_{n\mathbf{k}}(t,T) - f^{\mathrm{th}}_{n\mathbf{k}}(T)}{\tau_{n\mathbf{k}}(T)} \tag{2.91}$$

with the solution

$$f_{n\mathbf{k}}(t,T) = f^{\mathrm{th}}_{n\mathbf{k}}(T) + e^{-\frac{t}{\tau_{n\mathbf{k}}(T)}}[f_{n\mathbf{k}}(0,T) - f^{\mathrm{th}}_{n\mathbf{k}}(T)]. \tag{2.92}$$

Eq. (2.91) is commonly called RTA and Eq. (2.91) is the solution of RTA. It states that the distribution $f_{n\mathbf{k}}$ relaxes directly to the thermalized distribution $f^{th}_{n\mathbf{k}}$ with scattering rate $\tau^{-1}_{n\mathbf{k}}$. It omits all the intermediate relaxation steps between the initial non-equilibrium distribution and final relaxed distribution. We use Fermi-Dirac distribution with or without displaced Fermi energy depending upon the system under study as $f^{th}_{n\mathbf{k}}$. In other words, Eq. (2.92) states that the perturbation decays exponentially with the scattering time $\tau_{n\mathbf{k}}$ to restore the equilibrium Fermi-Dirac distribution $f(\varepsilon_{n\mathbf{k}}, T)$ [72]. Since, we consider EP scattering processes only, which is dominant for low carrier densities. We restrict ourselves to weak perturbation limit and neglect the higher order perturbations. We consider here the isotropic scattering processes only, i.e. there is no angular dependence and $\tau_{n\mathbf{k}}$ is the average time between the collision events defined through Eq. (2.89).

We generate the initial hot carrier occupation $f_{n\mathbf{k}}(0, T)$ as a combination of a Fermi-Dirac distribution $f(\varepsilon_{n\mathbf{k}}, T)$ at the temperature T and a Gaussian peak centered at energy $+\zeta$ for electrons in the conduction band ($\varepsilon_{n\mathbf{k}} > \varepsilon_{\mathrm{F}}$) and $-\zeta$ for the holes in the valence band ($\varepsilon_{n\mathbf{k}} < \varepsilon_{\mathrm{F}}$) as

$$\begin{aligned} f_{n\mathbf{k}}(0,T) &= f(\varepsilon_{n\mathbf{k}}, T) - \frac{\tilde{\lambda}_{\mathrm{h}}}{\sqrt{2\pi\sigma^2}} e^{\frac{(\varepsilon_{n\mathbf{k}}+\zeta)^2}{2\sigma^2}}, \quad \varepsilon_{n\mathbf{k}} < \varepsilon_{\mathrm{F}}, \\ f_{n\mathbf{k}}(0,T) &= f(\varepsilon_{n\mathbf{k}}, T) + \frac{\tilde{\lambda}_{\mathrm{e}}}{\sqrt{2\pi\sigma^2}} e^{\frac{(\varepsilon_{n\mathbf{k}}-\zeta)^2}{2\sigma^2}}, \quad \varepsilon_{n\mathbf{k}} \geq \varepsilon_{\mathrm{F}}. \end{aligned} \tag{2.93}$$

where, σ is a small smearing and ζ is the excitation energy counted from the valence and conduction band edges for holes and electrons respectively. $\tilde{\lambda}_{e/h}$ is the parameters to control the number of initially excited hot carriers and mostly chosen such that the same number of electrons and holes are excited

initially. σ and $\tilde{\lambda}_{e/h}$ are system dependent parameters and will be defined for each system specifically later.

We define the thermalization time τ_{th} as

$$\frac{P(\zeta, \tau_{\mathrm{th}}, T)}{P(\zeta, 0, T)} = \frac{1}{e} \tag{2.94}$$

with the population

$$P(E, t, T) = \sum_{n\mathbf{k}} \delta(E - \varepsilon_{n\mathbf{k}}) \times \begin{cases} [1 - f_{n\mathbf{k}}(t, T)], & E < \varepsilon_{\mathrm{F}}, \\ f_{n\mathbf{k}}(t, T), & E \geq \varepsilon_{\mathrm{F}}. \end{cases} \tag{2.95}$$

In our numerical calculations, we approximate the delta function in Eq. (2.95) by a narrow Gaussian with a width of approximately 20 meV. We focus on excitations above the quasi-Fermi levels, so that the finite width does not affect τ_{th}.

It must be noted that in our formalism the EP couplings are assumed to be small enough such that electronic wavefunctions, eigenenergies, and dynamical matrices are basically unchanged as compared to ground state calculations. Also, anharmonic interatomic interactions, which lead to hot phonon effect are disregarded for simplicity [70, 73]. We assume electron and phonon baths to be at the same temperature T.Our results are valid as long as the phonon thermalization times are much longer and phonon oscillation times are much shorter than the carrier thermalization times and the excited system is not far away from the equilibrium. The novelty of our model lies in the fact, that EP scattering times $\tau_{n\mathbf{k}}$ which is a central quantity are determined without any fitting parameters. It is precisely calculated taking into account the inter-and intraband transition arising from all the phonon branches. Our $\tau_{n\mathbf{k}}$ is band (n) and wave vector ($\mathbf{k}$) dependent that provides the microscopic details of the scattering events taking place in the BZ which is otherwise difficult to get from experiments.

Chapter 3

Photocarrier thermalization bottleneck in graphene

In this chapter, we present our *ab-initio* results on photocarrier thermalization bottleneck in defect free and intrinsic graphene. We use the methods described in Ch. 2 to calculate ground state properties of graphene and hence the self-energy. Later, temperature and excitation energy dependent thermalization time of hot carriers is extracted using Boltzmann equations. Our approach extracts the leading mechanism responsible for the suppression of the photocarrier thermalization at low excitation energies and temperatures, complimented by an explicitly solvable model.

From this work, we came up with one publication and this chapter is mainly from the Ref. [74]. We start this chapter by discussing the motivation for choosing graphene for our studies in Sec. 3.1. Then we present the details of simulations parameters used in the calculations and analytical model in Sec.3.2. Sec. 3.3 includes discussion on the self-energy of hot carriers and comparison of thermalization times between analytical model and our *ab-initio* approach. We finally conclude our main findings of this work in Sec. 3.4. Most of the sections of this chapter are from our own work Ref. [74].

3.1 Introduction

The central phenomenon employed in photodetection and PV is the conversion of light energy into electricity. It is a quantum conversion process, employing absorption of photons to deliver photoexcited carriers to an external circuit, where they do electrical work [75]. There are two obvious strategies for increasing the amount of energy transferred by photocarriers. One can try to speed up the photocarrier extraction such that the carriers are collected, while they are still hot or even out of thermal equilibrium. Alternatively, one can try to slow down the cooling or photocarrier thermalization for the same purpose. Graphene in a combination with other 2D semiconductors offers an interesting opportunity to employ both strategies. Thanks to the extremely small thickness of the junctions between 2D materials (also known as van der Waals (vdW) heterostructures [76]), interlayer photocarrier transport may occur faster than the intralayer relaxation processes [77]. At the same time the optical phonon emission is strongly suppressed for low-energy excitations in graphene due to unusually high energy quanta of optical phonons [78, 79]. As a consequence, the photocarriers can be extracted well before they thermalize and dissipate useful energy by means of phonon emission. By incorporating graphene into a heterostructure, we can combine the two strategies in one optoelectronic device. In this way the photoresponse can be substantially increased simultaneously to the device performance. In this work, we focus on the photocarrier evolution in intrinsic graphene, providing conclusive evidence for the existence of a thermalization bottleneck that makes such applications possible.

The striking difference between electron thermalization in intrinsic graphene and in a metal (e.g. doped graphene) is that the electron-electron collision rate is much lower in the former than in the latter, as it has been pointed out and confirmed by means of Raman spectroscopy by Basko et al. [80]. Indeed two electrons colliding with each other have to satisfy energy and momentum conservation. If one electron is excited in the conduction band, then it most likely collides with another electron from the valence band, as the conduction band is almost empty in intrinsic graphene. The only possible way to satisfy both conservation laws in this case is to assume all four involved momenta to be parallel (collinear scattering). This is a direct consequence of the cone-like dispersion for carriers in graphene. Collinear scattering is an inefficient thermalization mechanism, and the corresponding electron-electron thermalization time is about 1 ps for photocarriers excited in the optical spectral region, and it is even longer for lower excitation energies [78, 79, 81]. Since our model is developed to provide a solid proof for the photocarrier thermalization bottleneck in intrinsic graphene that occurs at the excitation energy near 100 meV, the electron-electron scattering turns out to be irrelevant for such excitation energies and only EP scattering is taken into account. This assumption is invalid for conventional heavily doped graphene samples with a Fermi energy of about 200 meV. However, such samples would not be suitable for studying the photocarrier thermalization bottleneck, as the relevant interband excitations are blocked by the Pauli principle.

In contrast to advanced two-temperature models for electron thermalization in metals [82–84] and semiconductors [85] we are dealing here with a single temperature describing both the thermalized electrons and equilibrium phonons. This single-temperature model does not treat the thermalization of phonons, which would require to take into account additional effects such as phonon- phonon scattering due to anharmonicities [70]. Neglecting weak perturbations from nonequilibrium phonon occupations, the photoexcited electrons in our model relax directly to the Fermi-Dirac distribution that is already in thermal equilibrium with the phonon bath. The temperature can be much higher than 300 K due to sample heating, but we assume the absorbed radiation fluence to be low enough to prevent a further increase of this temperature.

The photocarrier dynamics in graphene has been studied experimentally by means of pump-probe spectroscopy as well as time- and angle-resolved photoemission spectroscopy [86–94]. In the experiments the carriers are excited far above the Dirac point (by more than 1 eV), and the ultrafast relaxation of hot carriers is mainly attributed to optical phonon emission and electron-electron scattering, taking place within 150-170 fs [86, 91]. Excitations below the highest optical phonon energy (of around 200 meV in graphene) have been studied in Refs. [78, 79, 95], where it has been observed that the relaxation time is drastically increased from the femtosecond to the picosecond timescale. There has been a number of theoretical attempts to understand the thermalization and cooling in graphene [51–55, 78, 96–101], but most of the models suffer from drawbacks by neglecting the acoustical phonons or the contribution from other points in the BZ. EP coupling in n-doped graphene have been studied using *ab-initio* methods but not for the intrinsic graphene [102]. Further Raman spectroscopy has revealed the complex nature of the phonon dynamics in the presence of hot carriers [103, 104].

In detail, we present an *ab-initio* method to calculate the band and momentum resolved scattering times $\tau_{n\mathbf{k}}(T)$ along with their temperature dependence. We use $\tau_{n\mathbf{k}}(T)$ in the Boltzmann equation under the RTA to calculate the thermalization time τ_{th}. We investigate the relaxation time for different excitation energies from 0.05 to 0.8 eV and over a wide range of temperatures from 0 to 2000 K taking advantage of the high melting point of graphene [105].

3.2 Theory

3.2.1 *Ab-initio* modelling parameters

The ground state properties of graphene are calculated using DFT as implemented in QUANTUMESPRESSO [63] within the LDA. The contribution of the core electrons is taken into account through Troullier-Martins pseudopotential [106] and $2s^2 2p^2$ are used for the valence configuration. We employ a plane-wave (PW) basis set with a kinetic energy cutoff of 110 Ry and a charge density cutoff of 440 Ry. To simulate the graphene, the unit cell is repeated in xy-plane and interaction with the periodic images along z-direction is eliminated by using a vacuum of 20 Å along z-direction. The unit cell and the atoms in the unit cell of graphene are relaxed with the help of the Broyden-Fletcher-Goldfarb-Shanno algorithm using very strict force and total energy cutoffs. The cell and atoms are relaxed until the net force on atoms is less than 10^{-6} Ry/a.u., and total energy changes are below 10^{-8} Ry. The ground state charge density is calculated using $45 \times 45 \times 1$ Γ-centered $\mathbf{k}$-grid in the first BZ. We obtain an optimized in-plane lattice constant of graphene of $a = |\mathbf{a}_1| = |\mathbf{a}_2| = 2.436$ Å, see Fig. 3.1(a), which is in good agreement with previous reports of 2.458 Å [107]. The electronic wavefunctions and eigenenergies are calculated on $36 \times 36 \times 1$ $\mathbf{k}$-grid, whereas phonon dynamical matrices and frequencies are calculated on a $12 \times 12 \times 1$ $\mathbf{q}$-grid using DFPT [108] along high symmetry lines of the first BZ, as shown in Fig. 3.1(b). Fig. 3.1(c) shows the electronic band structure, as computed from DFT with PW. The excellent agreement with those determined through the WF method demonstrates the high quality of the interpolated localized orbitals. The phonon dispersion is finally displayed in Fig. 3.1(d). LO and TO phonon modes of graphene at the Γ-point are degenerate at an energy of 198.37 meV, which matches well with a previously reported value of 197.75 meV [107].

Having determined electronic and phononic band structures, we calculate the electronic self-energy $\Sigma_{n\mathbf{k}}(T)$ due to the EP interaction for the electronic eigenstate $|n\mathbf{k}\rangle$ with the EPW code Eq. (2.87) [73]. We construct WFs to get localized orbitals from PW eigenfunctions. By interpolating WFs, we finally obtain electronic eigenenergies, dynamical matrices and EP couplings on fine grids in the BZ [109]. We use a $1200 \times 1200 \times 1$ $\mathbf{k}$-grid and a $300 \times 300 \times 1$ $\mathbf{q}$-grid, which we find necessary to accurately map out the whole BZ and to converge the integral over $\mathbf{q}$ in Eq. (2.87).

The EP scattering time is used to study the time evolution of hot carriers using Boltzmann equations within RTA. For the initial occupation we use Eq. 2.93, with a small energy broadening $\sigma = 8.47$ meV. The free parameter $\tilde{\lambda}_{e/h}$ is adopted to adjust the initial occupation and is adjusted in such a way that initially the same number of electrons and holes are excited in conduction and valence bands respectively. The value which we use for the free parameter $\tilde{\lambda}_e = \tilde{\lambda}_h = 2.4 \times 10^{-3}$ eV. Since we are interested in the excitation range of -0.8 eV $\leq \zeta \leq 0.8$ eV, the electronic density of states (DOS) is rather symmetric in this range and $\tilde{\lambda} = \tilde{\lambda}_\mathrm{e} = \tilde{\lambda}_\mathrm{h}$ turns out to be an excellent approximation. It can be related to measurements through $\tilde{\lambda} = 4\pi^2 \alpha \hbar^2 \Phi v_\mathrm{F}^2 / \zeta^2$. In the expression, $\pi\alpha$ is the linear absorption of graphene, Φ is the pump-fluence and v_F is the Fermi velocity of electrons in graphene [81]. Then the occupations are time stepped up using Eq. (2.92) which is the solution of the Boltzmann equation 2.91. Finally, the time evolution of the photoexcited carriers is determined using Eq. (2.95). The delta function in the Eq. (2.95) is approximated by a narrow Gaussian of width 15 meV.

3.2.2 Analytical model

Before performing parameter-free *ab-initio* calculations of charge carrier dynamics, we estimate the photocarrier thermalization time of intrinsic graphene within an explicitly solvable model. For simplicity we assume only optical phonon modes p that are dispersionless, i.e., exhibit the fixed energy $\hbar\omega_p$. For this reason phonon wave vectors will be omitted. Furthermore, we consider only the two linear electronic bands of the Dirac cone with $\varepsilon_{n\mathbf{k}} = n\hbar v_\mathrm{F} k$, $n = \pm$ and $k = |\mathbf{k}|$. Additionally, we will

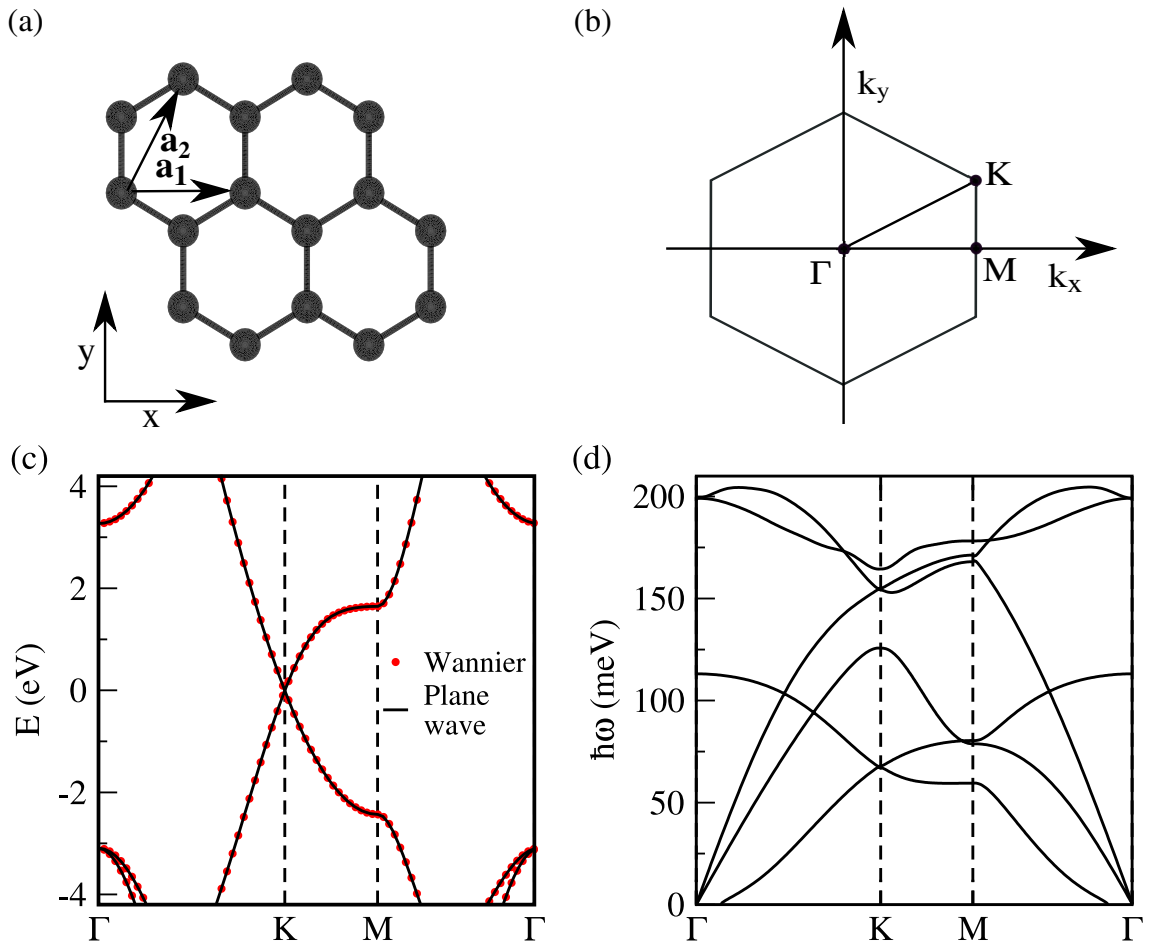

Figure 3.1: (a) Lattice structure of graphene with in-plane lattice vectors $\mathbf{a}_1$ and $\mathbf{a}_2$. (b) Reciprocal lattice of graphene with high symmetry points in the first BZ. (c) Electronic band structure of graphene, as obtained directly from the calculations with the PW basis set and the corresponding curve from the WF formalism. (d) Phonon band structure of graphene.

suppress all time and temperature arguments of the occupation functions in this subsection, because we assume a steady state regime.

The EP collisions in the given optical phonon mode p are governed by the following integral

$$I_p[\tilde{f}_{n\mathbf{k}}] = \sum_{n'\mathbf{k}'} \left[\tilde{f}_{n'\mathbf{k}'} \left(1 - \tilde{f}_{n\mathbf{k}}\right) W_{n'\mathbf{k}'\to n\mathbf{k}} \; - \tilde{f}_{n\mathbf{k}} \left(1 - \tilde{f}_{n'\mathbf{k}'}\right) W_{n\mathbf{k}\to n'\mathbf{k}'} \right],$$

where $\tilde{f}_{n\mathbf{k}} = f^{(0)}_{\varepsilon_{n\mathbf{k}}} + \tilde{f}^{(1)}_{n\mathbf{k}}$ denotes the carrier occupation with the time-independent Fermi-Dirac distribution $f(\varepsilon_{n\mathbf{k}}, T) = f^{(0)}_{\varepsilon_{n\mathbf{k}}}$ and the non-equilibrium addition $\tilde{f}^{(1)}_{n\mathbf{k}}$, representing the second term in Eq. (2.92). The transition probability is given by Fermi's golden rule

$$W_{n\mathbf{k}\to n'\mathbf{k}'} = \frac{2\pi}{\hbar} W_p \left[(N_p + 1)\, \delta\left(\varepsilon_{n\mathbf{k}} - \varepsilon_{n'\mathbf{k}'} - \hbar\omega_p\right) + N_p \delta\left(\varepsilon_{n\mathbf{k}} - \varepsilon_{n'\mathbf{k}'} + \hbar\omega_p\right) \right] \tag{3.1}$$

for carriers outgoing from the state $|n\mathbf{k}\rangle$, and

$$W_{n'\mathbf{k}'\to n\mathbf{k}} = \frac{2\pi}{\hbar} W_p \left[(N_p + 1)\, \delta\left(\varepsilon_{n'\mathbf{k}'} - \varepsilon_{n\mathbf{k}} - \hbar\omega_p\right) + N_p \delta\left(\varepsilon_{n'\mathbf{k}'} - \varepsilon_{n\mathbf{k}} + \hbar\omega_p\right) \right] \tag{3.2}$$

for carriers incoming to the state $|n\mathbf{k}\rangle$. Making use of nearly dispersionless optical phonon modes, the EP interaction matrix element W_p is assumed to be independent of momentum. The first term in both Eqs. (3.1) and (3.2) corresponds to the phonon emission, while the second one describes the phonon absorption. The phonons are treated as a non-interacting gas, characterized by the Bose-Einstein distribution $N_p = N(\hbar\omega_p, T)$. Due to the strong carbon-carbon bonding in graphene the optical phonon energy is higher than 100 meV [see Fig. 3.1(c)] and, hence, we assume $\hbar\omega_p \gg k_\mathrm{B}T$ for typical temperatures or, in other words, $N_p \ll 1$. The collision integral can then be simplified to

$$I_p[\tilde{f}_{n\mathbf{k}}] = \frac{2\pi}{\hbar} W_p \sum_{n'\mathbf{k}'} \Big[\tilde{f}_{n'\mathbf{k}'} \left(1 - \tilde{f}_{n\mathbf{k}}\right) \delta\left(\varepsilon_{n'\mathbf{k}'} - \varepsilon_{n\mathbf{k}} - \hbar\omega_p\right) - \tilde{f}_{n\mathbf{k}} \left(1 - \tilde{f}_{n'\mathbf{k}'}\right) \times \delta\left(\varepsilon_{n\mathbf{k}} - \varepsilon_{n'\mathbf{k}'} - \hbar\omega_p\right) \Big]. \tag{3.3}$$

Let us now assume $\tilde{f}_{n\mathbf{k}}$ to be a function of $\varepsilon_{n\mathbf{k}}$ and integrate in momentum space. Making use of the δ-function and $\varepsilon_{nk} = \varepsilon_{n\mathbf{k}}$, we obtain

$$I_p[\tilde{f}_{\varepsilon_{nk}}] = \frac{W_p}{\hbar^3 v_\mathrm{F}^2} \left[|\varepsilon_{nk} + \hbar\omega_p| \tilde{f}_{\varepsilon_{nk}+\hbar\omega_p} \left(1 - \tilde{f}_{\varepsilon_{nk}}\right) - |\varepsilon_{nk} - \hbar\omega_p| \tilde{f}_{\varepsilon_{nk}} \left(1 - \tilde{f}_{\varepsilon_{nk}-\hbar\omega_p}\right) \right]. \tag{3.4}$$

Finally, we employ a linear response approximation and the property of intrinsic graphene $1 - f^{(0)}_{\varepsilon_{nk}} = f^{(0)}_{-\varepsilon_{nk}}$ so that

$$\tilde{f}_{\varepsilon_{nk}+\hbar\omega_p} \left(1 - \tilde{f}_{\varepsilon_{nk}}\right) \approx f^{(0)}_{\varepsilon_{nk}+\hbar\omega_p} f^{(0)}_{-\varepsilon_{nk}} - \tilde{f}^{(1)}_{\varepsilon_{nk}} f^{(0)}_{\varepsilon_{nk}+\hbar\omega_p} + \tilde{f}^{(1)}_{\varepsilon_{nk}+\hbar\omega_p} f^{(0)}_{-\varepsilon_{nk}}, \tag{3.5}$$

$$\tilde{f}_{\varepsilon_{nk}} \left(1 - \tilde{f}_{\varepsilon_{nk}-\hbar\omega_p}\right) \approx f^{(0)}_{-\varepsilon_{nk}+\hbar\omega_p} f^{(0)}_{\varepsilon_{nk}} + \tilde{f}^{(1)}_{\varepsilon_{nk}} f^{(0)}_{-\varepsilon_{nk}+\hbar\omega_p} - \tilde{f}^{(1)}_{\varepsilon_{nk}-\hbar\omega_p} f^{(0)}_{\varepsilon_{nk}}. \tag{3.6}$$

Hence, Eq. (3.4) can be written as a sum of two terms $I_p[\tilde{f}_{\varepsilon_{nk}}] = I_p[f^{(0)}_{\varepsilon_{nk}}] + \hat{I}_p[f^{(0)}_{\varepsilon_{nk}}, \tilde{f}^{(1)}_{\varepsilon_{nk}}]$, where

$$I_p[f^{(0)}_{\varepsilon_{nk}}] = \frac{W_p}{\hbar^3 v_\mathrm{F}^2} \left[|\varepsilon_{nk} + \hbar\omega_p| f^{(0)}_{\varepsilon_{nk}+\hbar\omega_p} f^{(0)}_{-\varepsilon_{nk}} - |\varepsilon_{nk} - \hbar\omega_p| f^{(0)}_{-\varepsilon_{nk}+\hbar\omega_p} f^{(0)}_{\varepsilon_{nk}} \right], \tag{3.7}$$

$$\hat{I}_p[f^{(0)}_{\varepsilon_{nk}}, \tilde{f}^{(1)}_{\varepsilon_{nk}}] = \frac{W_p}{\hbar^3 v_\mathrm{F}^2} \Big[|\varepsilon_{nk} + \hbar\omega_p| \left(\tilde{f}^{(1)}_{\varepsilon_{nk}+\hbar\omega_p} f^{(0)}_{-\varepsilon_{nk}} - \tilde{f}^{(1)}_{\varepsilon_{nk}} f^{(0)}_{\varepsilon_{nk}+\hbar\omega_p} \right) - |\varepsilon_{nk} - \hbar\omega_p| \left(\tilde{f}^{(1)}_{\varepsilon_{nk}} f^{(0)}_{-\varepsilon_{nk}+\hbar\omega_p} - \tilde{f}^{(1)}_{\varepsilon_{nk}-\hbar\omega_p} f^{(0)}_{\varepsilon_{nk}} \right) \Big]. \tag{3.8}$$

Eqs. (3.7) and (3.8) are valid for any ratio between ε_{nk} and $\hbar\omega_p$ so that we can investigate the thermalization behavior for photocarriers excited below and above the phonon frequency. Note that only Eq. (3.8) is responsible for thermalization, because Eq. (3.7) does not contain $\tilde{f}^{(1)}_{\varepsilon_{nk}}$.

In what follows we consider the thermalization of electrons (i.e., $\varepsilon_k = \varepsilon_{+k} = \hbar v_\mathrm{F} k$), as the thermalization of holes is equivalent in the case of intrinsic graphene at not too high excitation energies [see Fig. 3.1(c)]. Assuming the initial non-equilibrium distribution to be δ-shaped, $f^{(1)}_{\varepsilon_k} \propto \delta\left(\varepsilon_k - \hbar\omega/2\right)$, we find

$$I_p[\tilde{f}_{\varepsilon_k}] = \frac{\omega W_p}{2\hbar^2 v_\mathrm{F}^2} \left(\tilde{f}^{(1)}_{\varepsilon_k+\hbar\omega_p} f^{(0)}_{-\frac{\hbar\omega}{2}+\hbar\omega_p} + \tilde{f}^{(1)}_{\varepsilon_k-\hbar\omega_p} f^{(0)}_{\frac{\hbar\omega}{2}+\hbar\omega_p} \right) - \frac{W_p}{\hbar^2 v_\mathrm{F}^2} \tilde{f}^{(1)}_{\varepsilon_k} \left(\left|\frac{\omega}{2} + \omega_p\right| f^{(0)}_{\frac{\hbar\omega}{2}+\hbar\omega_p} + \left|\frac{\omega}{2} - \omega_p\right| f^{(0)}_{-\frac{\hbar\omega}{2}+\hbar\omega_p} \right). \tag{3.9}$$

Eq. (3.9) contains cascade terms, generated each time, when a phonon is emitted or absorbed [100]. We use the RTA, i.e., we truncate the cascade to a single term proportional to $\tilde{f}^{(1)}_{\varepsilon}$. This results in the

thermalization time given by

$$\frac{1}{\tau_{\mathrm{th}}} = \sum_p \frac{W_p}{\hbar^2 v_{\mathrm{F}}^2} \left(\left| \frac{\omega}{2} + \omega_p \right| f^{(0)}_{\frac{\hbar\omega}{2}+\hbar\omega_p} + \left| \frac{\omega}{2} - \omega_p \right| f^{(0)}_{-\frac{\hbar\omega}{2}+\hbar\omega_p} \right). \tag{3.10}$$

This analytical model is of course not able to give quantitative predictions, but it suggests that the thermalization time at $\omega_p \gg \omega/2$ is much longer than at $\omega_p \ll \omega/2$. Indeed, in the latter limit we have

$$\frac{1}{\tau_{\mathrm{th}}} = \sum_p \frac{\omega W_p}{2\hbar^2 v_{\mathrm{F}}^2}, \quad \omega_p \ll \omega/2, \tag{3.11}$$

whereas in the former case the rate contains an exponentially small multiplier, resulting in the following expression

$$\frac{1}{\tau_{\mathrm{th}}} = \sum_p \frac{2\omega_p W_p}{\hbar^2 v_{\mathrm{F}}^2} \mathrm{e}^{-\frac{\hbar\omega_p}{k_{\mathrm{B}}T}}, \quad \omega_p \gg \omega/2. \tag{3.12}$$

We will confirm the predictions of Eqs. (3.11) and (3.12) in the next section using the *ab-initio* approach. Note, however, that while the approximation $\hbar\omega_p \gg k_{\mathrm{B}}T$ or $N_p \ll 1$, made for their derivation, is excellent for most temperatures studied, we will consider temperatures of up to 2000 K with our *ab-initio* approach, where this approximation becomes questionable.

3.3 Results

We will now use the *ab-initio* parameters for electrons, phonons and their couplings, as described in Sec. 2.1, 2.2, 2.3, and combine them with the Boltzmann formalism of Sec. 2.4 of Ch. 2 to study photocarrier thermalization. At the end, we will compare to the results of the analytical equations as derived in Sec. 3.2.2.

Since we determine scattering times $\tau_{n\mathbf{k}}$ of the Boltzmann formalism [see Eq. (2.91)] from the imaginary part of the EP self-energy [see Eq. (2.87)], we investigate this quantity first. Fig. 3.2(a) plots $\mathrm{Im}[\Sigma_{n\mathbf{k}}(T)]$ as a function of energy for different temperatures. For a given temperature it shows a pronounced energy dependence. Increasing initially monotonically and rather symmetrically in the vicinity of the Dirac point at $E = \varepsilon_{\mathrm{F}} = 0$, it follows the same behavior as the electronic DOS [see Eqs. (2.87)]. This results from the fact that the electronic DOS represents the phase space for EP scattering events to take place. As can be inferred from Fig. 3.2(a) and 3.2(b), $\mathrm{Im}[\Sigma_{n\mathbf{k}}(T)]$ is very sensitive to temperature close to $E = 0$. In contrast it shows a much weaker temperature dependence at energies above around 200 meV, coinciding with the highest optical phonon energies. Indeed, we see for low temperatures (0-300 K) that $\mathrm{Im}(\Sigma_{n\mathbf{k}})$ increases roughly exponentially until the highest optical phonon energy is reached, while the energy dependence is comparatively weak for elevated temperatures (600-2000 K). The behavior shows that scattering below the optical phonon threshold takes place rather inefficiently via acoustical phonons. With increasing temperature there are more phonons available for the carriers to interact with, leading to the increase of $\mathrm{Im}[\Sigma_{n\mathbf{k}}(T)]$. Analogously, the available phase space for optical phonon emission grows with increasing energy. We compare our EP matrix elements with the one used in literature [55, 110] and find them in excellent agreement.

EP matrix element	Our work	Ref. [55, 110]
$\lvert g_\Gamma \rvert^2$	0.0408	0.0405
$\lvert g_K \rvert^2$	0.1004	0.0994

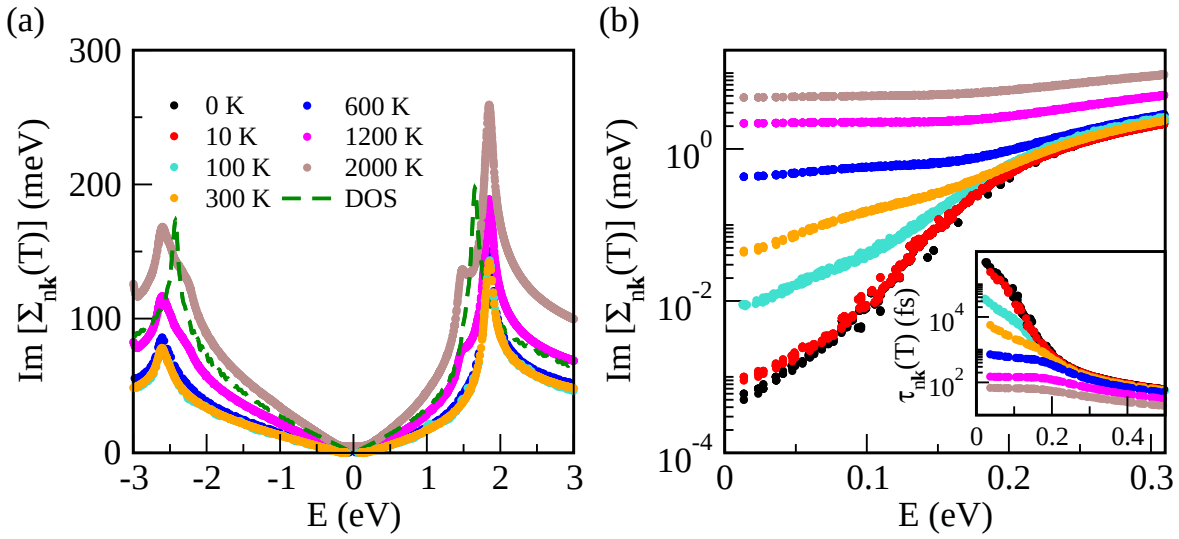

Figure 3.2: (a) Imaginary part of the EP self-energy as a function of energy, evaluated at different temperatures, and the electronic DOS of graphene. (b) Zoom in on the energy and temperature dependence of $\mathrm{Im}[\Sigma_{n\mathbf{k}}(T)]$. We consider only positive energies close to the Dirac point. The inset represents the corresponding scattering times.

Here, g_Γ denotes $g^{mn}_\lambda(\mathbf{k},\mathbf{q})$ with $\mathbf{k} = K$ and $\mathbf{q} = \Gamma$. Whereas, g_K denotes $g^{mn}_\lambda(\mathbf{k},\mathbf{q})$ with $\mathbf{k} = \mathbf{q} = K$ and m, n are the valence and conduction band crossing at Dirac-point. g_Γ and g_K is averaged over λ = LO, TO phonon modes. In the inset of Fig. 3.2(b), we consider the scattering times $\tau_{n\mathbf{k}}(T)$, which are inversely proportional to the self-energy [see Eq. (2.89)]. We observe that around the Dirac point the scattering time becomes very sensitive to temperature and can be on the order of a few picoseconds for low T. In contrast, at energies above 200 meV the scattering times exhibit only weak energy and temperature dependencies. As argued before, this behavior can be rationalized by the fact that for low T at $E < 200$ meV excited carriers can relax via acoustical phonon scattering only, while they thermalize efficiently via optical phonons above 200 meV.

To simulate the temporal dynamics, we use Eq. (2.92), starting with the initial distribution of Eq. (2.93) at time $t = 0$. Choosing the parameters $\tilde{\lambda}$ and σ as described in Sec. 3.2, we calculate time evolutions of occupations for different temperatures T and excitation energies ζ. We are particularly interested in the behavior of thermalization times for excitations below and above the optical phonon threshold. Fig. 3.3 shows the hot carrier population $P(E,t,T)$ [see Eq. (2.95)] for excitation energies $\zeta = 0.05, 0.5$ eV and temperatures $T = 0, 10, 100$ K. Below the optical phonon threshold for $\zeta = 0.05$ eV in Fig. 3.3(a)-(c), thermalization of the hot carriers takes place on the ps timescale via low-energy acoustical phonons. In this excitation range the relaxation time decreases with increasing temperature, because the background equilibrium electron distribution allows excited carriers to scatter increasingly efficiently with the optical phonons [95]. Our thermalization time τ_{th} at $T = 10$ K, as extracted from Fig. 3.3(b), is around 175 ps. This is lower than the 300 ps reported in Ref. [95] for an excitation energy of 51 meV on an epitaxially grown graphene sample containing around ~ 70 layers and arranged over a SiC substrate. Above the optical phonon threshold, our results in Fig. 3.3(d)-(f) predict a weak or almost no temperature dependence of the relaxation time. With $\tau_{\text{th}} \approx 60$ fs it takes a value of similar size as the photocarrier isotropization time from Ref. [94], originating from scattering by optical phonons. Our qualitative findings of a strong temperature dependence of τ_{th} below the optical phonon threshold and none above are consistent with the experimental observations in Ref. [95]. The plots in Fig. 3.3 also demonstrate that the populations of electrons and holes evolve with time

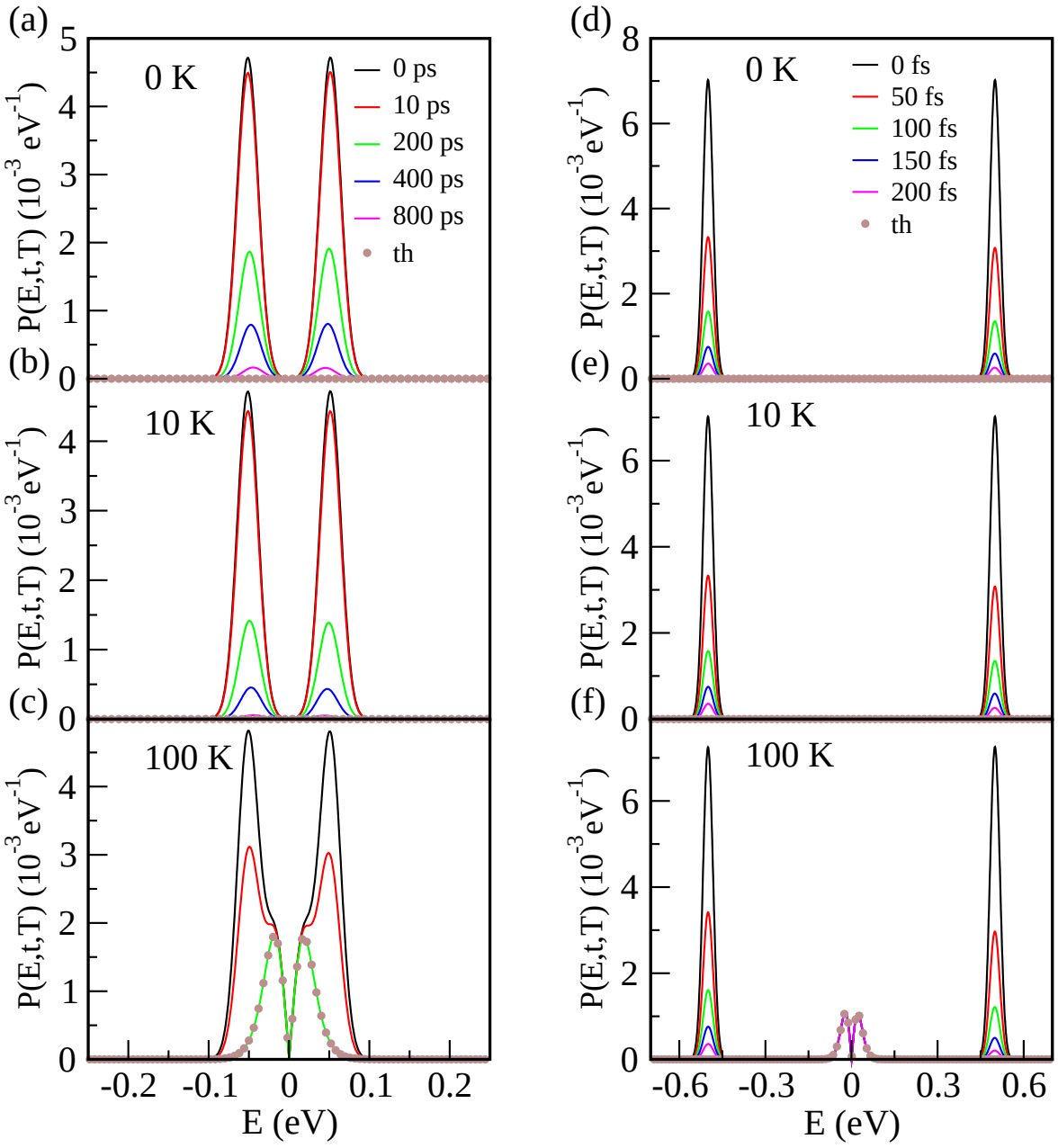

Figure 3.3: Time-dependent thermalization of photocarriers at an excitation energy of (a)-(c) 0.05 eV and (d)-(f) 0.5 eV for different temperatures.

quite symmetrically around the Dirac point, confirming that the dynamics of holes are similar as those of electrons.

Due to the extraordinarily high melting temperature of nearly 5000 K predicted theoretically for graphene [105], we extend our analysis of time evolutions to high temperatures $T = 300, 600, 1200$, 2000 K, see Fig. 3.4. As temperature in the system is increased, it is clear from Eq. (2.87) that the hot electrons (holes) cannot only emit (absorb) the phonons, but also absorb (emit) the phonons, which reduces thermalization times further. We find carriers to relax at $T = 300$ or 600 K on a 100 fs time scale. At 1200 K this reduces to around 34 fs and is even below 26 fs at 2000 K.

In Fig. 3.5 we summarize the relaxation times τ_{th}, which we have extracted from the Boltzmann

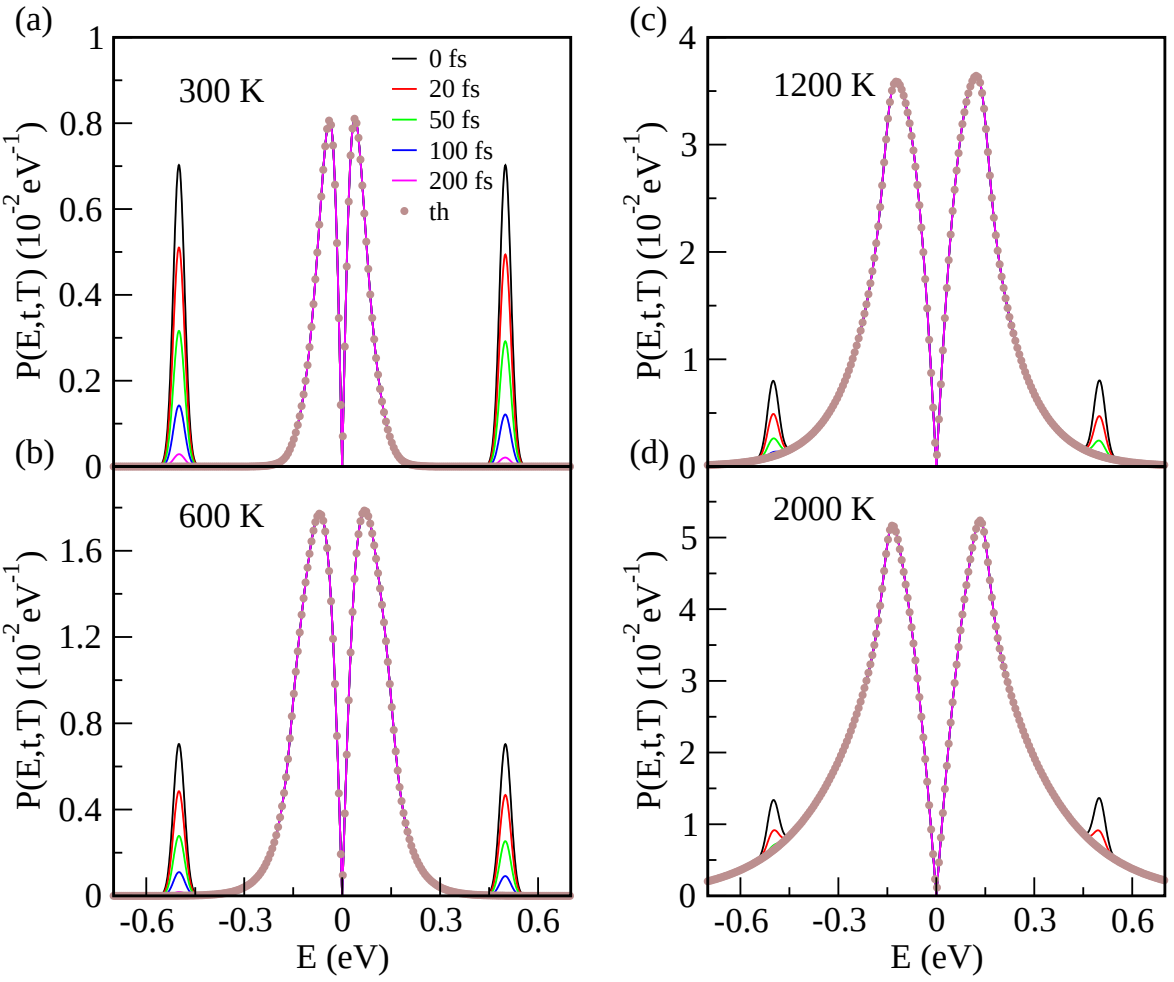

Figure 3.4: Same as Fig. 3.3 at an excitation energy of 0.5 eV for elevated temperatures.

equation combined with our *ab-initio* modeling at different excitation energies and temperatures. For $\zeta = 0.05$ eV the thermalization time decreases with increasing temperature from $T = 0$ to 1200 K by more than 3 orders of magnitude. In contrast, there is only little change in the relaxation time with temperature for a fixed excitation with $\zeta = 0.4, 0.6, 0.8$ eV above the optical phonon threshold. A slight decrease is seen at the temperatures, where thermal energies are similar to those of optical phonon quanta, i.e., $k_{\mathrm{B}}T \approx \hbar\omega_p$. In addition, for a fixed temperature, relaxation times depend only little on ζ, if the excitation energy is above the optical phonon threshold. To summarize, taking into account only EP scattering events, we thus observe intriguingly that relaxation times in graphene can span an extraordinary range from 170 ps down to 60 fs, if the temperature is varied and carriers are excited below the optical phonon threshold.

Our predictions can be qualitatively understood by using the concept of a thermalization bottleneck in graphene. Thanks to the high optical phonon energy quanta of about 200 meV [see Fig. 3.1(d)], the low-energy (THz) electrons cannot relax as fast as the optically excited photocarriers, because at low temperatures (i) the phonon absorption is a very rare process and (ii) the phonon emission requires an empty electron state below the Fermi level, but states below ε_{F} are almost fully occupied. The relevant thermalization times can be estimated by using our analytical model. We assume an explicit form for the EP interaction matrix element given by [99]

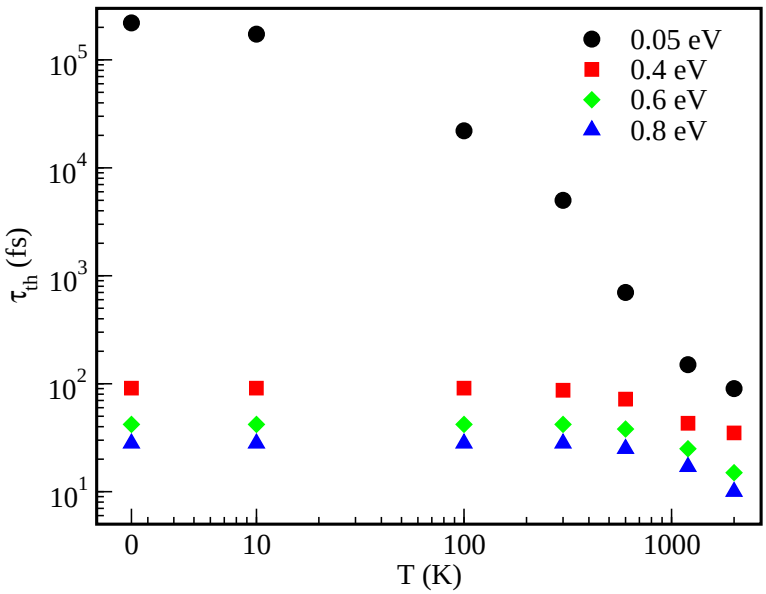

Figure 3.5: Thermalization time of the excited carriers, as determined from the Boltzmann equation, as a function of temperature for different excitation energies.

$$W_p = \frac{\hbar \Delta_p^2 F_p}{2\rho\omega_p}, \tag{3.13}$$

where Δ_p is the deformation potential for a mode p, F_p is a dimensionless geometric factor, and $\rho = 7.6 \times 10^{-8}$ g/cm^2 is the mass density. In what follows, we take into account the two most important phonon modes [99], $p = \Gamma, \mathrm{K}$, where $F_\Gamma = 1$, $F_\mathrm{K} = 1/2$, $\hbar\omega_\Gamma = 197$ meV, $\hbar\omega_\mathrm{K} = 157$ meV, and $\Delta_\Gamma = \Delta_0$, $\Delta_\mathrm{K} = \sqrt{2}\Delta_0$ with $\Delta_0 = 11$ eV/Å [99]. At $\omega \gg \omega_p$ the thermalization time can be found from Eq. (3.11) as

$$\tau_\mathrm{th} = \frac{4\omega_0}{\omega}\frac{\hbar v_\mathrm{F}^2 \rho}{\Delta_0^2}, \quad \omega \gg \omega_{\Gamma,\mathrm{K}}, \tag{3.14}$$

where $1/\omega_0 = 1/\omega_\Gamma + 1/\omega_\mathrm{K}$. Assuming an excitation energy of $\hbar\omega = 1.55$ eV (i.e., a radiation wavelength of 800 nm), we estimate $\tau_\mathrm{th} \approx 58$ fs. In the opposite limit $\omega \ll \omega_p$ we get from Eq. (3.12)

$$\tau_\mathrm{th} = \frac{\hbar v_\mathrm{F}^2 \rho}{\Delta_0^2}\frac{1}{\exp(-\frac{\hbar\omega_\Gamma}{k_\mathrm{B}T}) + \exp(-\frac{\hbar\omega_\mathrm{K}}{k_\mathrm{B}T})}, \quad \omega \ll \omega_{\Gamma,\mathrm{K}}. \tag{3.15}$$

Assuming the most relevant temperature of 300 K, we estimate $\tau_\mathrm{th} \approx 92$ ps.

Our considerations confirm that (i) the thermalization timescales differ at $\omega \ll \omega_p$ and $\omega \gg \omega_p$ by three orders of magnitude at room temperature, (ii) the photocarrier thermalization time strongly depends on temperature at $\omega \ll \omega_p$, whereas at $\omega \gg \omega_p$ it does not, (iii) in the former case, the thermalization time decreases rapidly with increasing temperature. This is exactly what we see in the summary of the relaxation times τ_th shown in Fig. 3.5, as determined through our first principles approach.

3.4 Summary and Outlook

In summary, we have studied the relaxation dynamics of hot carriers in single-layer graphene near and away from the Dirac point subject to the EP interaction. In excellent agreement with analytical predictions we find that relaxation times computed with our model are strongly increased, if carriers are excited below the optical phonon energies. In addition, we have shown that the carrier relaxation times depend strongly on temperature for such low excitation energies, while being rather temperature-independent for excitation energies above optical phonon energy quanta. Our results are in agreement with the experimental findings, attributing photocarrier relaxation at different excitation energies to different phonon branches [86, 91, 95].

DFT results depend on the choice of the exchange-correlation functional. To assess the robustness of DFT-derived electron and phonon dispersions as well as EP couplings, different functionals have been tested in Ref. [111] and compared to the Hartree-Fock and GW approximations. While the cone-like electron dispersion at the K-point is consistently reproduced and phonon dispersions are generally found to be in good agreement with experiment, inaccuracies of the EP couplings for the highest optical phonon branch near the K-point have been corroborated and the GW approach has been advocated as a way for making quantitative improvements. While the use of electronic structure methods beyond DFT would certainly be desirable in the future, we expect that more accurate *ab-initio* input parameters will not qualitatively change the results presented here.

The photocarrier thermalization bottleneck could be employed to facilitate the photoexcited electron transport from graphene to a semiconductor across a Schottky barrier [112–114]. Thanks to the longer relaxation time at lower excitation energies, the photocarriers can contribute to the interlayer transport before thermalization is completed, thus improving the photoresponsivity [115]. From the device engineering point of view, the most important assumption made in this work is the absence of a substrate. It might provide additional dielectric screening and unintentional doping, which overall influence the electron-electron scattering contribution neglected here. Moreover the photocarriers might experience interactions with remote polar surface phonons [99], providing additional EP scattering channels. Since the precise effects caused by a substrate strongly depend on the chosen material and its interface properties, the model should be tailored for each device to make quantitative predictions. Such aspects could be addressed in future work.

Chapter 4

Effect of spin-orbit coupling on thermalization of photoexcited carriers in two-dimensional transition metal dichalcogenides and internal quantum efficiency of van der Waals heterostructures

In this chapter, we focus on another class of 2D materials called TMDCs of type MX_2 with M being a transition metal and X is a chalcogen. As mentioned previously, strong light-matter interaction, selective valley excitations, and a direct bandgap make them an excellent candidate for electronics, optoelectronics and, PV devices. The systems of our interest here are single-layer of MoS_2 and WSe_2. The single-layer of WSe_2 shows approximately three times stronger SOC splitting at VBM than MoS_2. We investigate the effect SOC in the EP scattering events leading to the thermalization of photoexcited carriers. We show that self-energy decreases around the band edges where SOC splitting is not small. Due to the finite energy gap between optical and acoustical phonons in the phonon band structure, we can resolve the thermalization times in terms of optical and acoustical phonon contributions. We approximate tunneling time using an analytical model. The ratio between thermalization and tunneling times as a function of excitation energy shows almost no energy dependence for WSe_2 which is not true in case of MoS_2. The results reported in Sec.4.3 are available online Ref.[116] and is currently under review. This chapter up to large extent is from our own work Ref. [116].

We start with the motivation in Sec. 4.1.In Sec. 4.2, we refer to the computational details of the simulations and an analytical model used to estimate tunneling times. Results in Sec. 4.3 are divided into two parts (i) the geometrical structure, electronic and phononic band structure analysis (ii) Self-energy, thermalization and tunneling time analysis. The chapter ends with conclusions in Sec.4.4.

4.1 Introduction

Utilizing high-energy carriers in PV devices could improve light-to-energy conversion efficiency [75]. Despite recent progress with hot-carrier generation and injection in plasmonic nanostructures [117], the conventional semiconductor solar cells still demonstrate a superior efficiency without need for nanoscale fabrication. Alternative approaches to the problem either facilitate hot-electron transfer,

e.g. from a chemically modified surface of lead selenide to titanium oxide [7], or extend photocarrier lifetimes, *e.g.* in some perovskites [118, 119]. Van der Waals (vdW) semiconductor heterostructures formed from atomically thin 2D crystals [76] might represent a suitable platform to take advantage of both phenomena, *i.e.* ultrafast photocarrier extraction and slow photocarrier thermalization.

The possibility to assemble vdW heterostructures layer by layer allows to tune electron transfer across interfaces in the out-of-plane dimension. This interlayer charge transfer directly competes with intralayer photocarrier thermalization. The scheme has first been realized in a graphene–boron-nitride–graphene vdW heterostructure [77], where the interlayer tunneling time ranges from 1 fs to 1 ps depending on bias voltage. Since the photocarrier thermalization time in graphene spans the interval between 10 fs and 10 ps depending on carrier concentration and excitation energy [74, 79, 81, 94, 120, 121], there is a parameter range within which high-energy photocarrier extraction is feasible. Substituting graphene by a 2D TMDCs in a stack [122–125] opens new perspectives thanks to the possibility to create a diode configuration [126] and to realize stronger light-matter interactions [127]. There are already several reports on the fabrication of TMDC-based vdW heterostructures and their optoelectronic properties [128–130]. The high-energy photocarriers may be filtered by means of a boron-nitride layer, constituting a barrier for thermalized electrons and holes with low energy [129, 130]. Since the photocarrier thermalization time is sensitive to the electron and phonon spectra of each semiconductor, it is important to compare this thermalization time with the interlayer tunneling time: The high-energy photocarrier transport may not be feasible, if the former is too short. The relevant processes are sketched in Fig. 4.1. Note that we do not distinguish between the terms "hot" or "high-energy" carriers, but use them interchangably.

Light-matter interaction in 2D TMDCs has recently been explored in time-resolved photoluminescence and transient absorption spectroscopy experiments using either linearly or circularly polarized light targeting exciton and carrier dynamics [30, 31, 131–144]. Experimental and theoretical studies of 2D TMDCs have largely focused on bound states for excitation energies below the electronic bandgap, reporting exciton lifetimes [31, 135, 145], excitonic linewidths and diffusion rates [143, 144], exciton-exciton annihilation [133, 134], and exciton surface defect trapping [132]. Valley-resolved carrier dynamics has also been investigated around the band edge, and long valley depolarisation times starting from a few ps for MoS_2 [30, 31] to a few ns for WSe_2 [137–139] have been measured. Free photoexcited carrier thermalization in 2D TMDCs, arising for excitations above the bandgap, has been studied much less comprehensively [131, 136, 140–142, 146]. *Ab-initio* studies have shown that the carrier-carrier scattering is efficient far away from the band edges due to a quadratic increase of the available phase space [40, 41]. For a clean sample with no defects, the interaction with phonons thus represents the most important nonradiative channel for thermalization and cooling of photoexcited carriers in the vicinity of the valence and conduction band edges [132, 146, 147] and requires a deeper understanding.

In the present work we study the influence of SOC on photocarrier thermalization in single-layer TMDCs and additionally relate intralayer thermalization rates to interlayer tunneling rates in vdW heterostructures, important for future optoelectronic devices with improved internal quantum efficiency (IQE). We show that photocarrier thermalization is slowed down by SOC induced band splitting near valence band maximum (VBM) and conduction band minimum (CBM). Similar to interlayer transport, the thermalization occurs faster for photocarriers excited farther away from the band edges. We find, however, that the hole thermalization rate increases with excess energy in MoS_2 much more rapidly than in WSe_2. We therefore expect that the IQE of the tunneling device shown in Fig. 4.1 will strongly depend on whether MoS_2 or WSe_2 is employed.

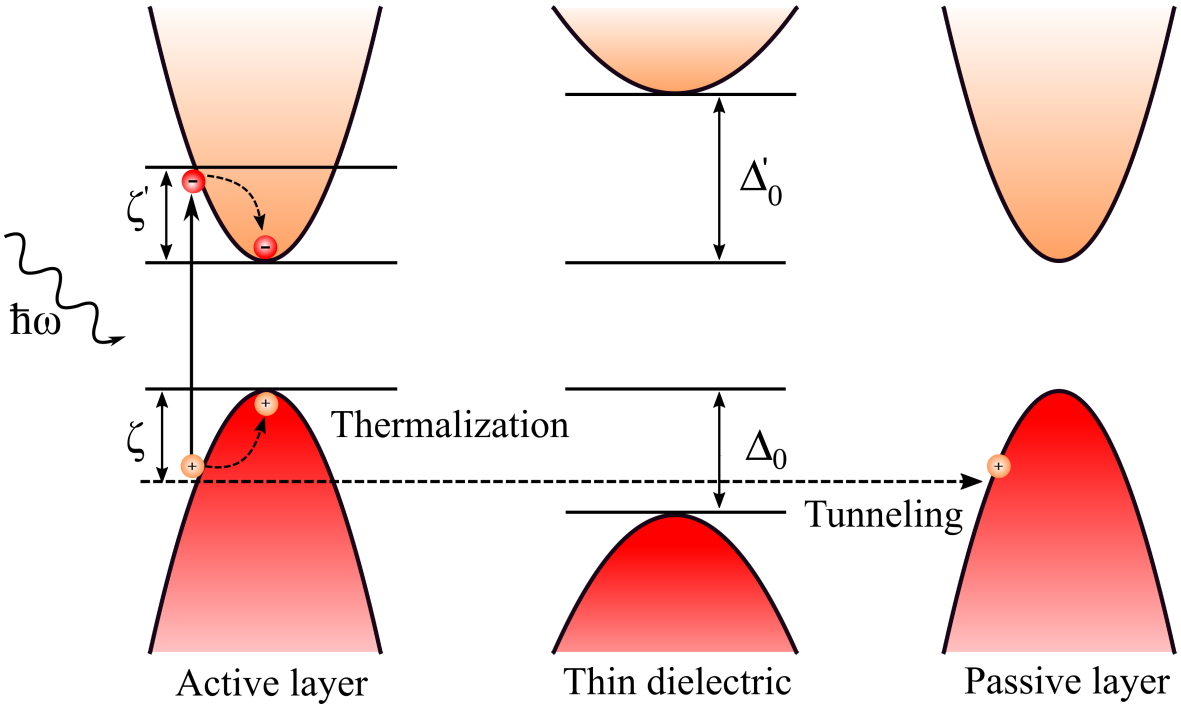

Figure 4.1: Photocarrier excitation, thermalization, and tunneling in a semiconductor–dielectric–semiconductor vdW heterostructure. A weak bias (not shown) is applied to create a current across the layers. The internal quantum efficiency (IQE) is determined by the ratio between thermalization and tunneling rates. Here, we consider transport through the valence bands because of the longer thermalization time for photoexcited holes.

4.2 Theoretical methods

4.2.1 *Ab-initio* modelling parameters

The ground state properties of the MoS_2 and WSe_2 monolayers are determined using DFT within LDA with scalar relativistic correction using QUANTUMESPRESSO. SOC is included through the Hamiltonian $\hat{\mathrm{H}}_{\mathrm{SO}}$ (in atomic units)

$$\hat{\mathrm{H}}_{\mathrm{SO}} = \frac{1}{2M^2}\frac{1}{r}\frac{dV^{\mathrm{KS}}}{dr}\mathbf{L}\cdot\sigma, \tag{4.1}$$

here, M is the mass of the nucleus, r is the radial distance from the nucleus and V^{KS} is the self-consistent Kohn-Sham potential. The contribution of the core electrons is taken into account using norm-conserving Troullier-Martins pseudopotentials with relativistic corrections [106]. For the valence configuration, 6 outermost electrons of each transition metal (Mo, W) and chalcogen (S, Se) are considered. A PW basis set with a kinetic energy cutoff of 70 Ry and a charge density cutoff of 280 Ry is employed. The unit cells and atoms in the unit cells of MoS_2 and WSe_2 monolayer are optimized simultaneously with the help of the Broyden-Fletcher-Goldfarb-Shanno algorithm, neglecting SOC until the net force on atoms is less than 10^{-6} Ry/a.u. and total energy changes are below 10^{-8} Ry. The inclusion of SOC during relaxation changes the lattice constant by less than 0.00035 Å. In order to have band structures comparable, we don't consider SOC during relaxation. The unit cells are repeated in the xy-directions but a vacuum of 18 Å is used to avoid artificial interaction in the z-direction. We

calculate every quantity with and without SOC and compare the final results. The ground state charge density is computed on $45 \times 45 \times 1$ Γ-centered **k**-grid. The electronic eigenfunctions and eigenvalues are evaluated on $24 \times 24 \times 1$ **k** grid and however, for phonon dynamical matrices we use $12 \times 12 \times 1$ **q** grids.

To construct WFs [109], we consider 7 valence bands and 4 conduction bands in case of no SOC and these numbers are doubled when SOC is included. With the localised WFs we interpolate eigenenergies, eigenfunctions and dynamical matrices on $300 \times 300 \times 1$ **k** and **q** grids which are sufficient to map the $\Sigma_{n\mathbf{k}}[T]$ on whole BZ accurately and converge the sum over **q** in Eq. (2.87). We use EPW package to compute the $\Sigma_{n\mathbf{k}}[T]$ [73].

The time evolution of the photoexcited carriers is calculated using the Eq. (2.92) and we follow the same steps as mentioned in the section 3.2 of chapter 3. The initial occupation at $t = 0$ fs is realized using a Gaussian pulse centered at excitation energy ζ which is measured with respect to the conduction and valence band edges for electrons and holes respectively and a narrow broadening $\sigma = 8.74$ meV is used. The free parameter $\tilde{\lambda}_e$ and $\tilde{\lambda}_h$ controls the number of photoexcited carriers in the conduction and valence band respectively. They are adjusted such that the different electronic DOS in valence and conduction bands yields the same number of photoexcited carriers at $t = 0$ fs. The thermalized distribution $f^{th}_{n\mathbf{k}}(T)$ in Eq (2.92) is assumed to be a Fermi-Dirac distribution as $t \to \infty$ with the quasi-Fermi level consisting the same number of photoexcited carriers as excited initially. In Eq. (2.95) for population calculations, delta function is approximated by a narrow Gaussian having a width of 20 meV. We focus on excitations above the quasi-Fermi levels so that the finite width does not affect τ_{th}.

4.2.2 Interlayer charge transport

Having the thermalization time at hand, we need a reference timescale to see whether high-energy photoexcited carriers can contribute to interlayer electron transport in vdW heterostructures, as sketched in Fig. 4.1. An accurate calculation of the interlayer transport time is a challenging task, because the carrier motion across interfaces is subject to multiple uncontrolled effects, *e.g.* interfacial roughness and impurity scattering. These effects may vary even within the same batch of samples, let alone the use of different 2D materials. In what follows, we employ a concept based on the transmission coefficient for carriers tunneling through a barrier and the uncertainty relation between the photocarrier excess energy and lifetime [77]. The advantage of the approach is that we can straightforwardly relate the transmission probability of the photoexcited carriers to a measurable quantity, namely the IQE.

Our starting point is the well-known transmission probability of carriers through a rectangular barrier of width d and height Δ_0 counted from the respective band edge, see Fig. 4.1. We assume the tunneling regime [77] so that the photocarrier excess energy is always below the barrier $\zeta < \Delta_0$. Note that according to the conventions used in this work ζ and Δ_0 are both positive, even for holes. We assume that the in-plane photocarrier momentum is not conserved due to interfacal disorder, rendering the problem effectively one-dimensional. We must, however, change the physical meaning of the incident wave vector k_z. It does not describe propagating waves anymore but is related to the out-of-plane momentum uncertainty $\Delta p_z/\hbar$, which is of the order of the size of the first BZ for 2D conductors [148]. The approximations can formally be summarized as [77, 149]

$$\mathcal{T}(\zeta) = \frac{4k_z^2\kappa^2}{\left(k_z^2+\kappa^2\right)^2 \sinh^2 \kappa d + 4k_z^2\kappa^2} \tag{4.2}$$

$$\approx \frac{4k_z^2\kappa^2}{\left(k_z^2+\kappa^2\right)^2} e^{-2\kappa d}, \quad \kappa d \gg 1 \tag{4.3}$$

$$\approx \frac{4\kappa^2}{k_z^2} e^{-2\kappa d}, \quad k_z \gg \kappa \tag{4.4}$$

$$\approx 8\frac{\Delta_0 - \zeta}{v_z \Delta p_z} \exp\left(-\frac{2d}{\hbar}\sqrt{2m(\Delta_0-\zeta)}\right). \tag{4.5}$$

In the last line, we have used the relations $\hbar\kappa = \sqrt{2m(\Delta_0-\zeta)}$ and $\hbar^2 k_z^2/m \approx v_z \Delta p_z$. Since the structure is aperiodic along the out-of-plane direction, the effective mass m of the quasiparticle moving across the interface equals the free electron mass. Importantly, there is a relation between the quasiparticle velocity, momentum uncertainty, and lifetime [148, 149]: $v_z \Delta p_z \approx 1/\tau_{\mathrm{th}}$. Note that we have assumed here that the lifetime is determined by the thermalization time. Hence, the photocarrier transmission probability can be expressed as $\mathcal{T}(\zeta) \approx \tau_{\mathrm{th}}/\tau_{\mathrm{tun}}$, where

$$\frac{1}{\tau_{\mathrm{tun}}} \approx \frac{\Delta_0 - \zeta}{\hbar} \exp\left(-\frac{2d}{\hbar}\sqrt{2m(\Delta_0-\zeta)}\right). \tag{4.6}$$

Equation (4.6) is somewhat similar to the transport time formula for a triangular barrier, employed in Ref. [77] to describe electron tunneling in the Fowler-Nordheim regime. In our case, we assume a low bias and a thin barrier such that the voltage does not appear in τ_{tun} explicitly, but it may influence Δ_0. As we need τ_{tun} solely for comparison with τ_{th} by the order of magnitude, we estimate it roughly for $\Delta_0 \approx 1$ eV and $d \approx 1$ nm. The interlayer transport time then ranges between 100 fs to 10 ps, depending on the excess energy. To gain a substantial photocurrent, the interlayer transport must not be too slow as compared with thermalization. From the experimental point of view, the ratio $\tau_{\mathrm{th}}/\tau_{\mathrm{tun}}$ is nothing else but the IQE in the tunneling limit $\tau_{\mathrm{th}} \ll \tau_{\mathrm{tun}}$. In the following section we will further analyze τ_{th}, τ_{tun} and the ratio $\tau_{\mathrm{th}}/\tau_{\mathrm{tun}}$.

4.3 Results

4.3.1 Structural, electronic and phononic properties

Monolayer MX_2 has a layered structure, and the unit cell consists 3 atoms with D_{3h} symmetry. A plane of transition atoms is sandwiched between planes of chalcogen atoms as shown in Fig. 4.2. After structural relaxation the in-plane lattice constants $|\mathbf{a}|$ for MoS_2 and WSe_2 monolayer turns out to be 3.16 Å and 3.27 Å, respectively, which is in good agreement with experiment and previous *ab-initio* calculations [150, 151].

The electronic band structures are displayed in Fig. 4.3(a,b). We find a direct bandgap of 1.74 eV at the K point in the BZ for MoS_2, while WSe_2 exhibits an indirect gap of 1.44 eV with the VBM at the K point and the CBM located on the Γ-K direction. As DFT is known to underestimate bandgaps, we apply a rigid shift to the conduction bands to arrive at GW bandgap values of 2.82 and 2.42 eV for MoS_2 and WSe_2, respectively [152, 153]. This shift modifies the bandgap values only but does not affect the time evolution of the hot carriers to be discussed later. This assumption is valid because the electronic bandgap is much larger than the highest phonon energy, and electrons and holes thus thermalize independently. Fig. 4.3(a,b) furthermore shows that the WF-interpolated band structure matches exactly with the band structure determined with the PW basis, confirming the high quality of

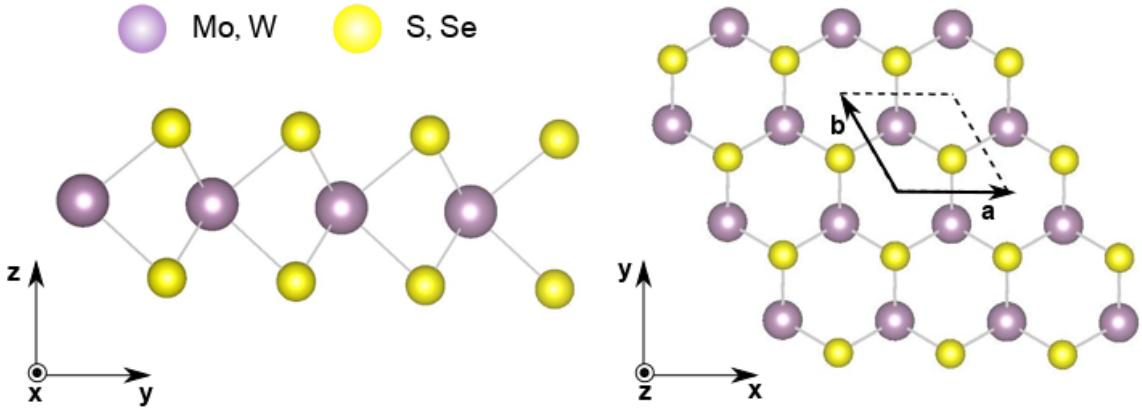

Figure 4.2: Schematic crystal structure of MX_2 viewed perpendicularly to the x- and (b) z-axis. Yellow and violet spheres represent chalcogen (S, Se) and transition metal atoms (Mo, W) respectively.

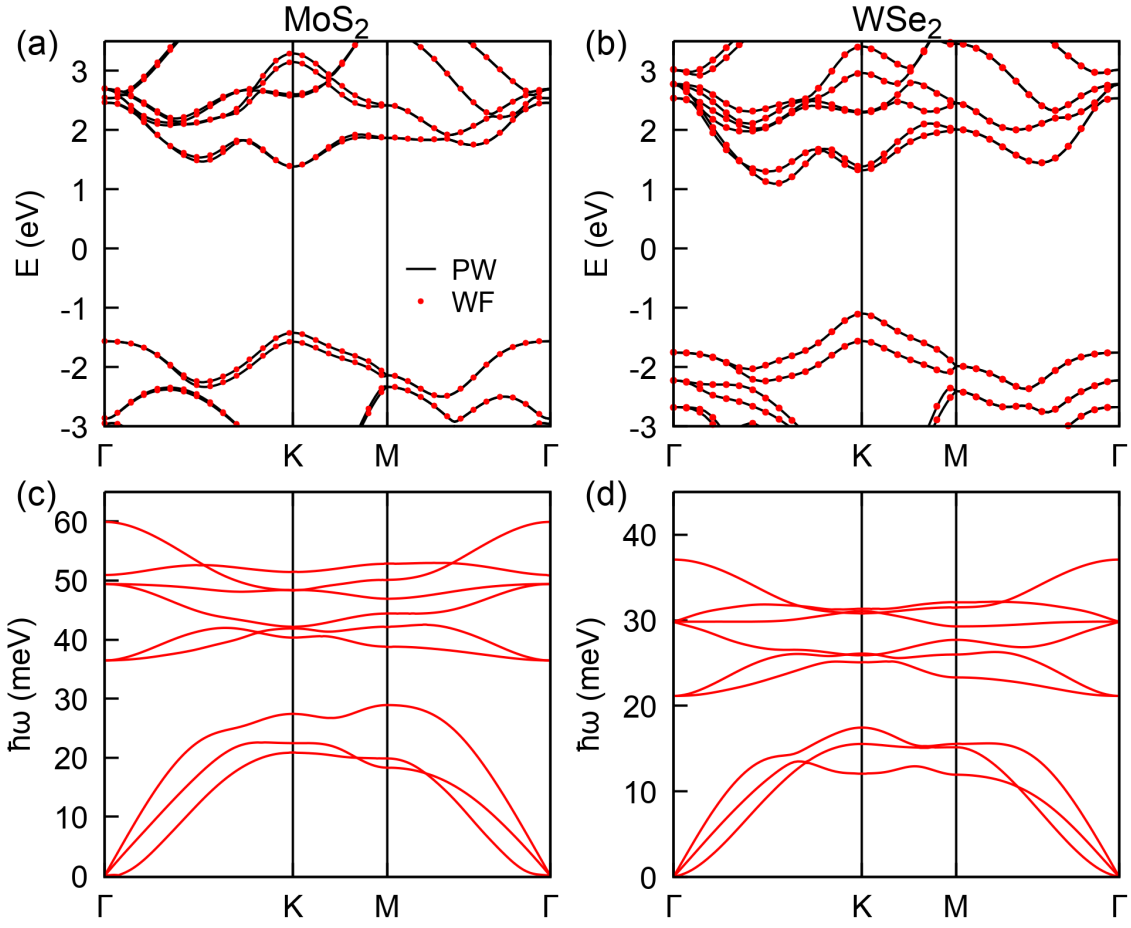

Figure 4.3: Electronic band structure for monolayer (a) MoS_2 and (b) WSe_2, calculated with PW and WFs basis sets. Phonon band structure for monolayer (c) MoS_2 and (d) WSe_2. Both electronic and phononic band structures take the relativistic SOC into account.

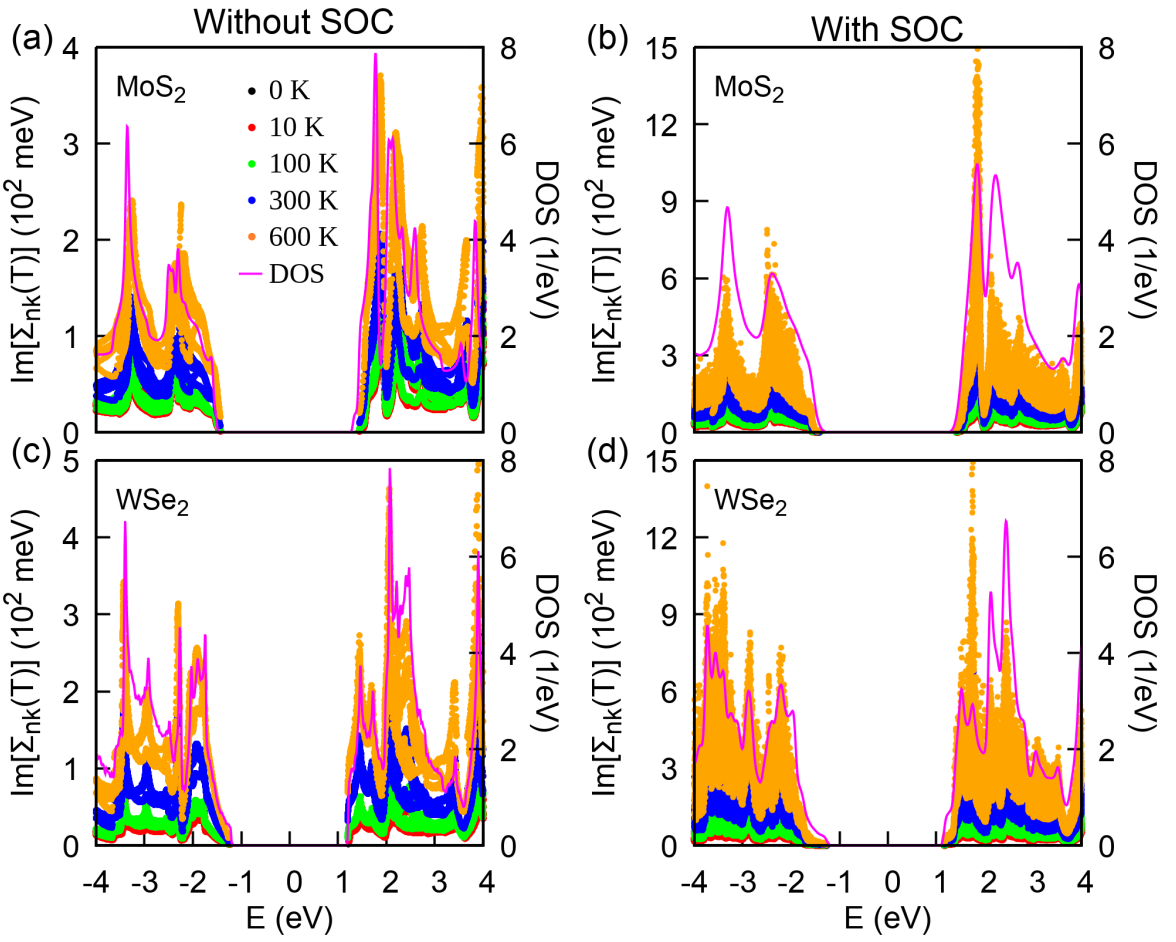

Figure 4.4: Imaginary part of the EP self-energy as a function of energy calculated for different temperatures without and with SOC for (a)-(b) MoS_2 and (c)-(d) WSe_2 monolayers. The DOS is also shown in each panel by a solid line.

the localized basis set. Due to three atoms in the unit cell MoS_2 and WSe_2 feature three acoustical and six optical modes of vibration, as it is visible from the phonon band structure in Fig. 4.3(c,d). The highest frequencies of 60 and 37 meV for MoS_2 and WSe_2 monolayers occur at the Γ point, respectively, and these values agree with previously reported ones [154, 155]. An energy gap separates acoustical and optical branches, which will be exploited in the analysis of thermalization times later. We compare our band structure with truncated Coulomb interaction along z-direction and find changes less then 1.2 meV, this justifies our 18 Å vacuum slab [not shown here].

4.3.2 Self-energy and thermalization time

We start by discussing the imaginary part of the self-energy, which is proportional to the EP scattering rate $\tau^{-1}_{n\mathbf{k}}$. Figure 4.4 shows $\mathrm{Im}\Sigma_{n\mathbf{k}}$ for MoS_2 and WSe_2 with and without SOC as a function of energy at different temperatures. The energy dependence of $\mathrm{Im}\Sigma_{n\mathbf{k}}$ follows that of the electronic DOS. This can be understood from Eq. (2.87), where the self-energy for state $|n\mathbf{k}\rangle$ is determined by a sum over all electronic states $|m\mathbf{k}+\mathbf{q}\rangle$. Considering that phonon energies are limited to below 60 meV for both materials, the sum essentially constitutes an integral over electronic states in the vicinity of $\epsilon_{n\mathbf{k}}$, which is proportional to the electronic DOS. SOC reshapes the electronic band structure by splitting

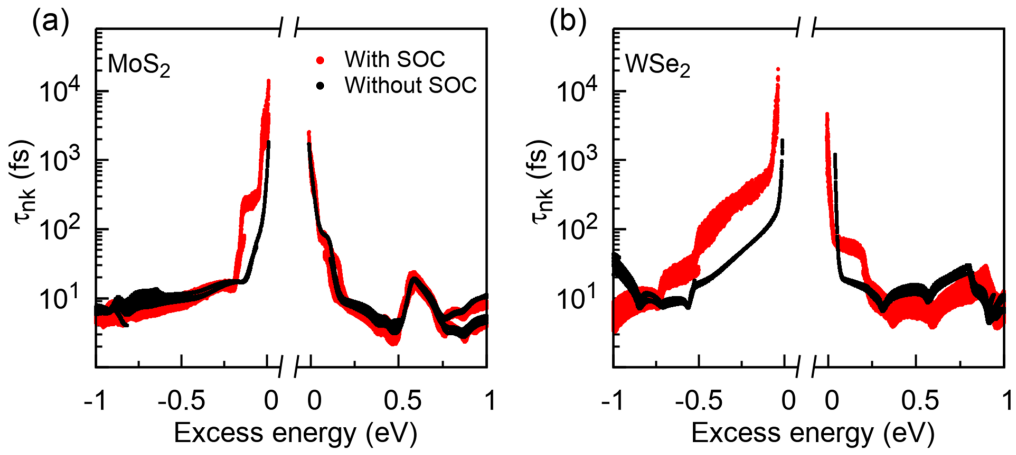

Figure 4.5: Scattering times as a function of excess energy with and without SOC for (a) MoS_2 and (b) WSe_2 at $T = 0$ K.

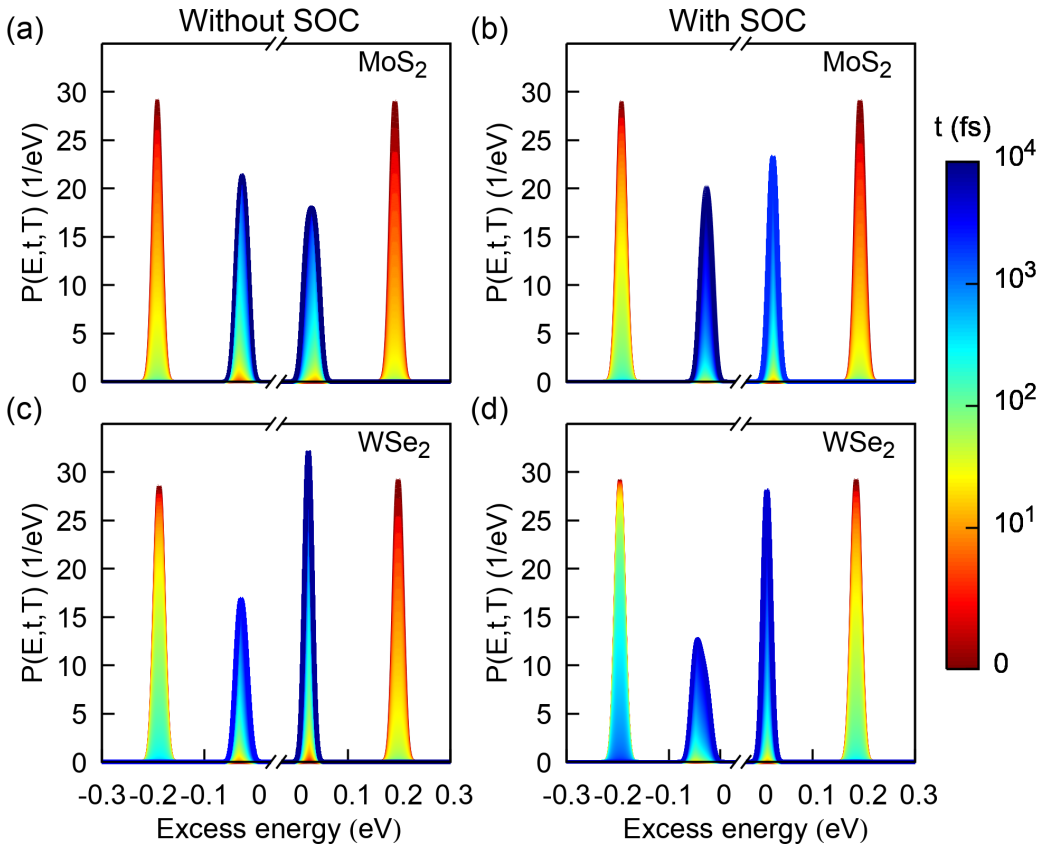

Figure 4.6: Time evolution of photoexcited carriers with and without SOC in (a)-(b) MoS_2 and (c)-(d) WSe_2 monolayers at an excitation energy of $\zeta = 0.2$ eV for $T = 0$ K. Initial and final photoexcited carrier populations correspond to a carrier density of 7×10^{12} cm^{-2}. Note that due to the large spin-orbit splitting near the valence band edge the thermalized population is rather broad in panels (b) and (d), but the area under initial and final distributions remains constant.

spin-degenerate states. On the rather large energy scales shown in Fig. 4.4, comprising excess energies of up to 3 eV, we find that this can increase the imaginary part of the self-energy as compared to the case without SOC.

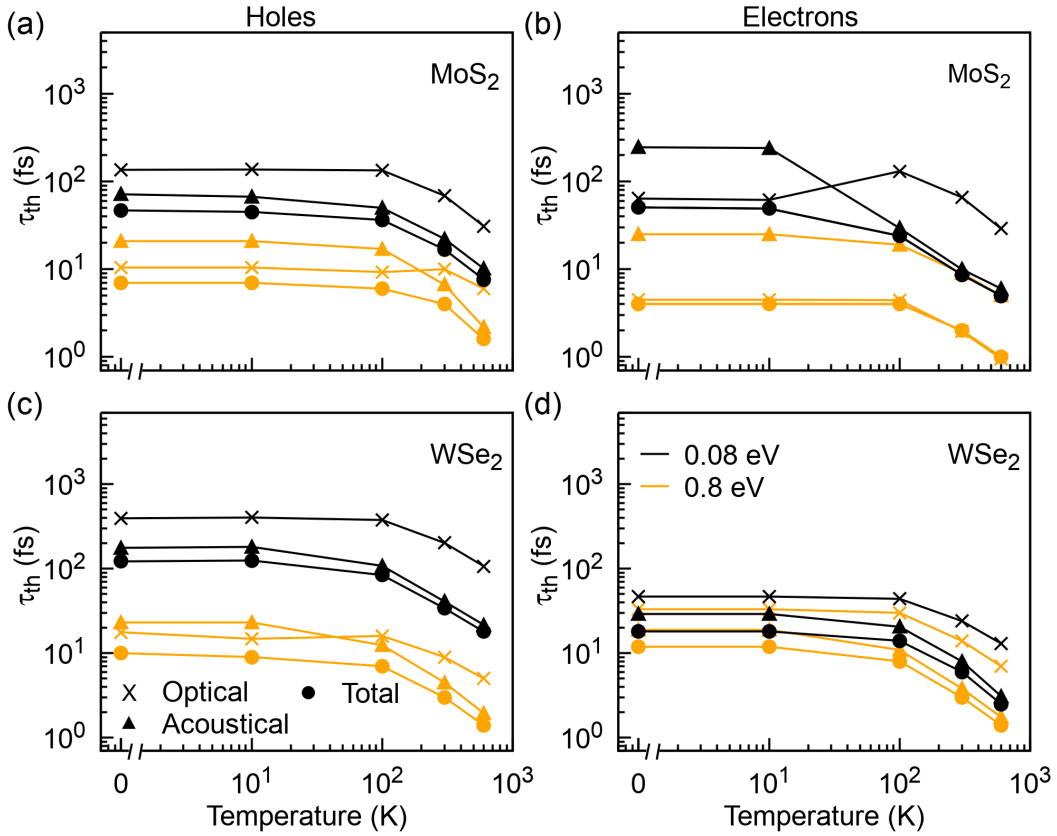

Figure 4.7: Contributions of acoustical and optical phonons to the thermalization of hot holes (left) and hot electrons (right) in (a)-(b) MoS_2 and (c)-(d) WSe_2 monolayers, neglecting SOC.

More relevant to us are the effects of SOC around the band edges. Comparing scattering times with and without SOC in Fig. 4.5, we observe that the $\tau_{n\mathbf{k}}$ are strongly increased by SOC for holes of both MoS_2 and WSe_2 and electrons of WSe_2. The electron states of MoS_2, on the other hand, are basically unaffected. The large increase of $\tau_{n\mathbf{k}}$ correlates with a large spin-orbit splitting of the corresponding valence and conduction band states in Fig. 4.3. Let us point out that similar calculations of $\tau_{n\mathbf{k}}$ have already been presented by Ciccarino *et al.* [40]. The authors have assigned the increased scattering times to the suppression of intraband scattering and spin-valley locking. In the following we extend that study by calculating thermalization times with the Boltzmann equation, by distinguishing the roles of acoustical and optical phonons in the scattering processes, and by comparing thermalization to tunneling times in vdW heterostructures.

Typical densities of carriers excited in pump-probe experiments lie between 10^{11} to 10^{13} cm^{-2} [131, 135, 156]. We adjust our free parameters $\tilde{\lambda}_\mathrm{e}, \tilde{\lambda}_\mathrm{h}$ of Eq. (2.93) such that we generate non-equilibrium populations corresponding to densities of 7×10^{12} cm^{-2} carriers in the valence and conduction bands and use the same number for all the initial state preparations throughout this chapter. The time evolution of the occupation is then calculated using Eq. (2.92) with the thermalized Fermi-Dirac distribution $f^{\mathrm{th}}_{n\mathbf{k}}$ centered at a quasi-Fermi level such that the density of 7×10^{12} cm^{-2} carriers are present after thermalization. This assumption of a conserved number of carriers is valid, because radiative recombination times of electron-hole pairs in MoS_2 and WSe_2 are on the order of a few ps

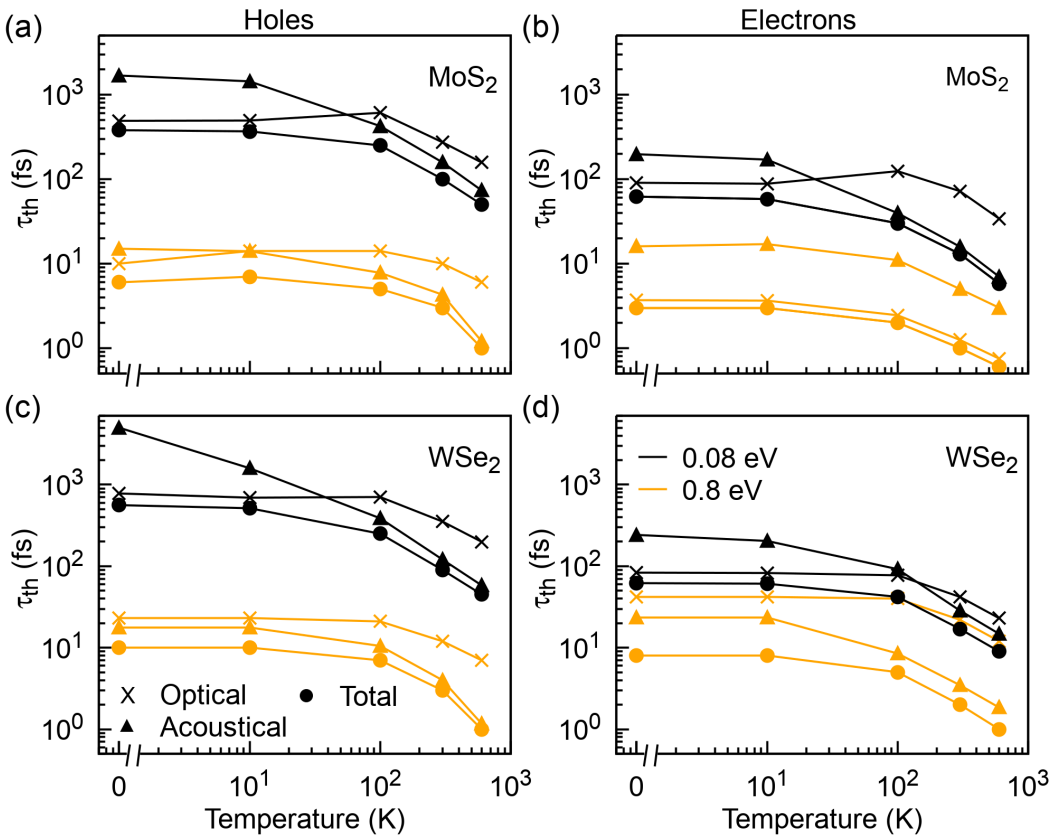

Figure 4.8: Same as Fig. 4.7 but including SOC.

[132, 135, 145]. They are thus much longer than the thermalization times that we will report in the following.

Fig. 4.6(a) shows the evolution of the hot-carrier population for MoS_2 at $T = 0$ K without SOC. In this case thermalization times of electrons and holes are comparable. Upon introducing the SOC, it can be seen in Fig. 4.6(b) that the thermalization time of holes is increased, whereas it remains almost unchanged for electrons. WSe_2 follows the same trend as MoS_2, see Fig. 4.6(c,d). We attribute this behavior to the strong spin-orbit splitting of the valence band in both MoS_2 and WSe_2.

The finite energy separation between optical and acoustical branches, observed in Fig. 4.3, makes it possible to distinguish them in $\mathrm{Im}\Sigma_{n\mathbf{k}} = \mathrm{Im}\Sigma_{n\mathbf{k}\mathrm{ac}} + \mathrm{Im}\Sigma_{n\mathbf{k}\mathrm{op}}$ and consequently in $\tau_{\mathrm{th}}^{-1} = \tau_{\mathrm{th,ac}}^{-1} + \tau_{\mathrm{th,op}}^{-1}$. In Figs. 4.7 and 4.8 we show thermalization times determined by disregarding or considering SOC, respectively. Beside the total thermalization time τ_{th} ($\bullet$) we display $\tau_{\mathrm{th,ac}}$ ($\blacktriangle$) and $\tau_{\mathrm{th,op}}$ ($\times$), calculated by taking into account only acoustical or optical phonons. In Fig. 4.7 it can be seen that thermalization of electrons and holes at low temperatures near the band edges (see the low excess energy $\zeta = 0.08$ eV) is typically dominated by low-energy acoustical phonons. The electrons of MoS_2 constitute an exception, since their thermalization is governed by optical phonons. With increasing temperature acoustical phonons keep their dominant influence on τ_{th} or start to dominant the EP scattering at $T \gtrsim 100$ K for the electrons of MoS_2. Away from the band edges (see the high excess energy $\zeta = 0.8$ eV) a rather diverse picture arises, where both acoustical and optical contributions can define thermalization. Once SOC is introduced in Fig. 4.8, the contribution of acoustical phonons is strongly suppressed for low ζ and low T, while that of the optical phonons remains nearly unaffected. For this reason the thermalization of both electrons and holes at low temperatures is fully governed by optical phonons. With increasing temperature acoustical phonons play an increasingly important

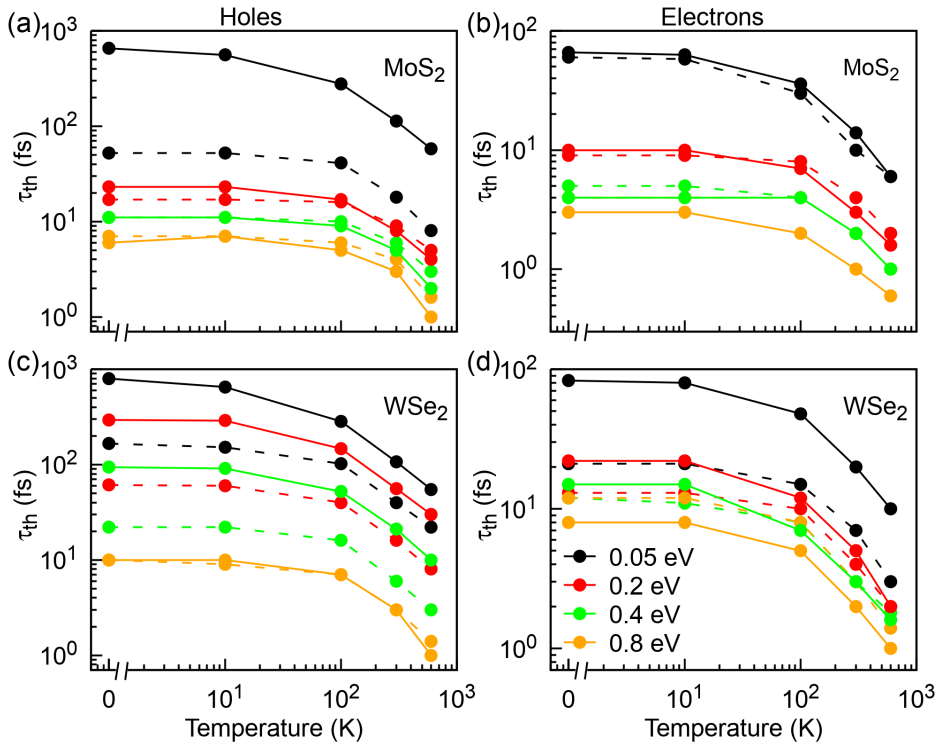

Figure 4.9: Hot carrier thermalization times for holes (left) and electrons (right) in (a)-(b) MoS_2 and (c)-(d) WSe_2 monolayers. Solid lines represent thermalization times with SOC and dashed lines those without SOC.

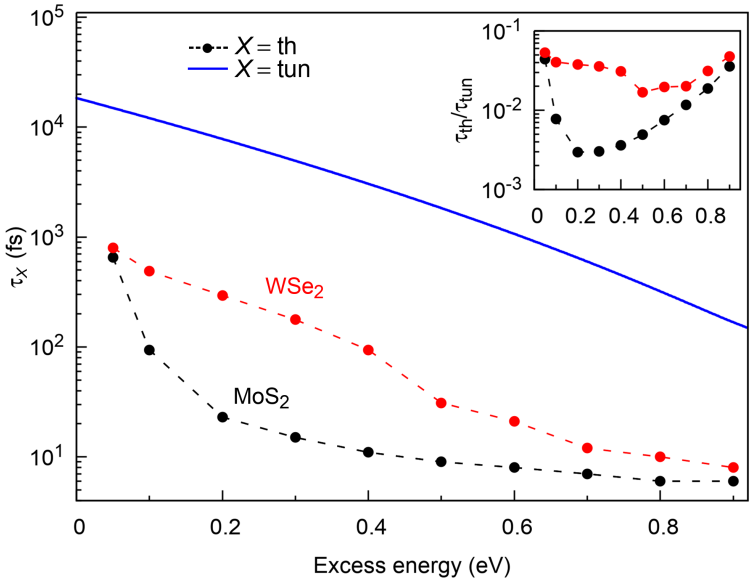

Figure 4.10: Comparison of thermalization and tunneling times for holes in MoS_2 and WSe_2 heterostructures, see Fig. 4.1, as a function of excess energy measured from the VBM. The inset shows the ratio $\tau_{\mathrm{th}}/\tau_{\mathrm{tun}}$. Thermalization times include the effect of SOC.

role and at $T \gtrsim 100$ K they define the decreasing behavior of τ_{th}. Altogether, the effects of SOC slow down thermalization near the band edges.

We summarize the total thermalization time τ_{th} in Fig. 4.9 as a function of temperature for different excess energies. The dashed curves represent the thermalization time without SOC, and the solid curves include SOC. While SOC strongly increases the thermalization time at low T near the band edges, τ_{th} may also decrease (see for instance $\zeta = 0.8$ eV in Fig. 4.9(d)) depending upon the band structure and EP couplings. For a fixed excitation energy the thermalization time generally decreases with increasing temperature, because more phonons are accessible to scatter on electrons and holes. The same trend has been reported in pump-probe experiments performed on five-layer MoS_2 [131], where the drop of τ_{th} has been observed for electrons at around $T = 300$ K. Fig. 4.9(a,b) suggests that it occurs around 100 K for MoS_2 in our theory. It should however be emphasized that we study perfectly crystalline, free-standing layers in vacuum. The presence of a substrate, defects and interlayer interactions thus complicates a comparison with the experimental results. A qualitative agreement is nevertheless achieved.

As visible in Fig. 4.9, free carriers near the band edges feature longer relaxation times as compared with those at higher excess energies. The reason is the lower electronic DOS available for scattering around the band edges. Caused by multiple valleys in the conduction band, see Figs. 4.3 and 4.4, electrons thermalize faster than holes in both MoS_2 and WSe_2. Due to the heavier elements composing WSe_2, the SOC-related splitting at both the valence and conduction band edges is larger than in MoS_2. This alters the thermalization time of both electrons and holes. However, electrons still thermalize one order of magnitude faster than holes around band edges. We note that our calculated thermalization times of electrons in MoS_2 for $\zeta = 0.05$ eV amount to 63 and 36 fs at 10 and 100 K, respectively, which is of a similar magnitude as found in Ref. [142], where $\tau_{\text{th}} \approx 30$ fs at $T \approx 50$ K.

Since our calculations predict that holes thermalize more slowly than electrons in both MoS_2 and WSe_2, we focus on hole transport to discuss the IQE of the tunneling device presented in Fig. 4.1. The heterostructure that we have in mind thus consists of two single-layer of 2D TMDCs at the outside, which are separated by a 1 nm thick dielectric film that establishes a tunneling barrier Δ_0 of 1 eV to the VBM of the single-layer. Figure 4.10 shows how the photoexcited hole thermalization time τ_{th} compares to the tunneling time τ_{tun} of Eq. (4.6) as a function of the excess energy ζ. Surprisingly, τ_{th} follows the same trend as τ_{tun} for WSe_2. The ratio $\tau_{\text{th}}/\tau_{\text{tun}}$ thus depends only weakly on ζ, as visible in the inset of Fig. 4.10. This suggests that the IQE of the vdW heterostructure stays rather constant with regard to increasing photocarrier excess energy. This contrasts to the case of MoS_2, where τ_{th} drops much faster than τ_{tun} when ζ increases. Hence, we expect that an analogous MoS_2-based tunneling device will demonstrate a pronounced decay in the IQE once the photocarriers are excited away from the band edges. Ultimately, our calculations trace back this effect to the larger SOC-induced valence band splitting of WSe_2 as compared to MoS_2 in these otherwise similar materials, see Fig. 4.3.

4.4 Conclusions and outlook

In the relevant region near the band edges we find that the inclusion of SOC generally increases the thermalization times by up to an order of magnitude. Our analysis assigns this effect to a suppression of acoustical phonon scattering, while thermalization by optical phonon remains basically unaffected. In both monolayers electrons thermalize almost one order of magnitude faster than holes. We have additionally estimated the tunneling time of a TMDC-based heterostructure using an analytical model. The ratio of thermalization and tunneling times decreases weakly with photocarrier excess energy in WSe_2, whereas it drops quickly for MoS_2 when moving away from the WF. Our calculations hence suggest that tunneling devices based on WSe_2 monolayers will have a higher IQE than MoS_2-based systems.

Chapter 5

Charge carrier thermalization in bulk and monolayer CdTe

The 2D materials we have studied so far have hexagonal structures and can be exfoliated from their bulk crystals by reducing the number of layer from infinity to one. In this work, we decided to explore group II-VI semiconductor which exists primarily in cubic structures in nature. One of the most popular choice in this group is CdTe which is a direct gap material and an excellent choice for devices based on light matter interaction. Bulk CdTe has zinc blende structure. Through the *ab-initio* calculations we make prediction that the stable monolayer CdTe can be cleaved along [110] facet which has rectangular unit cell. We perform the similar studies as done in Ch. 3 and 4 for graphene and TMDCs respectively on CdTe in this chapter. We find that the thermalzation time is constant for electrons in single-layer CdTe up to 500 meV of excess energy. This is consistent with the current understanding of constant electronic DOS of parabolic band in 2D limit.

The chapter is organised as follows. We start with the motivation behind the present studies in Sec. 5.1 and then provide with the technical details of the simulations in Sec. 5.2. In Sec. 5.3 we discuss the calculated electronic and phononic properties, EP scattering rates, and photocarrier thermalization times using the computational methods described in Ch. 2. The main findings of the present work are summarised in Sec. 5.4. This chapter up to large extent is from our own work Ref. [157] and will be submitted shortly.

5.1 Introduction

A direct bandgap facilitates the interband absorption in semiconductors, because of the vanishing momentum mismatch in optical transitions between the VBM and CBM. Group II-VI and III-V semiconductors exhibit a direct bandgap and are therefore excellent candidates to exploit interband optical transitions. One of the popular choices among this group is CdTe, being a direct-bandgap semiconductor used in electro-optic modulators and nuclear detectors [158]. Its most prevalent commercial application is in PV as a component of cadmium sulfide (CdS)-CdTe junctions [159]. State of the art CdS-CdTe solar cells have reached impressive 21% PV efficiency [3] defined as a ratio of the electrical power density to the incident light power density in the optimal operating regime under the standard test condition.

Recent progress in nanofabrication technologies has made it possible to reduce the thickness of CdTe crystals to just a few layers [160] and even to roll the layers up into nanoscrolls [161]. Atomically thin layers of other members of the group II-VI semiconductors have also been synthesized recently [160, 162]. In particular, a four-layer-thick zinc selenide (ZnSe) slab cleaved along the [110] facet of the bulk crystal has been shown to be stable [163]. Note that bulk CdTe features the same zinc

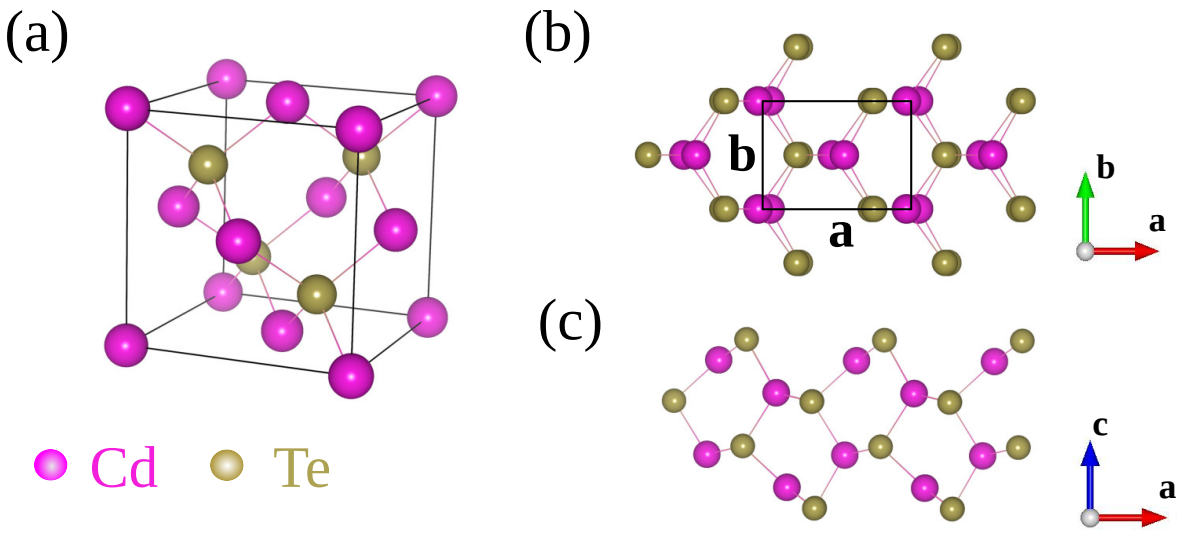

Figure 5.1: Energy-optimized crystal structure for (a) bulk CdTe in the zinc blende phase and monolayer CdTe cleaved along the [110] facet in (b) top and (c) side views. The lattice vectors $\mathbf{a}$, $\mathbf{b}$, $\mathbf{c}$ are indicated for each of the monolayer structures.

blende crystal structure as ZnSe, see Fig. 5.1(a). Keeping in mind this tremendous progress, we anticipate fabrication of monolayer CdTe in the near future, because first principles studies suggest that this material is dynamically stable [164–166]. In this work we address what happens with the ultrafast dynamics of photoexcited carriers in CdTe films, once their thickness is reduced down to the fundamental limit of a monolayer, as shown in Fig. 5.1(b).

Such extremely thin CdTe films belong to the class of atomically thin or 2D materials such as graphene [8], TMDCs [10], 2D oxides [167], germanane [168], and phosphorene [169]. 2D materials show properties drastically different from their bulk counterparts due to quantum confinement. For example, TMDCs demonstrate a transition from indirect to direct gap when reduced from the bulk to a monolayer, resulting in strong excitonic photoluminescence peaks [10, 29]. Interestingly, the opposite behavior of a direct to indirect bandgap can be observed in metal monochalcogenides, leading to a vanishing of the excitonic absorption in stacks that are less than 8 layers thick [11]. The peculiar optical properties make 2D materials promising for photodetection and other photonic applications [35, 124, 170–172].

To understand the microscopic details of hot-carrier dynamics in CdTe, both theoretical and experimental efforts are necessary. There are several pump-probe studies on the electron-spin relaxation in bulk CdTe, highlighting the role of photoexcited carrier density and excitation energy [173–175]. In the pump-probe studies the carriers mainly thermalize via emission of optical phonons and interactions with defects [173, 175, 176]. Although surface phonons in the group II-VI semiconductors have also been investigated [177], their role in photocarrier thermalization is still unknown. In perfect crystals the dominant mechanisms involved in hot-carrier scattering are electron-electron and EP interactions [6]. It is well established by means of *ab-initio* methods that the EP scattering plays a major role near the band edges [40–42]. We therefore focus on the EP scattering in this paper and proceed similar to a previous work [74], where we studied the photocarrier thermalizaton bottleneck in graphene. We show that the thermalization process is qualitatively different, depending upon whether CdTe is bulk or 2D. The respective thermalization times differ by orders of magnitude and demonstrate a distinct behavior upon excess energy and temperature changes.

5.2 *Ab-initio* modelling parameters

We use DFT within the LDA including the SOC as implemented in QUANTUMESPRESSO [63] to calculate the ground state properties of monolayer and bulk CdTe. The core electronic contribution to the Kohn-Sham potential is taken with Troullier-Martins pseudopotential [106] with scalar relativistic correction. The valence electronic configuration has six electrons from both Cd and Te. We use a PW basis set with kinetic energy cutoff of 70 Ry and charge density cutoff of 280 Ry. To simulate the monolayer CdTe, unit cell is repeated in xy-direction and a vacuum of 18 Å along z-direction is used to isolate the monolayer from its periodic images in z-direction. The unit cell and atoms are relaxed simultaneously using Broyden-Fletcher-Goldfarb-Shanno algorithm for both bulk and monolayer CdTe until the net force on atoms is less than 10^{-6} Ry/a.u. and total energy changes are below 10^{-8} Ry. To compute the ground state charge density including SOC, we employ a Γ-centered $\mathbf{k}$-grids with dimensions of $12 \times 12 \times 12$ for bulk and $9 \times 12 \times 1$ for monolayer. To obtain dynamical matrices and eigenfrequencies from DFPT [108], we use $6 \times 6 \times 6$ and $9 \times 12 \times 1$ $\mathbf{q}$-grids for bulk and monolayer respectively.

Once electronic and phononic band structures of relaxed systems have been calculated, we evaluate the electronic self-energy $\Sigma_{n\mathbf{k}}(T)$ as defined in the Eq. (2.87) in the lowest order of the EP interaction for a given electron band n, a wave vector $\mathbf{k}$, and the temperature T using the EPW code [73]. With the help of localised WF [178] we evaluate electronic eigenfunctions, eigenvalues and phonon dynamical matrices on fine grids. We find that fine $\mathbf{k}$ and $\mathbf{q}$ grids of size $45 \times 45 \times 45$ for bulk and $300 \times 300 \times 1$ for monolayer CdTe are sufficient to converge the sum over $\mathbf{q}$ in Eq. (2.87).

We follow the same procedure as mentioned in section 2.4 of Ch. 2 to calculate the time evolution of the photoexcited carriers. It should be noted that we use $\sigma = 8.74$ meV. The free parameter $\tilde{\lambda}_{e/h}$ is adjusted such that the different electronic DOS in valence and conduction bands yields the same number of photoexcited carriers at $t = 0$ fs. The thermalized distribution $f^{th}_{n\mathbf{k}}$ and ζ are same as defined in the Sec. 4.2 of Ch. 4.

5.3 Results

5.3.1 Structural, electronic and phononic properties

Bulk CdTe possesses the zinc blende structure with a relaxed lattice constant of $|\mathbf{a}| = 6.42$ Å, see Fig. 5.1(a), and shows Cd-Te bonds of mixed covalent-ionic character with lengths of 2.87 Å, in good agreement with experimental values [179]. All the facets except [110] exhibit a polar surface and are therefore unstable [180]. This is the reason, why we cleave CdTe along the [110] facet to obtain a stable monolayer. As shown in Fig. 5.1(b)-(c), the monolayer unit cell consists of 8 atoms: 4 Cd, 4 Te, and each Cd atom is bonded to three Te atoms and vice versa. Due to the energy optimization of the unit cell, exterior Cd atoms are pulled into the layer, resulting in a rippled surface. We find lattice parameters of monolayer CdTe to be $|\mathbf{a}|$ = 6.20 Å, $|\mathbf{b}|$ = 4.48 Å, and Cd-Te bond lengths to vary in the interval of 2.72 to 2.83 Å, in agreement with a previous DFT study of monolayer CdTe [181].

Fig. 5.2(a)-(b) shows the electronic band structures for bulk and monolayer CdTe along with the corresponding DOS. Both materials exhibit a direct bandgap with the VBM and CBM located in the center of the BZ, i.e. at the Γ point. As visible in Fig. 5.2(a), the bulk valence band at the Γ point is four-fold degenerate, and the spin-orbit split-off band is shifted down from the VBM by about 0.8 eV. The VBM of the monolayer is two-fold degenerate, but the degeneracy is quickly lifted away from the Γ point, see Fig. 5.2(b). We construct WFs from the PW basis, and the excellent match between WF-interpolated and PW-derived band structures demonstrates the quality of the WFs. DFT in the LDA is not able to predict the bandgap values reliably, and more advanced methods are required for

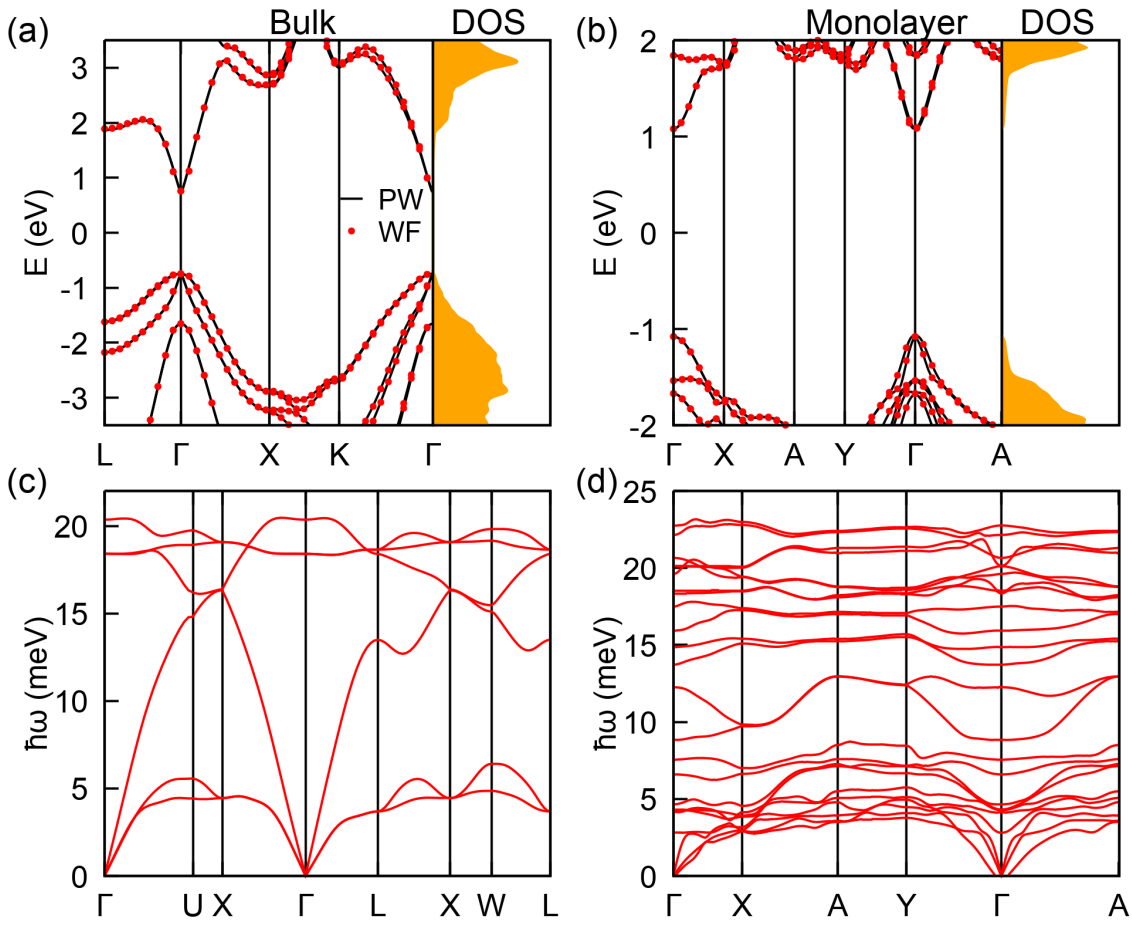

Figure 5.2: Electronic band structure calculated using PW and WF basis sets for (a) bulk and (b) monolayer CdTe. The corresponding DOS is shown in arbitary units to the right of the band structure. Phononic band structure for (c) bulk and (d) monolayer CdTe.

this purpose like DFT with hybrid exchange-correlation functionals or the GW approximation. We compute DFT bandgap values for bulk and monolayer CdTe of 0.18 and 1.2 eV, respectively. To correct the bandgaps, we perform a rigid shift of occupied and unoccupied electronic bands to match with the experimental value of 1.5 eV for bulk and with calculations using the Heyd–Scuseria–Ernzerhof functional of 2.13 eV for monolayer CdTe [181, 182]. While the shift modifies the electronic gap sizes visible in Figs. 5.2(a)-(b) and self-energy 5.3, the temporal dynamics studied in Figs. 5.4 and 5.5 are not affected by this choice. Since the electronic bandgap is much larger than maximum phonon frequencies, see Fig. 5.2, electrons and holes thermalize separately in our model.

The phonon spectrum of bulk CdTe is well studied, and it shows LO-TO splitting of around 2 meV at Γ-point. Our result in Fig. 5.2(c) matches well with the phonon band structure calculated previously [183]. Monolayer CdTe, featuring 8 atoms in the unit cell, gives rise to 3 acoustical and 21 optical modes with the highest LO mode energy of 23 meV reached between the Γ and X points, see Fig. 5.2(d). This agrees with the DFT results of Ref. [181]. Positive frequencies throughout the BZ ensure the dynamical stability of monolayer CdTe.

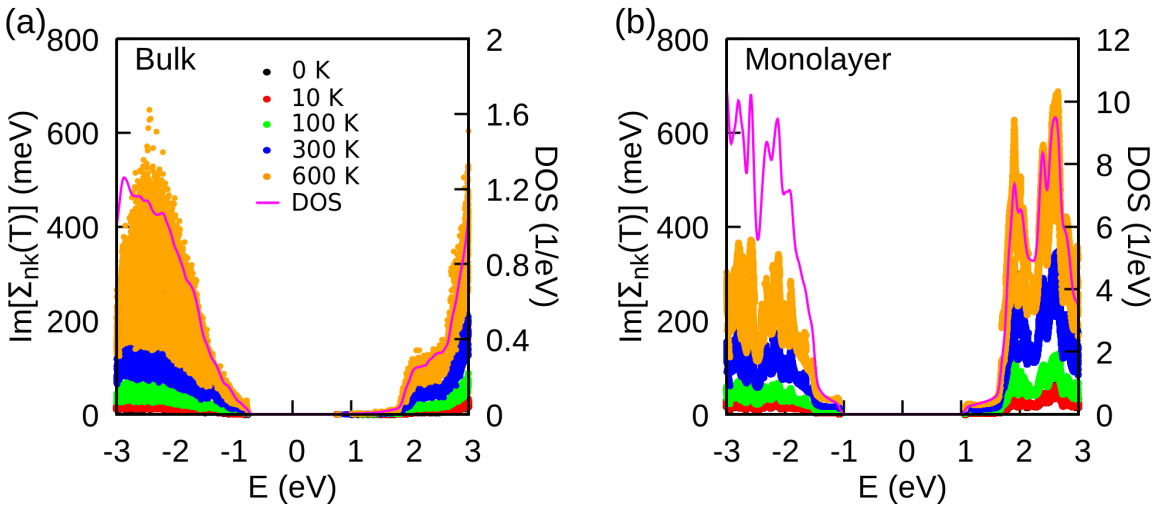

Figure 5.3: Imaginary part of the EP self-energy in Eq. (2.87) as a function of energy at different temperatures, and the carrier DOS for (a) bulk and (b) monolayer CdTe.

5.3.2 Self-energy and thermalization time

Fig. 5.3(a) shows the imaginary part of the self-energy Im$[[\Sigma_{n\mathbf{k}}(T)]$ for bulk CdTe as a function of energy at different temperatures. The imaginary part of the electronic self-energy exhibits small values from 0.75 eV up to 1.75 eV because of the two-fold spin-degeneracy in the conduction band, precluding interband scattering. At higher energy Im$[\Sigma_{n\mathbf{k}}(T)]$ shows a sudden increase, reaching a plateau just above 2 eV that is followed by a second step at 2.7 eV. These abrupt changes around 1.75 eV and 2.7 eV take place when the CBM at the L and X valley, respectively, enter the energy window. The energy dependence of Im$[\Sigma_{n\mathbf{k}}(T)]$ follows the electronic DOS, because the latter determines the available phase space for EP scattering events. In contrast to the degenerate conduction band, the presence of multiple valence bands allows for both inter- and intraband transitions. As a consequence, Im$[\Sigma_{n\mathbf{k}}(T)]$ increases smoothly with energy for holes. For electrons and holes, the EP scattering increases in efficiency at higher temperatures because the number of phonons increases, facilitating phonon absorption by both carrier types.

Fig. 5.3(b) shows Im$[\Sigma_{n\mathbf{k}}(T)]$ for monolayer CdTe. It keeps a constant value from 1.07 eV up to 1.5 eV and then abruptly increases due to the local minimum in the conduction band around the Y point. In the case of holes, Im$[\Sigma_{n\mathbf{k}}(T)]$ remains constant from -1.07 eV down to -1.2 eV and then also increases due to the second VBM at the Γ point. The band structure becomes increasingly complex at higher excitation energies away from the band edges, and multiple extrema in the electronic band structure give rise to several peaks in Im$[\Sigma_{n\mathbf{k}}(T)]$ for electrons and holes.

To analyze the photocarrier thermalization time, we set the reference level for the excess energy of hot holes and electrons to the valence and conduction band edges, respectively. Fig. 5.4 shows the evolution of the hot-carrier population, starting from the initial one comprising 10^{17} cm^{-3} and 10^{11} cm^{-2} hot carriers at an excess energy of 0.2 eV for bulk and monolayer CdTe, respectively. The thermalized population is obtained from the Fermi-Dirac distribution, with the quasi-Fermi level set to a value that reproduces the same carrier concentration as initially present. This assumption is valid as long as the photocarrier thermalization is much faster than the electron-hole recombination. Recombination times for carriers in bulk CdTe are reported[184] to vary from 670 to 60 ns at concentrations from 10^{16} to 10^{17} cm^{-3}. Fig. 5.4(a)-(b) shows the hot carrier populations for bulk CdTe. The spin-degenerate conduction band limits the EP scattering, slowing down electron thermalization

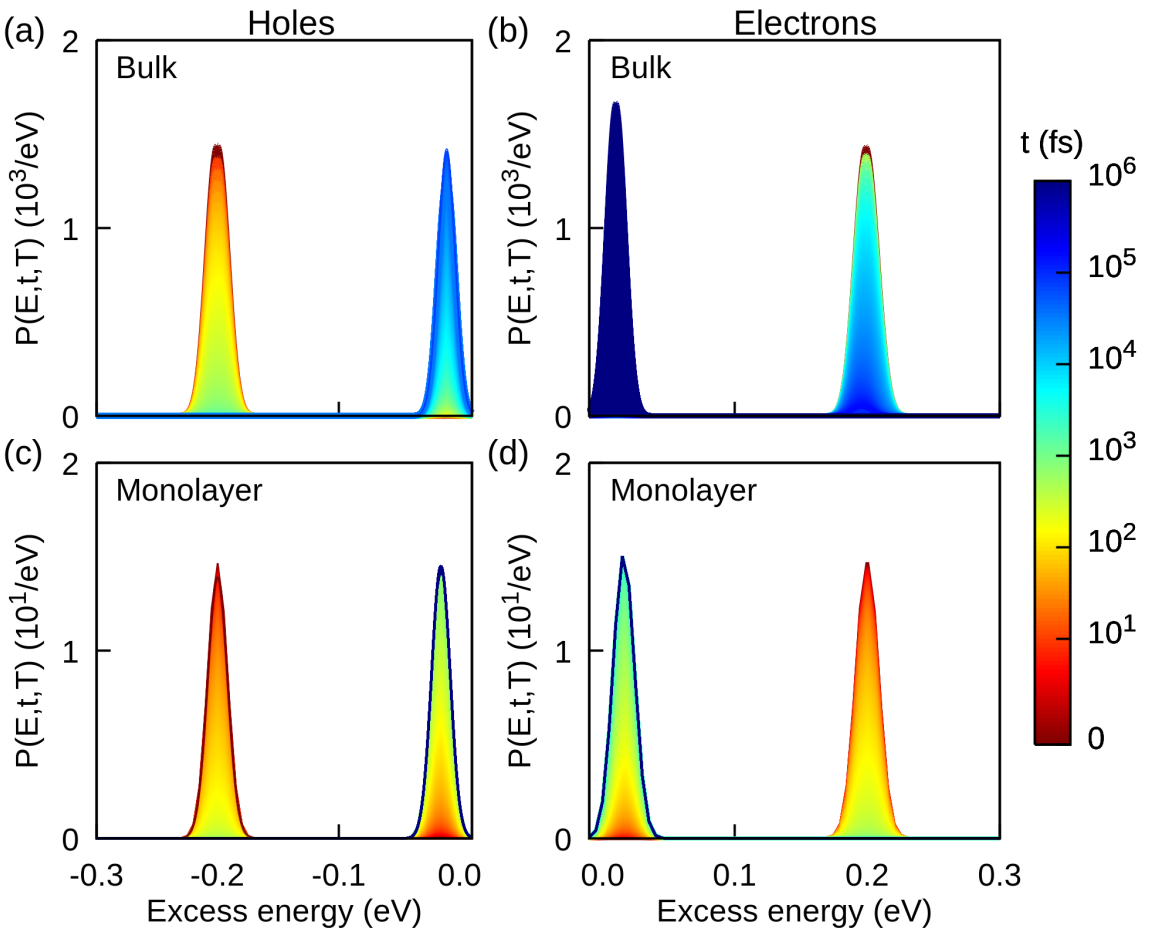

Figure 5.4: Temporal evolution of hole (left column) and electron (right column) populations, calculated separately using the Boltzmann equation in the RTA for (a)-(b) bulk and (c)-(d) monolayer CdTe at $T = 10$ K. The initial carrier excess energy, counted from the respective band edges, is 0.2 eV. Initial and final populations correspond to photocarrier densities of 10^{17} cm^{-3} for bulk and of 10^{11} cm^{-2} for monolayer CdTe. The color scale indicates the time evolution (red for early, blue for late times). Note that the Gaussian shape of the thermalized population is a consequence of our choice to represent the delta function in Eq. (2.95) by a Gaussian.

substantially as illustrated by the blue color. In contrast, the holes thermalize much faster because of the broken degeneracy away from the VBM, allowing for both inter- and intraband scattering. Fig. 5.4(c)-(d) demonstrates that electrons and holes thermalize approximately at the same rate in monolayer CdTe, but the rate is much higher than in the bulk case. The reason becomes clear from Fig. 5.2(c)-(d): Monolayer CdTe possesses a rich phonon spectrum that provides much more scattering channels than its bulk counterpart.

Fig. 5.5 summarizes our main outcomes regarding the thermalization time τ_{th}, defined in Eq. (2.94). We study τ_{th} as a function of temperature over a range of excess energies $|\zeta| = 0.1, 0.2, 0.4, 0.8$ eV. In the case of bulk CdTe, holes thermalize approximately two orders of magnitude faster than electrons at the same excess energy, see Fig. 5.5(a)-(b). In the case of monolayer CdTe, the hole and electron thermalization times are of the same order of magnitude. But interestingly there is either very weak or almost no change of the τ_{th} for electrons up to an excess energy of about 0.5 eV due to the degenerate conduction band and the constant DOS in this region. Thermalization times generally shorten with

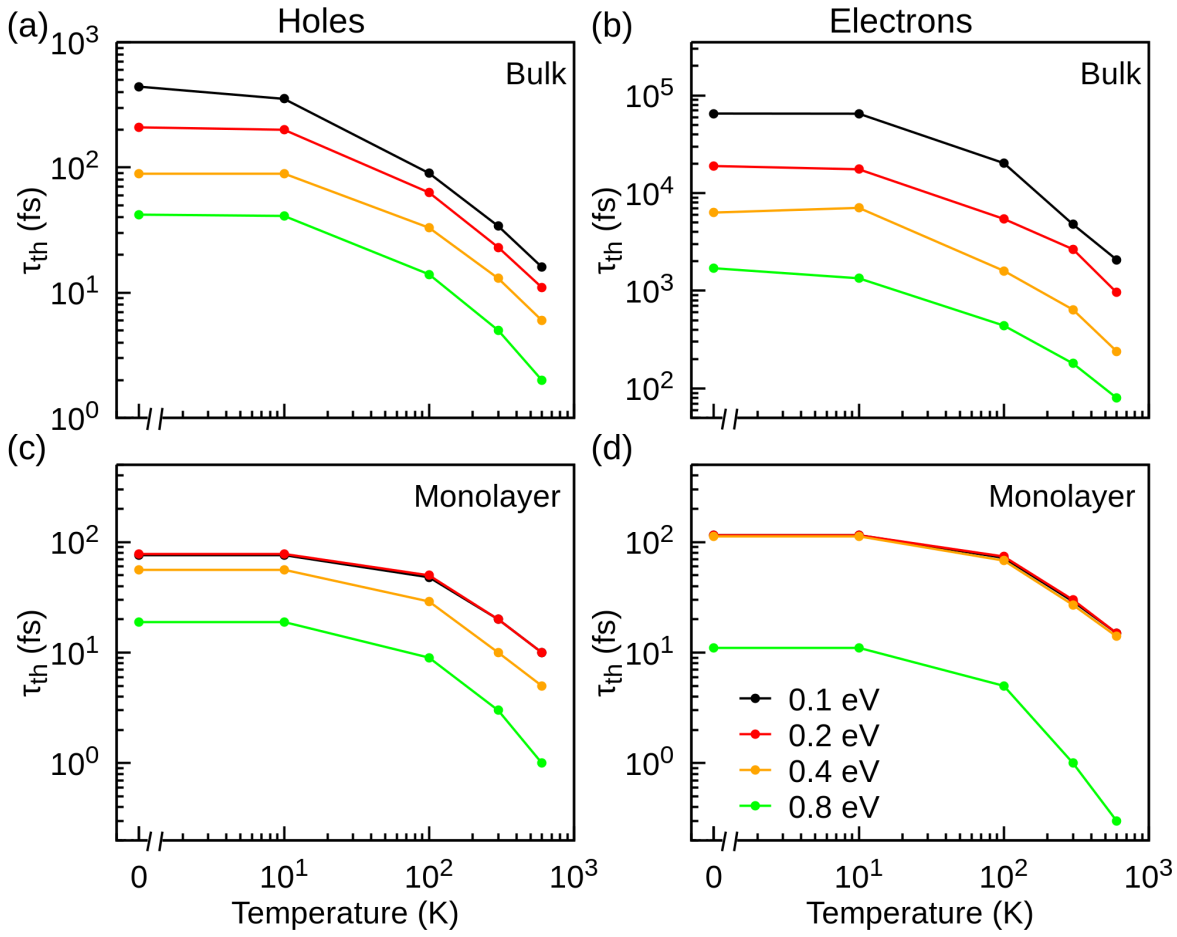

Figure 5.5: Thermalization time for holes (left column) and electrons (right column) as a function of temperature over a range of initial excess energies for (a)-(b) bulk and (c)-(d) monolayer CdTe.

increasing temperature, and the reduction accelerates at temperatures above 100 K. Fig. 5.5(c)-(d) suggests extremely fast thermalization ($\tau_{\mathrm{th}} < 20$ fs) in monolayer CdTe at high temperatures about 600 K. Nearly identical thermalization times for electrons and holes at low excess energies arise from a comparable DOS around the conduction and valence band edges.

It is instructive to compare our findings regarding thermalization time with pump-probe spectroscopy data. Unfortunately, data for monolayer CdTe is not available yet. The thermalization time in bulk CdTe can be deduced from polarization-resolved pump-probe experiments [173–175]. We can assume that the photocarrier occupation is thermalized once the oppositely polarized probes become indistinguishable. This corresponds to the pump-probe delay time of the order of 10 ps [174, 175] but the time may be lower in doped samples [173]. In particular, Ma and Leng [175] report the relaxation time of 53 ps at 70 K with excess energy of 0.05 eV. Our calculated thermalization time for electrons at excess energy 0.1 eV is 65 ps and 20 ps at 10 K and 100 K, respectively. The agreement justifies our approach to some extent and makes to believe that our predictions regarding monolayer CdTe are correct as well.

5.4 Conclusions and outlook

We have studied the carrier thermalization in bulk and monolayer CdTe within a range of up to 0.8 eV away from the band edges. At low temperature, the photoexcited carriers in bulk CdTe thermalize on a 0.1–100 ps timescale, whereas in monolayer CdTe this process completes within 10-100 fs. Increased temperatures generally reduce the thermalization time. Our observations are consistent with the current understanding that reduced dimensionality alters the EP scattering rate [6] drastically changing carrier thermalization. The thermalization time also depends on the excitation energy and is, in general, substantially reduced, if the carriers are excited far away from the band edges. Our most unexpected observation is that the photoexcited electrons in monolayer CdTe comprise an exception from this rule: Their thermalization time does not depend on excess energy up to about 0.5 eV. We attribute the behavior to a parabolic conduction band that forms in the monolayer and whose band minimum is well separated from the other conduction bands.

One of the promising strategies for increasing the amount of work done per absorbed photon is speeding up the photocarrier extraction into the external electrical circuit [7]. The carriers are then collected, while they are still hot or even out of thermal equilibrium. The saved excess energy can then be utilized for increasing the photoresponse. 2D materials might offer unprecedented opportunities along this path: Their thickness is so small that the photoexcited carriers could be extracted well before they thermalize and reach ambient temperature by means of phonon emission. The mechanism has recently been studied in a graphene-based vdW heterostructure [77]. The hot photocarriers are filtered out by a potential barrier so that only the carriers having high enough excess energy can contribute to the photocurrent. However, the photocarrier thermalization time usually drops substantially with increasing excess energy, as one can see in Fig. 5.5(a)-(c). This is also true for other popular 2D semiconductors, including MoS_2 or WSe_2. Hence, high excess energy and slow thermalization are two conflicting requirements which are probably impossible to satisfy at the same time. Our main result, shown in Fig. 5.5(d), suggests that monolayer CdTe is a great exception: electron thermalization does not significantly depend on excess energy. Clever utilization of this effect may help to circumvent the problem of hot photocarrier extraction.

Chapter 6

Additional project: Layer dependent absorption studies for few-layer GaSe

In this chapter, we present our experimental and theoretical results for the layer dependent absorption spectra of ϵ-GaSe crystal. We measure the optical absorption via highly sensitive differential transmission measurements. We calculate the band structure and absorption spectra within RPA of ϵ-GaSe w.r.t number of layers ranging between 1-12 and bulk. Experimental results are briefly discussed in the Sec. 6.2.1 of Sec. 6.2 and for the experimental setup and details, we refer to Ref. [11]. Theory results are explained more elaborately in the Sec. 6.2.2 of Sec. 6.2. A transition from direct to indirect bandgap is seen and the VBM changes from parabolic to inverted Mexican-hat shape when the thickness of crystal is less than 8 layers. Below, 8 layer thick ϵ-GaSe crystal excitonic signal in the transmission spectra is lost. We explain this suppression of excitonic signal with a simple analytical model and relate it to the change in the band structure. The experiments were carried out by Dr. Budweg and Dr. Brida of Prof. Leitenstorfer's group at University of Konstanz. We come up with one publication from this work [11] and this chapter up to large extent is taken from our published work [11].

6.1 Structure of GaSe

GaSe is a group III-VI semiconductor, forming crystals with a hexagonal layered structure. Individual layers consist of four atomic planes in a Se-Ga-Ga-Se order and interlayer bonding arises from weak vdW forces. In the ϵ-GaSe polytype the stacking follows an AB sequence, corresponding to the non-centrosymmetric space group D^1_{3h}[185, 186]. Thickness values between 0.8 and 1 nm are reported for a GaSe monolayer [187–189]. Fig.6.1 displays the crystal structure of a double layer of GaSe in (a) side and (b) top view, stacked according to the ϵ polytype. At room temperature, bulk GaSe exhibits a quasi-direct bandgap of approximately 2 eV. The VBM is at the Γ point, while the global CBM is positioned in proximity of the M point. However an almost isoenergetic local minimum exists at the Γ point, exceeding the M valley by only 10 meV [190]. The direct exciton with a binding energy of 19 meV is also located at the Γ point, in close energetic vicinity to the direct and indirect interband transitions [185, 191].

6.2 Results

6.2.1 Experiment

Fig. 6.2 depicts pump-probe measurements at different temperatures and as a function of the GaSe sample thickness. The blue-shift of the photon energy in Fig. 6.2(a) associated with the exciton

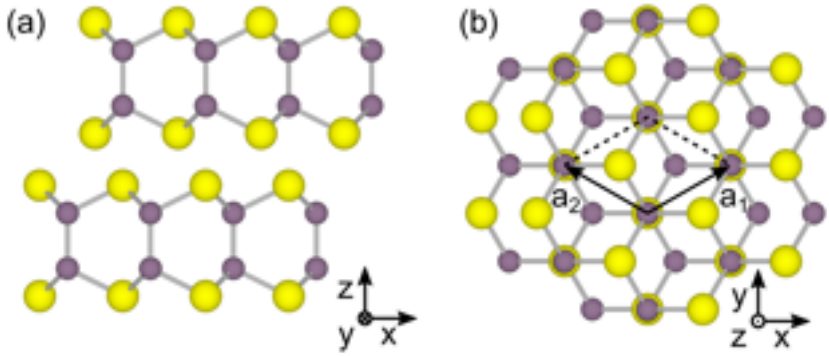

Figure 6.1: Schematic crystal structure of ϵ-GaSe viewed perpendicularly to the (a) y- and (b) z-axis. Yellow and violet spheres represent selenium and gallium atoms, respectively.

transition as extracted from these experiments. In detail the values are extracted from the pump-probe spectra by tracking the probe wavelength associated with the maximum signal in the differential transmission. Fig. 6.2(b) shows the magnitude of the excitonic signal as a function of the GaSe sample thickness. The dashed lines represent linear fits of the data points for thickness values up to 16 nm. It is clear that the excitonic signature vanishes for flakes thinner than 8 nm. Importantly, a significant residual signal cannot be hidden under the technical noise of the experiments, since the limit of the sensitivity is 10^{-5} (dotted black line in Fig. 6.2(b)).

A similar reduction in signal strength, as observed in our data, was recently reported for the photoluminescence of GaSe and attributed to rapid oxidation of thin flakes [192]. In contrast, we prevent oxidation of some samples by passivating them with a layer of Si_3N_4 right after exfoliation. Both sample sets, with and without passivation, display the vanishing signal at excitonic transitions, thus excluding oxidation as its origin. Instead, we tentatively attribute the observed behavior to a fundamental shaping of the valence band structure [193] in few-layer GaSe combined with substrate screening, as explained in the theory Sec. 6.2.2.

6.2.2 Theory

The band structure of single-layer GaSe has been calculated and studied thoroughly [193–197], and band calculations for few-layers have been performed both for the β-GaSe polytype [193] and the ϵ polytype [198]. For the ϵ-GaSe polytype, which is relevant for exfoliated samples [199], we perform ground state electronic structure calculations using DFT within LDA [62], as implemented in the open-source package QUANTUMESPRESSO [63]. We employ a PW basis set with a kinetic energy cutoff of 80 Ry and a charge-density cutoff of 320 Ry together with fully relativistic norm-conserving pseudopotentials [106]. For the bulk we use a Γ-centered $16 \times 16 \times 3$ $\mathbf{k}$-grid. Few-layer structures are calculated by keeping the distance between periodic images constant at 18 Å along the stacking direction [z-axis in Fig. 6.1(a)] and the BZ are sampled with a $12 \times 12 \times 1$ $\mathbf{k}$-grid centered at the Γ point. Geometries are subsequently optimized by using the Broyden-Fletcher-Goldfarb-Shanno algorithm until the net force on atoms is less than 10^{-4} N Ry/a.u. and the total energy change is below 10^{-6} N Ry, where N is the number of GaSe layers in our supercell. We consider SOC in the band structure calculations but omit it in geometry optimizations, since it does not play a major role in that step.

The evolution of the highest valence band (HVB) and the lowest conduction band (LCB) is shown in Fig. 6.3(a). Since splitting of the bands around the Γ point is small, only one spinor-component is

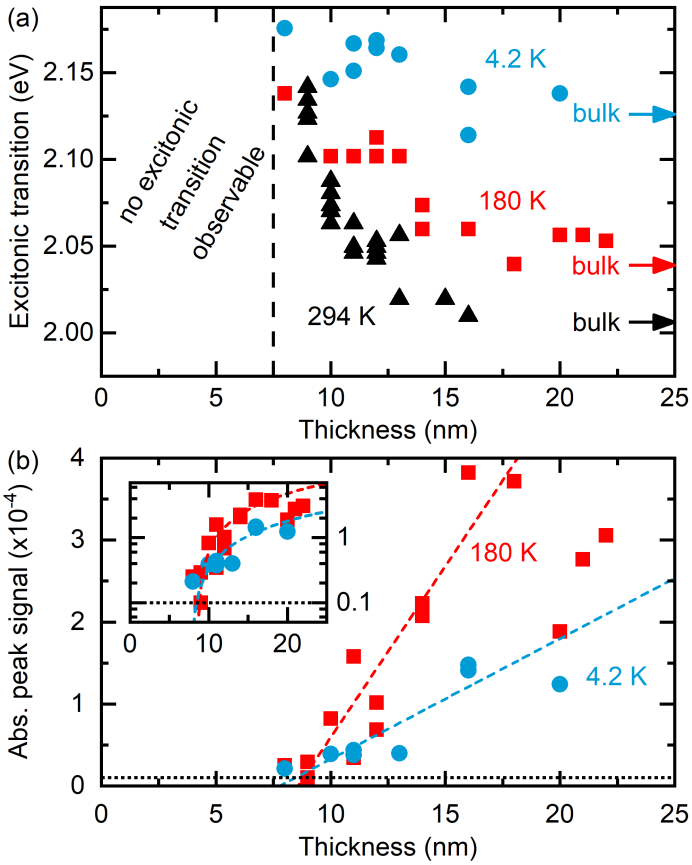

Figure 6.2: Measured energy position (a) and signal strength (b) of the maximum transmission change after optical excitation for different GaSe areas with thicknesses ranging from 8 to 25 nm and at temperatures of 4.2 K (blue circles), 180 K (red squares) and 294 K (black triangles). The arrows in panel (a) mark the energy of the exciton transition in bulk samples for each temperature. In panel (b), the dashed lines represent linear fits of the data points while the inset shows the same information on a logarithmic scale. The dotted line represents the noise level of the experiments.

displayed. Similar to previous reports [193, 198], our calculations show that the HVB evolves from a parabolic shape to an inverted Mexican hat by reducing the number of layers. In this process, the effective mass of the holes changes from positive to negative at the Γ point. This transition occurs at the critical value of 8 layers, where the HVB is approximately flat around the center of the BZ. In contrast to the HVB, the curvature of the LCB is qualitatively unaffected by the GaSe thickness, exhibiting a parabolic shape equivalent to a positive effective mass of the electrons. As shown in Fig. 6.3(b), the gap between the LCB and HVB at the Γ point increases with decreasing layer thickness, as expected from quantum confinement effects due to dimensionality reduction.

We investigate further the absorption spectra of the layers by computing the complex dielectric function $\epsilon(E) = \epsilon_1(E) + i\epsilon_2(E)$ within the RPA using QUANTUMESPRESSO [63]. While we neglect excitonic effects in this approach, we concentrate on vertical transitions within the single-particle band structure, leading to non-interacting electron-hole pairs. The complex dielectric function $\epsilon_2(E)$ is defined as

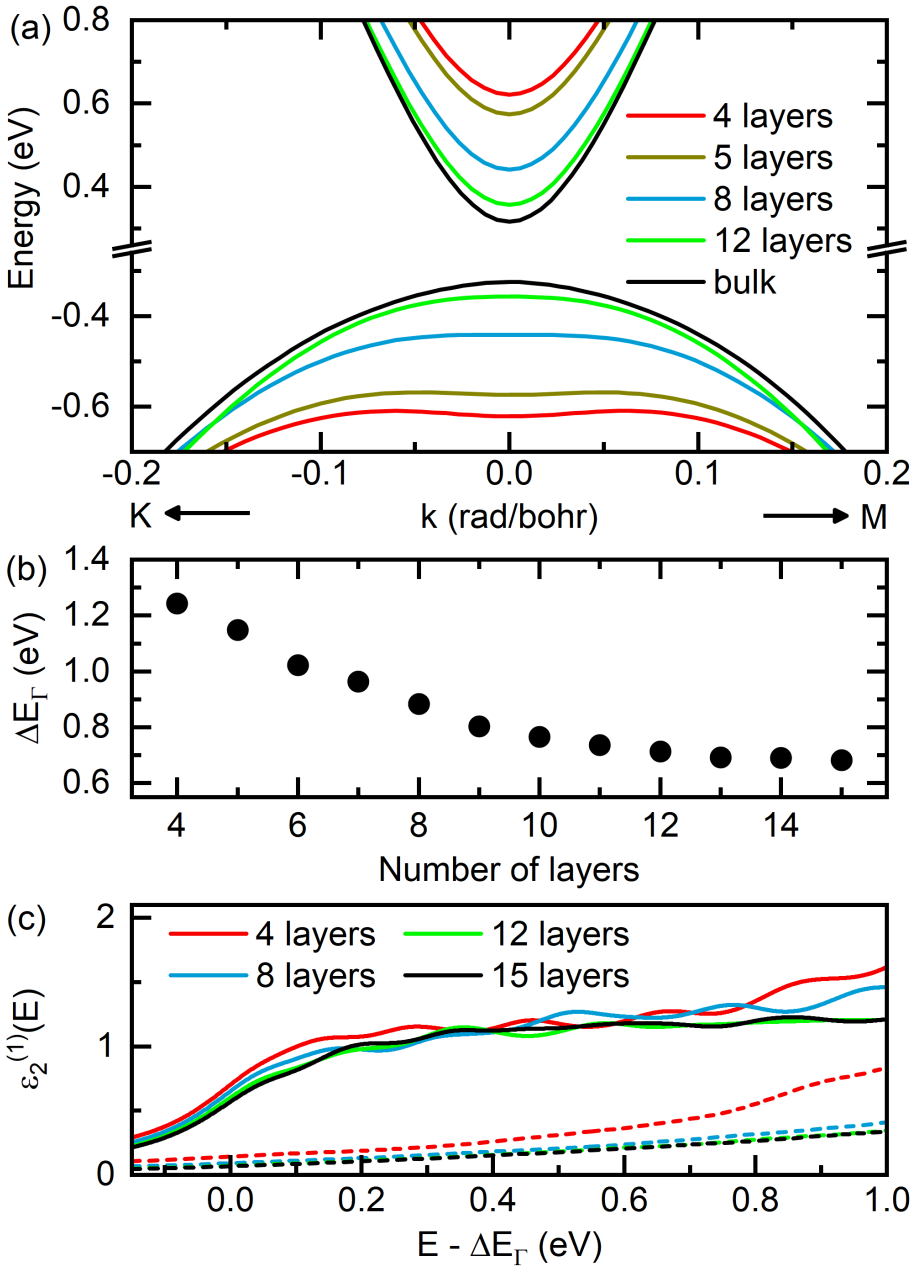

Figure 6.3: (a) Evolution of HVB and LCB with increasing number of layers for the ϵ-GaSe polytype. (b) Change of the DFT bandgap at the Γ point. (c) Absorption spectra of 4, 8, 12 and 15 layers calculated within RPA as a function of the photon energy. The spectra are plotted relative to the bandgap at the Γ point and are normalized to a single-layer, as described in the text. Solid lines show $\epsilon_2^1(E)$, if the light is polarized out-of-plane [$\epsilon_{2,zz}^1(E)$], dashed lines are for the in-plane direction [$\epsilon_{2,xx}^1(E) = \epsilon_{2,yy}^1(E)$, see Fig. 6.1].

$$\epsilon_{2\alpha,\beta}(E) = 1 - \frac{4\pi}{\Omega N_{\mathbf{k}}} \sum_{n\mathbf{k}} \frac{df(\varepsilon_{n\mathbf{k}})}{d\varepsilon_{n\mathbf{k}}} \frac{M_{\alpha,\beta}}{E^2 + i\eta E} + \frac{8\pi}{\Omega N_{\mathbf{k}}} \sum_{\substack{n\neq n' \\ \mathbf{k}}} \frac{f(\varepsilon_{n\mathbf{k}})}{(\varepsilon_{n'\mathbf{k}} - \varepsilon_{n\mathbf{k}})^2 + E^2 + i\Lambda E} \frac{M_{\alpha,\beta}}{\varepsilon_{n'\mathbf{k}} - \varepsilon_{n\mathbf{k}}}, \tag{6.1}$$

where α, β = x, y and, z. Λ, η are the intersmearing and intrasmearing respectively and $N_{\mathbf{k}}$ are the number of $\mathbf{k}$-points. The momentum transition matrix elements $M_{\alpha,\beta}$ is written in terms of single particle Bloch function $u_{n\mathbf{k}}$ and momentum operator $\mathbf{p}$ is written as

$$M_{\alpha,\beta} = \langle u_{n'\mathbf{k}}|p_\alpha|u_{n\mathbf{k}}\rangle\langle u_{n\mathbf{k}}|p^\dagger_\beta|u_{n'\mathbf{k}}\rangle. \tag{6.2}$$

We find that without SOC transitions from the HVB to the LCB at the Γ point are strictly forbidden in all structures of the ϵ-GaSe polytype independent of layer thickness, if the light is polarized in-plane. Selection rules are changed, however, with the inclusion of SOC, making such transitions weakly allowed, as has been pointed out for the bulk and single-layer cases [185, 200]. We note that stacks with even layer numbers possess point-group symmetry C_{3v}, while those with an odd number are of D_{3h} symmetry. In the RPA calculations we use a $50 \times 50 \times 1$ $\mathbf{k}$-grid to obtain the in-plane (straight lines) and out-of-plane (dashed lines) components of the imaginary part of the dielectric function, as depicted in Fig. 6.3(c), which is proportional to the absorption coefficient.

The absorption spectra are normalized to a single-layer by plotting $\epsilon_2^{(1)}(E) = L\epsilon_2(E)/L_s$, where L_s is the thickness of the GaSe sample and L is the total thickness of the supercell perpendicular to the stack, thus also including the surrounding vacuum. Fig. 6.3(c) shows that, within our assumption of non-interacting electrons and holes, the absorption of the individual layers does not change significantly as the number of layers in the GaSe crystal is reduced and that it is stronger if the light is polarized out-of-plane. However, the strongly focused beams employed in the experiments access both in- and out-of-plane components of the absorption spectrum with negligible dependence of the differential transmission signal on the angle of incidence onto the samples.

Since qualitative changes of the absorption based on band structure effects can be excluded in a single-particle picture [see Fig. 6.3(c)], we now focus on the relation between the slab thickness d and many-body interactions as characterized by the ground-state exciton radius R_0. Assuming an anisotropic hydrogenic model for Wannier-Mott excitons [35], we can estimate the exciton radius as $R_0 = e^2/2\sqrt{\epsilon_\parallel \epsilon_\perp} E_0$. Using literature values [201] for the binding energy E_0 = 19.7 meV as well as for out-of-plane and in-plane dielectric constants $\epsilon_\parallel = 6.18$ and $\epsilon_\perp = 10.6$ respectively, we find R_0 = 4.5 nm in the bulk limit. Surprisingly, the corresponding exciton diameter of 9 nm is very close to the critical slab thickness, below which the excitonic signal disappears in the optical excitation measurements [See Fig. 6.2(b)]. Once $d \leq 2R_0$ the 3D exciton does not fit the out-of-plane dimension anymore and hence must be considered as a 2D entity. Apparently, this critical thickness corresponds to just above 8 layers, where the valence band acquires the inverted Mexican hat shape with the in-plane wave vector of the local band maxima $k_0 \approx 0.1\text{Å} - 1$ [see Fig. 6.1(a)]. Thus, the critical thickness of about 9 nm (i) leads to the suppression of the exciton absorption line, (ii) induces a valence band inversion, and (iii) separates the 2D and 3D regimes in the electron-hole relative motion. This suggests that phenomena (i)–(iii) should be interrelated.

The valence band inversion may indeed lead to qualitative changes in the electron-hole relative motion and exciton ground state. The radial wave vectors relevant for the excitonic ground state formation lie below $1/R_0$. Since $k_0 R_0 > 1$ in our case, both the valence and conduction bands are characterized by a positive curvature at the relevant momentum scale, yielding a configuration where both conduction and valence band states have positive group velocities. This contrasts with the GaSe monolayer limit in vacuum [197], where the binding energy is predicted to be about 660 meV, suggesting an excitonic radius at least one order of magnitude smaller than R_0 estimated from bulk parameters. Resulting in $k_0 R_0 > 1$, this condition allows for the existence of conventional but tightly bound excitonic states [202], since the valence band acquires the usual negative curvature at the scale of $1/R_0$, leading to a negative group velocity for the corresponding states. In real samples like ours this effect is however limited by the dielectric screening of the substrate. The energy shift of the main excitonic feature in [See Fig. 6.2] is due to the increasing energy gap between the CBM and VBM as

is qualitatively confirmed by the values calculated in Fig. 6.3(b), where the typical underestimation of the DFT bandgap has to be taken into account [64].

6.3 Summary

The thickness-controlled modulation of the optical properties provides attractive resources for the development of functional optoelectronic devices based on a single material. The discovery of this mechanism paves the way towards devices employing a single material with engineered band topology in a controlled environment, where the layer number determines the properties of light-matter interaction and complex adjacent functionalities can be integrated on a single chip.

Chapter 7

Summary and outlook

In this work, we presented the theoretical calculations for photocarrier thermalization in various 2D materials. We mainly looked at the carrier-phonon or EP scattering events by calculating the self-energy within the lowest-order of perturbation theory. We also studied layer dependent absorption in the GaSe.

In the Ch. 2 of this thesis, we provided the theoretical model used in the photocarrier thermalization. There, we started with the description of DFT based on Kohn-Sham equations, which we used to calculate the ground-state properties of the materials. We gave a brief derivation of lattice dynamics and introduced a relation for LO-TO correction term in polar materials at Γ-point. Next, we moved to self-energy derivation, considering EP interaction as a small perturbation. We used Matsubara Green's function formalism in the grand canonical ensemble. The grand canonical ensemble allowed us to take into account temperature in Green's function and hence in self-energy. We ended this chapter by describing the Boltzmann equation in steady state under RTA. In nutshell, we combined the DFT and many-body perturbation theory with Boltzmann equation to calculate the excitation energy and temperature dependent thermalization times of photoexcited carriers due to EP scattering. We explored the carrier dynamics namely in graphene, MoS_2, WSe_2 and, CdTe.

In the Ch. 3 of this thesis, we studied photocarrier thermalization in intrinsic graphene. We carried out calculations using *ab-initio* methods as described in Ch. 2 and supported our simulation's results by an explicitly solvable model. We found out that thermalization time varied from few hundred of ps to few ten of fs over a range of temperature and excitation energies. Within low-temperature and excitation energies (below optical phonon threshold), three order of magnitude change in thermalization time was explained by the thermalization bottleneck in graphene and role of acoustical phonons in thermalization was highlighted. The main outcome of this chapter was that at low-temperature and excitation energies, phonon absorption became a rare event and phonon emission would require empty states below Fermi-energy (which is already occupied). For these reasons, carriers thermalized by acoustical phonons and took much longer time as compared to optical phonons.

In the next Ch. 4, we explored photocarrier dynamics of MoS_2 and WSe_2. We investigated the effect of SOC and the role of optical and acoustical phonons on thermalization times. Without SOC at low-excitation energy (0.08 eV) carrier thermalization was dominated by acoustical phonons except for MoS_2 electrons. Whereas, at high excitation energy (0.8 eV), optical phonons were dominant at low-temperatures and acoustic phonons kicked in at a temperature greater than 100 K. On including SOC, the acoustical phonon contributions were strongly suppressed at low-temperature and excitation energies leaving optical contribution unaffected. For this reason, the thermalization of electrons and holes was governed by optical phonons only at low T. We found that the phonon bottleneck persisted even slightly above the highest phonon energy as long as low-temperature and excitation energies condition was full filled. The major changes in the thermalization times were seen around the band edges where the spin-splitting of the bands due to SOC was present. Based on tunneling time, we

anticipated that the devices based on WSe_2 would give more IQE than MoS_2.

Ch. 5 comprised a comparative study of the photocarrier thermalization, between the bulk and single-layer CdTe. Within the best of our knowledge, monolayer CdTe has not been synthesized in the lab yet. With the help of DFT, we envisioned the dynamical stability of four-layer-thick monolayer CdTe when cleaved along [110] facet of the bulk crystal. Though the calculated thermalization time of the hot carriers was much longer in the bulk as compared to the monolayer. However, we observed interesting phenomena in monolayer CdTe. Up to 0.5 eV of excitation energy, the thermalization time for holes changed slightly and for electrons it remained constant with increasing temperature and excitation energies. We associated this behaviour as a direct consequence of parabolic bands in the 2D limit.

In summary of the photocarrier thermalization, (i) we found the existence of a phonon bottleneck in graphene (ii) increase in the thermalization time due to the presence of strong SOC at the band edges in MoS_2 and WSe_2 and (iii) constant thermalization time for parabolic bands in the 2D limit in case of monolayer CdTe. We found our findings consistent with the current understanding of thermalization at reduced dimensionality.

The last chapter of this thesis covered the study of optical absorption of a few-layer ϵ-GaSe. At the sample thickness below 8 layers, the excitonic peak in the transmission spectra was suppressed. This feature, we related to the change in the shape of valence band maxima through analytical model and absorption calculations within RPA.

Let us close this section with a short outlook. We restricted ourselves to the low-excitation densities and energies where the EP scattering dominated. For a generalization of our approach, it would be important to include the carrier-carrier scattering in the model. We always studied the intrinsic materials, whereas in real samples, defects can not be avoided and they also provide additional channel for thermalization. It would be important to include the carrier-carrier and carrier-defect scattering to make the model applicable for higher excitation densities, energies and realistic samples. DFT underestimated the bandgap of materials in our studies, we used the scissor operator to make rigid shifts in the band gaps. This crude approximation can be avoided by using the GW method and using the correctly aligned the GW eigenvalues for the phonon calculations. This would correctly define the slopes of the phonon band structure and reduce the errors in the EP matrix elements.

List of publications

Regular articles

1. E. Linardy, D. Yadav, D. Vella, I. A. Verzhbitskiy, K. Watanabe, T. Taniguchi, F. Pauly, M.Trushin, and G. Eda, “Harnessing exciton-exciton annihilation in two-dimensional semiconductors”, Nano Letters (2020).

2. A. Budweg, D. Yadav, A. Grupp, A. Leitenstorfer, M. Trushin, F. Pauly, and D. Brida, “Controlof excitonic absorption by thickness variation in few-layer gase”, Phys. Rev. B **100**, 045404 (2019).

3. D. Yadav, M. Trushin, and F. Pauly, “Photocarrier thermalization bottleneck in graphene”, Phys. Rev. B **99**, 155410 (2019).

Under review

1. D. Yadav, M. Trushin, and F. Pauly, “Thermalization of photoexcited carriers in two-dimensional transition metal dichalcogenides and internal quantum efficiency of van der waals heterostructures”, arXiv:1910.05216.

2. D. Yadav, F. Pauly, and M. Trushin, “Charge carrier thermalization in bulk and monolayer CdTe:a first principles study”, arXiv:1910.05216.

Manuscripts under preparation

1. S. Borah, D. Yadav, M. Trushin, and F. Pauly, "Electron-phonon assisted carrier cooling in bilayer graphene and hBN/graphene Van der Waals heterostructures".

Abbreviations

2D	Two-dimensional
BZ	Brillouin zone
CBM	conduction band minima
DFPT	Density functional perturbation theory
DFT	Density functional theory
DOS	Density of state
EP	Electron-phonon
HVB	Highest valence band
IFC	Interatomic force constant
IQE	Internal quantum efficiency
LDA	Local density approximation
LO	Longitudinal optical
LCB	Lowest conduction band
MOSFET	Metal-oxide-semiconductor field-effect transistors
PV	Photovoltaic
PW	Plane-wave
RPA	Random phase approximation
RTA	Relaxation time approximation
SOC	Spin-orbit coupling
TMDCs	Transition metal dichalcogenides
TO	Transverse optical
vdW	Van der Waals
VBM	valence band maximum
WF	Wannier function

Chapter 8

Acknowledgment

First of all, I thank to Prof. Pauly for providing me an opportunity to pursue my PhD in his "Quantum Transport and Electronic Structure Theory" group. We started this adventure almost 5 years ago together at University of Konstanz, exploring the photocarrier dynamics in 2D materials. I also got an opportunity through Prof. Pauly to travel to a beautiful place Okinawa Institute of Science and Technology (OIST), Japan. I extend my decisive thanks to Dr. Trushin for making my PhD journey interesting and providing constant support at the physics end. Their constant positive encouragement, helped me a lot to make my PhD possible. On the financial side, I thank to Carl Zeiss Foundation, the Collaborative Research Center (SFB) of the German Research Foundation (DFG) and OIST.

I also acknowledge Prof. Brida, Prof. Goki, Dr. Budweg and Eric for the fruitful collaborations on the various projects that I did with them. They helped me to gauge the application side of my theoretical works and to get more insights on the power and limitations of the theory.

I am grateful to Dr. Gerlach, admin of the Scientific Computing Cluster (SCC) at Konstanz for installing the softwares and packages needed. It helped me to run test calculations at initial stages of my work. I can't thank more to the computational facilities and team of SANGO at OIST and the bwHPC program, namely the JUSTUS HPC facility of the bwUniCluster for providing the resources to complete the simulations at the final stages.

I thank to my colleagues, Simon and Maxim for discussions on the scientific and technical aspects of our research work. In the end, I would like to thank Ms. Lucas, Ms. Dutt and team from the Welcome center in Konstanz to make my life easy with the paper and bureaucratic work in and out of University.

References

[1] F. Schwierz, "Graphene transistors", Nat. Nanotechnol. **5**, 487 (2010) (cit. on p. 1).

[2] A. Louwen, W. van Sark, R. Schropp, and A. Faaij, "A cost roadmap for silicon heterojunction solar cells", Sol. Energy Mater. Sol. Cells **147**, 295 (2016) (cit. on p. 1).

[3] M. A. Green, E. D. Dunlop, D. H. Levi, J. Hohl-Ebinger, M. Yoshita, and A. W. Ho-Baillie, "Solar cell efficiency tables (version 54)", Progress in Photovoltaics: Research and Applications **27**, 565 (2019) (cit. on pp. 1, 51).

[4] J. Shah, *Front matter* (Academic Press, San Diego, 1992) (cit. on p. 2).

[5] P. Würfel, "Solar energy conversion with hot electrons from impact ionisation", Sol. Energy Mater. Sol. Cells **46**, 43 (1997) (cit. on p. 2).

[6] B. K. Ridley, "Hot electrons in low-dimensional structures", Rep. Prog. Phys. **54**, 169 (1991) (cit. on pp. 2 sq., 52, 58).

[7] W. A. Tisdale, K. J. Williams, B. A. Timp, D. J. Norris, E. S. Aydil, and X.-Y. Zhu, "Hot-electron transfer from semiconductor nanocrystals", Science **328**, 1543 (2010) (cit. on pp. 2, 40, 58).

[8] K. S. Novoselov, A. K. Geim, S. V. Morozov, D. Jiang, Y. Zhang, S. V. Dubonos, I. V. Grigorieva, and A. A. Firsov, "Electric field effect in atomically thin carbon films", Science **306**, 666 (2004) (cit. on pp. 2 sq., 52).

[9] Y. Cao, A. Mishchenko, G. L. Yu, E. Khestanova, A. P. Rooney, E. Prestat, A. V. Kretinin, P. Blake, M. B. Shalom, C. Woods, J. Chapman, G. Balakrishnan, I. V. Grigorieva, K. S. Novoselov, B. A. Piot, M. Potemski, K. Watanabe, T. Taniguchi, S. J. Haigh, A. K. Geim, and R. V. Gorbachev, "Quality heterostructures from two-dimensional crystals unstable in air by their assembly in inert atmosphere", Nano Lett. **15**, 4914 (2015) (cit. on p. 2).

[10] K. F. Mak, C. Lee, J. Hone, J. Shan, and T. F. Heinz, "Atomically thin MoS_2: a new direct-gap semiconductor", Phys. Rev. Lett. **105**, 136805 (2010) (cit. on pp. 2, 52).

[11] A. Budweg, D. Yadav, A. Grupp, A. Leitenstorfer, M. Trushin, F. Pauly, and D. Brida, "Control of excitonic absorption by thickness variation in few-layer gase", Phys. Rev. B **100**, 045404 (2019) (cit. on pp. 2, 52, 59).

[12] A. Fleurence, R. Friedlein, T. Ozaki, H. Kawai, Y. Wang, and Y. Yamada-Takamura, "Experimental evidence for epitaxial silicene on diboride thin films", Phys. Rev. Lett. **108**, 245501 (2012) (cit. on p. 2).

[13] P. Vogt, P. De Padova, C. Quaresima, J. Avila, E. Frantzeskakis, M. C. Asensio, A. Resta, B. Ealet, and G. Le Lay, "Silicene: compelling experimental evidence for graphenelike two-dimensional silicon", Phys. Rev. Lett. **108**, 155501 (2012) (cit. on p. 2).

[14] D. Kong, W. Dang, J. J. Cha, H. Li, S. Meister, H. Peng, Z. Liu, and Y. Cui, "Few-layer nanoplates of bi2se3 and bi2te3 with highly tunable chemical potential", Nano Lett. **10**, 2245 (2010) (cit. on p. 2).

[15] Y. Shi, W. Zhou, A.-Y. Lu, W. Fang, Y.-H. Lee, A. L. Hsu, S. M. Kim, K. K. Kim, H. Y. Yang, L.-J. Li, J.-C. Idrobo, and J. Kong, "Van der waals epitaxy of mos2 layers using graphene as growth templates", Nano Lett. **12**, 2784 (2012) (cit. on p. 2).

[16] A. Ismach, H. Chou, D. A. Ferrer, Y. Wu, S. McDonnell, H. C. Floresca, A. Covacevich, C. Pope, R. Piner, M. J. Kim, R. M. Wallace, L. Colombo, and R. S. Ruoff, "Toward the controlled synthesis of hexagonal boron nitride films", ACS Nano **6**, 6378 (2012) (cit. on p. 2).

[17] C. Li, L. Huang, G. P. Snigdha, Y. Yu, and L. Cao, "Role of boundary layer diffusion in vapor deposition growth of chalcogenide nanosheets: the case of ges", ACS Nano **6**, 8868 (2012) (cit. on p. 2).

[18] J. Kim, L. J. Cote, F. Kim, and J. Huang, "Visualizing graphene based sheets by fluorescence quenching microscopy", J. Am. Chem. Soc. **132**, 260 (2010) (cit. on p. 2).

[19] D. Teweldebrhan, V. Goyal, and A. A. Balandin, "Exfoliation and characterization of bismuth telluride atomic quintuples and quasi-two-dimensional crystals", Nano Lett. **10**, 1209 (2010) (cit. on p. 2).

[20] H. R. Gutiérrez, N. Perea-López, A. L. Elías, A. Berkdemir, B. Wang, R. Lv, F. López-Urías, V. H. Crespi, H. Terrones, and M. Terrones, "Extraordinary room-temperature photoluminescence in triangular ws2 monolayers", Nano Lett. **13**, 3447 (2013) (cit. on p. 2).

[21] K. Fukuda, K. Akatsuka, Y. Ebina, R. Ma, K. Takada, I. Nakai, and T. Sasaki, "Exfoliated nanosheet crystallite of cesium tungstate with 2d pyrochlore structure: synthesis, characterization, and photochromic properties", ACS Nano **2**, 1689 (2008) (cit. on p. 2).

[22] M. A. Bizeto, A. L. Shiguihara, and V. R. L. Constantino, "Layered niobate nanosheets: building blocks for advanced materials assembly", J. Mater. Chem. **19**, 2512 (2009) (cit. on p. 2).

[23] P. Nemes-Incze, Z. Osváth, K. Kamarás, and L. Biró, "Anomalies in thickness measurements of graphene and few layer graphite crystals by tapping mode atomic force microscopy", Carbon **46**, 1435 (2008) (cit. on p. 2).

[24] A. K. Geim and I. V. Grigorieva, "Van der waals heterostructures", Nature **499**, 419 (2013) (cit. on p. 2).

[25] A. H. Castro Neto, F. Guinea, N. M. R. Peres, K. S. Novoselov, and A. K. Geim, "The electronic properties of graphene", Rev. Mod. Phys. **81**, 109 (2009) (cit. on p. 2).

[26] J.-H. Chen, C. Jang, S. Xiao, M. Ishigami, and M. S. Fuhrer, "Intrinsic and extrinsic performance limits of graphene devices on SiO_2", Nat. Nanotechnol. **3**, 206 (2008) (cit. on p. 2).

[27] Y.-M. Lin, C. Dimitrakopoulos, K. A. Jenkins, D. B. Farmer, H.-Y. Chiu, A. Grill, and P. Avouris, "100-ghz transistors from wafer-scale epitaxial graphene", Science **327**, 662 (2010) (cit. on p. 2).

[28] A. Splendiani, L. Sun, Y. Zhang, T. Li, J. Kim, C.-Y. Chim, G. Galli, and F. Wang, "Emerging photoluminescence in monolayer mos2", Nano Lett. **10**, 1271 (2010) (cit. on p. 2).

[29] G. Eda, H. Yamaguchi, D. Voiry, T. Fujita, M. Chen, and M. Chhowalla, "Photoluminescence from chemically exfoliated MoS_2", Nano Lett. **11**, 5111 (2011) (cit. on pp. 2, 52).

[30] Q. Wang, S. Ge, X. Li, J. Qiu, Y. Ji, J. Feng, and D. Sun, "Valley carrier dynamics in monolayer molybdenum disulfide from helicity-resolved ultrafast pump-probe spectroscopy", ACS Nano **7**, 11087 (2013) (cit. on pp. 2, 40).

[31] D. Lagarde, L. Bouet, X. Marie, C. R. Zhu, B. L. Liu, T. Amand, P. H. Tan, and B. Urbaszek, "Carrier and polarization dynamics in monolayer MoS_2", Phys. Rev. Lett. **112**, 047401 (2014) (cit. on pp. 2, 40).

[32] B. Radisavljevic, A. Radenovic, J. Brivio, V. Giacometti, and A. Kis, "Single-layer MoS_2 transistors", Nat. Nanotechnol. **6**, 147 (2011) (cit. on p. 2).

[33] D. Lembke and A. Kis, "Breakdown of high-performance monolayer mos2 transistors", ACS Nano **6**, 10070 (2012) (cit. on p. 2).

[34] S. Bertolazzi, D. Krasnozhon, and A. Kis, "Nonvolatile memory cells based on mos2/graphene heterostructures", ACS Nano **7**, 3246 (2013) (cit. on p. 2).

[35] F. Bonaccorso, Z. Sun, T. Hasan, and A. C. Ferrari, "Graphene photonics and optoelectronics", Nat. Photonics **4**, 611 (2010) (cit. on pp. 2, 52).

[36] S. Bae, H. Kim, Y. Lee, X. Xu, J.-S. Park, Y. Zheng, J. Balakrishnan, T. Lei, H. Ri Kim, Y. I. Song, Y.-J. Kim, K. S. Kim, B. Özyilmaz, J.-H. Ahn, B. H. Hong, and S. Iijima, "Roll-to-roll production of 30-inch graphene films for transparent electrodes", Nat. Nanotechnol. **5**, 574 (2010) (cit. on p. 3).

[37] E. P. Randviir, D. A. Brownson, and C. E. Banks, "A decade of graphene research: production, applications and outlook", Mater. Today **17**, 426 (2014) (cit. on p. 3).

[38] W. Choi, N. Choudhary, G. H. Han, J. Park, D. Akinwande, and Y. H. Lee, "Recent development of two-dimensional transition metal dichalcogenides and their applications", Mater. Today **20**, 116 (2017) (cit. on p. 3).

[39] A. Leitenstorfer, C. Fürst, A. Laubereau, W. Kaiser, G. Tränkle, and G. Weimann, "Femtosecond carrier dynamics in gaas far from equilibrium", Phys. Rev. Lett. **76**, 1545 (1996) (cit. on p. 3).

[40] C. J. Ciccarino, T. Christensen, R. Sundararaman, and P. Narang, "Dynamics and spin-valley locking effects in monolayer transition metal dichalcogenides", Nano Lett. **18**, 5709 (2018) (cit. on pp. 3, 40, 47, 52).

[41] M. Bernardi, D. Vigil-Fowler, J. Lischner, J. B. Neaton, and S. G. Louie, "*Ab initio* study of hot carriers in the first picosecond after sunlight absorption in silicon", Phys. Rev. Lett. **112**, 257402 (2014) (cit. on pp. 3, 40, 52).

[42] M. Bernardi, D. Vigil-Fowler, C. S. Ong, J. B. Neaton, and S. G. Louie, "Ab initio study of hot electrons in GaAs", Proc. Natl. Acad. Sci. U. S. A. **112**, 5291 (2015) (cit. on pp. 3, 52).

[43] F. Bloch, "Über die quantenmechanik der elektronen in kristallgittern", Z.Physik **52**, 555 (1929) (cit. on p. 3).

[44] L. Nordheim, "Zur elektronentheorie der metalle. i", Ann. Phys. (Berlin) **401**, 607 (1931) (cit. on p. 3).

[45] J. Bardeen, "Conductivity of monovalent metals", Phys. Rev. **52**, 688 (1937) (cit. on p. 3).

[46] J. Bardeen and W. Shockley, "Deformation potentials and mobilities in non-polar crystals", Phys. Rev. **80**, 72 (1950) (cit. on p. 3).

[47] W. Shockley and J. Bardeen, "Energy bands and mobilities in monatomic semiconductors", Phys. Rev. **77**, 407 (1950) (cit. on p. 3).

[48] H. Fröhlich, H. Pelzer, and S. Zienau, "Xx. properties of slow electrons in polar materials", Philos. Mag. Ser. **41**, 221 (1950) (cit. on p. 3).

[49] M. M. Dacorogna, M. L. Cohen, and P. K. Lam, "Self-consistent calculation of the q dependence of the electron-phonon coupling in aluminum", Phys. Rev. Lett. **55**, 837 (1985) (cit. on pp. 3, 17).

[50] M. V. Fischetti and S. E. Laux, "Monte carlo analysis of electron transport in small semiconductor devices including band-structure and space-charge effects", Phys. Rev. B **38**, 9721 (1988) (cit. on p. 3).

[51] J. C. W. Song, M. Y. Reizer, and L. S. Levitov, "Disorder-assisted electron-phonon scattering and cooling pathways in graphene", Phys. Rev. Lett. **109**, 106602 (2012) (cit. on pp. 3, 28).

[52] E. Mali ć, T. Winzer, and A. Knorr, "Efficient orientational carrier relaxation in optically excited graphene", Appl. Phys. Lett. **101**, 213110 (2012) (cit. on pp. 3, 28).

[53] A. Tomadin, D. Brida, G. Cerullo, A. C. Ferrari, and M. Polini, "Non-equilibrium dynamics of photoexcited electrons in graphene: collinear scattering, Auger processes, and the impact of screening", Phys. Rev. B **88**, 035430 (2013) (cit. on pp. 3, 28).

[54] S. G. Menabde, H. Cho, and N. Park, "Interface defect-assisted phonon scattering of hot carriers in graphene", Phys. Rev. B **96**, 075426 (2017) (cit. on pp. 3, 28).

[55] M. Calandra and F. Mauri, "Electron-phonon coupling and electron self-energy in electron-doped graphene: calculation of angular-resolved photoemission spectra", Phys. Rev. B **76**, 205411 (2007) (cit. on pp. 3, 28, 32).

[56] F. Giustino, M. L. Cohen, and S. G. Louie, "Electron-phonon interaction using Wannier functions", Phys. Rev. B **76**, 165108 (2007) (cit. on p. 3).

[57] P. Hohenberg and W. Kohn, "Inhomogeneous electron gas", Phys. Rev. **136**, B864–B871 (1964) (cit. on pp. 5 sq.).

[58] W. Kohn and L. J. Sham, "Self-consistent equations including exchange and correlation effects", Phys. Rev. **140**, A1133–A1138 (1965) (cit. on pp. 5, 7).

[59] G. D. Mahan, *Many-Particle Physics*, 2nd ed. (Plenum, 1993) (cit. on pp. 5, 12).

[60] G. Pizzi, A. Cepellotti, R. Sabatini, N. Marzari, and B. Kozinsky, "Aiida: automated interactive infrastructure and database for computational science", Computational Materials Science **111**, 218–230 (2016) (cit. on p. 5).

[61] S. Haastrup, M. Strange, M. Pandey, T. Deilmann, P. S. Schmidt, N. F. Hinsche, M. N. Gjerding, D. Torelli, P. M. Larsen, A. C. Riis-Jensen, J. Gath, K. W. Jacobsen, J. J. Mortensen, T. Olsen, and K. S. Thygesen, "The computational 2d materials database: high-throughput modeling and discovery of atomically thin crystals", 2D Materials **5**, 042002 (2018) (cit. on p. 5).

[62] J. P. Perdew and A. Zunger, "Self-interaction correction to density-functional approximations for many-electron systems", Phys. Rev. B **23**, 5048 (1981) (cit. on pp. 9, 60).

[63] P. Giannozzi, O. Andreussi, T. Brumme, O. Bunau, M. B. Nardelli, M. Calandra, R. Car, C. Cavazzoni, D. Ceresoli, M. Cococcioni, N. Colonna, I. Carnimeo, A. D. Corso, S. de Gironcoli, P. Delugas, R. A. DiStasio, A. Ferretti, A. Floris, G. Fratesi, G. Fugallo, R. Gebauer, U. Gerstmann, F. Giustino, T. Gorni, J. Jia, M. Kawamura, H.-Y. Ko, A. Kokalj, E. Küçükbenli, M. Lazzeri, M. Marsili, N. Marzari, F. Mauri, N. L. Nguyen, H.-V. Nguyen, A. Otero-de-la-Roza, L. Paulatto, S. Poncé, D. Rocca, R. Sabatini, B. Santra, M. Schlipf, A. P. Seitsonen, A. Smogunov, I. Timrov, T. Thonhauser, P. Umari, N. Vast, X. Wu, and S. Baroni, "Advanced

capabilities for materials modelling with quantum ESPRESSO", J. Phys.: Condens. Matter **29**, 465901 (2017) (cit. on pp. 9, 29, 53, 60 sq.).

[64] R. M. Martin, *Electronic structure: basic theory and practical methods* (Cambridge University Press, 2004) (cit. on pp. 9, 64).

[65] K. Capelle, "A bird's-eye view of density-functional theory", Brazilian Journal of Physics **36**, 1318 (2006) (cit. on p. 9).

[66] J. C. Cuevas and E. Scheer, *Molecular Electronics: An introduction to theory and experiment*, 2nd edition (World Scientific, 2017) (cit. on p. 9).

[67] M. L. Cohen and S. G. Louie, *Fundamentals of condensed matter physics*, 2nd ed. (Cambridge University Press, 2016) (cit. on p. 10).

[68] X. Gonze and C. Lee, "Dynamical matrices, born effective charges, dielectric permittivity tensors, and interatomic force constants from density-functional perturbation theory", Phys. Rev. B **55**, 10355 (1997) (cit. on p. 11).

[69] F. Han, *A modern course in the quantum theory of solids*, 2nd ed. (World Scientific Printers, 2013) (cit. on p. 12).

[70] F. Giustino, "Electron-phonon interactions from first principles", Rev. Mod. Phys. **89**, 015003 (2017) (cit. on pp. 12, 25, 28).

[71] R. Kubo, "The spin-wave theory of antiferromagnetics", Phys. Rev. **87**, 568 (1952) (cit. on p. 13).

[72] M. Lundstrom, *Fundamentals of carrier transport*, 2nd ed. (Cambridge University Press, 2000) (cit. on p. 24).

[73] S. Poncé, E. R. Margine, C. Verdi, and F. Giustino, "EPW: Electron-phonon coupling, transport and superconducting properties using maximally localized Wannier functions", Comput. Phys. Commun. **209**, 116 (2016) (cit. on pp. 25, 29, 42, 53).

[74] D. Yadav, M. Trushin, and F. Pauly, "Photocarrier thermalization bottleneck in graphene", Phys. Rev. B **99**, 155410 (2019) (cit. on pp. 27, 40, 52).

[75] J. Nelson, *The physics of solar cells* (Imperial College Press, London, 2003) (cit. on pp. 27, 39).

[76] K. S. Novoselov, A. Mishchenko, A. Carvalho, and A. H. Castro Neto, "2D materials and van der Waals heterostructures", Science **353**, aac9439 (2016) (cit. on pp. 27, 40).

[77] Q. Ma, T. I. Andersen, N. L. Nair, N. M. Gabor, M. Massicotte, C. H. Lui, A. F. Young, W. Fang, K. Watanabe, T. Taniguchi, J. Kong, N. Gedik, F. H. L. Koppens, and P. Jarillo-Herrero, "Tuning ultrafast electron thermalization pathways in a van der Waals heterostructure", Nat. Phys. **12**, 455 (2016) (cit. on pp. 27, 40, 42 sq., 58).

[78] M. T. Mihnev, F. Kadi, C. J. Divin, T. Winzer, S. Lee, C.-H. Liu, Z. Zhong, C. Berger, W. A. de Heer, E. Mali ć, A. Knorr, and T. B. Norris, "Microscopic origins of the terahertz carrier relaxation and cooling dynamics in graphene", Nat. Commun. **7**, 11617 (2016) (cit. on pp. 27 sq.).

[79] J. C. König-Otto, M. Mittendorff, T. Winzer, F. Kadi, E. Malic, A. Knorr, C. Berger, W. A. de Heer, A. Pashkin, H. Schneider, M. Helm, and S. Winnerl, "Slow noncollinear Coulomb scattering in the vicinity of the Dirac point in graphene", Phys. Rev. Lett. **117**, 087401 (2016) (cit. on pp. 27 sq., 40).

[80] D. M. Basko, S. Piscanec, and A. C. Ferrari, "Electron-electron interactions and doping dependence of the two-phonon Raman intensity in graphene", Phys. Rev. B **80**, 165413 (2009) (cit. on p. 28).

[81] M. Trushin, "Collinear scattering of photoexcited carriers in graphene", Phys. Rev. B **94**, 205306 (2016) (cit. on pp. 28 sq., 40).

[82] P. B. Allen, "Theory of thermal relaxation of electrons in metals", Phys. Rev. Lett. **59**, 1460 (1987) (cit. on p. 28).

[83] P. Maldonado, K. Carva, M. Flammer, and P. M. Oppeneer, "Theory of out-of-equilibrium ultrafast relaxation dynamics in metals", Phys. Rev. B **96**, 174439 (2017) (cit. on p. 28).

[84] S. Ono, "Thermalization in simple metals: role of electron-phonon and phonon-phonon scattering", Phys. Rev. B **97**, 054310 (2018) (cit. on p. 28).

[85] S. Sadasivam, M. K. Y. Chan, and P. Darancet, "Theory of thermal relaxation of electrons in semiconductors", Phys. Rev. Lett. **119**, 136602 (2017) (cit. on p. 28).

[86] D. Brida, A. Tomadin, C. Manzoni, Y. J. Kim, A. Lombardo, S. Milana, R. R. Nair, K. S. Novoselov, A. C. Ferrari, G. Cerullo, and M. Polini, "Ultrafast collinear scattering and carrier multiplication in graphene", Nat. Commun. **4**, 1987 (2013) (cit. on pp. 28, 37).

[87] M. Breusing, S. Kuehn, T. Winzer, E. Mali ć, F. Milde, N. Severin, J. P. Rabe, C. Ropers, A. Knorr, and T. Elsaesser, "Ultrafast non-equilibrium carrier dynamics in a single graphene layer", Phys. Rev. B **83**, 153410 (2011) (cit. on p. 28).

[88] C. H. Lui, K. F. Mak, J. Shan, and T. F. Heinz, "Ultrafast photoluminescence from graphene", Phys. Rev. Lett. **105**, 127404 (2010) (cit. on p. 28).

[89] J. Shang, T. Yu, J. Lin, and G. G. Gurzadyan, "Ultrafast electron-optical phonon scattering and quasiparticle lifetime in CVD-grown graphene", ACS Nano **5**, 3278 (2011) (cit. on p. 28).

[90] J. M. Dawlaty, S. Shivaraman, M. Chandrashekhar, F. Rana, and M. G. Spencer, "Measurement of ultrafast carrier dynamics in epitaxial graphene", Appl. Phys. Lett. **92**, 042116 (2008) (cit. on p. 28).

[91] J. C. Johannsen, S. Ulstrup, F. Cilento, A. Crepaldi, M. Zacchigna, C. Cacho, I. C. E. Turcu, E. Springate, F. Fromm, C. Raidel, T. Seyller, F. Parmigiani, M. Grioni, and P. Hofmann, "Direct view of hot carrier dynamics in graphene", Phys. Rev. Lett. **111**, 027403 (2013) (cit. on pp. 28, 37).

[92] I. Gierz, "Probing carrier dynamics in photo-excited graphene with time-resolved ARPES", J. Electron Spectrosc. Relat. Phenom. **219**, 53 (2017) (cit. on p. 28).

[93] S. Aeschlimann, R. Krause, M. Chávez-Cervantes, H. Bromberger, R. Jago, E. Malić, A. Al-Temimy, C. Coletti, A. Cavalleri, and I. Gierz, "Ultrafast momentum imaging of pseudospin-flip excitations in graphene", Phys. Rev. B **96**, 020301 (2017) (cit. on p. 28).

[94] M. Trushin, A. Grupp, G. Soavi, A. Budweg, D. De Fazio, U. Sassi, A. Lombardo, A. C. Ferrari, W. Belzig, A. Leitenstorfer, and D. Brida, "Ultrafast pseudospin dynamics in graphene", Phys. Rev. B **92**, 165429 (2015) (cit. on pp. 28, 33, 40).

[95] S. Winnerl, M. Orlita, P. Plochocka, P. Kossacki, M. Potemski, T. Winzer, E. Mali ć, A. Knorr, M. Sprinkle, C. Berger, W. A. de Heer, H. Schneider, and M. Helm, "Carrier relaxation in epitaxial graphene photoexcited near the Dirac point", Phys. Rev. Lett. **107**, 237401 (2011) (cit. on pp. 28, 33, 37).

[96] S. S. Kubakaddi, "Interaction of massless Dirac electrons with acoustic phonons in graphene at low temperatures", Phys. Rev. B **79**, 075417 (2009) (cit. on p. 28).

[97] R. Bistritzer and A. H. MacDonald, "Electronic cooling in graphene", Phys. Rev. Lett. **102**, 206410 (2009) (cit. on p. 28).

[98] W. K. Tse and S. DasSarma, "Energy relaxation of hot Dirac fermions in graphene", Phys. Rev. B **79**, 235406 (2009) (cit. on p. 28).

[99] T. Low, V. Perebeinos, R. Kim, M. Freitag, and P. Avouris, "Cooling of photoexcited carriers in graphene by internal and substrate phonons", Phys. Rev. B **86**, 045413 (2012) (cit. on pp. 28, 35–37).

[100] E. Mali ć, T. Winzer, E. Bobkin, and A. Knorr, "Microscopic theory of absorption and ultrafast many-particle kinetics in graphene", Phys. Rev. B **84**, 205406 (2011) (cit. on pp. 28, 31).

[101] R. Kim, V. Perebeinos, and P. Avouris, "Relaxation of optically excited carriers in graphene", Phys. Rev. B **84**, 075449 (2011) (cit. on p. 28).

[102] C.-H. Park, F. Giustino, C. D. Spataru, M. L. Cohen, and S. G. Louie, "First-principles study of electron linewidths in graphene", Phys. Rev. Lett. **102**, 076803 (2009) (cit. on p. 28).

[103] C. Ferrante, A. Virga, L. Benfatto, M. Martinati, D. De Fazio, U. Sassi, C. Fasolato, A. K. Ott, P. Postorino, D. Yoon, G. Cerullo, F. Mauri, A. C. Ferrari, and T. Scopigno, "Raman spectroscopy of graphene under ultrafast laser excitation", Nat. Commun. **9**, 308 (2018) (cit. on p. 28).

[104] S. Wu, W.-T. Liu, X. Liang, P. J. Schuck, F. Wang, Y. R. Shen, and M. Salmeron, "Hot phonon dynamics in graphene", Nano Lett. **12**, 5495 (2012) (cit. on p. 28).

[105] K. V. Zakharchenko, A. Fasolino, J. H. Los, and M. I. Katsnelson, "Melting of graphene: from two to one dimension", J. Phys.: Condens. Matter **23**, 202202 (2011) (cit. on pp. 28, 34).

[106] N. Troullier and J. L. Martins, "Efficient pseudopotentials for plane-wave calculations", Phys. Rev. B **43**, 1993 (1991) (cit. on pp. 29, 41, 53, 60).

[107] J.-A. Yan, W. Y. Ruan, and M. Y. Chou, "Phonon dispersions and vibrational properties of monolayer, bilayer, and trilayer graphene: density-functional perturbation theory", Phys. Rev. B **77**, 125401 (2008) (cit. on p. 29).

[108] S. Baroni, S. de Gironcoli, A. D. Corso, and P. Giannozzi, "Phonons and related crystal properties from density-functional perturbation theory", Rev. Mod. Phys. **73**, 515 (2001) (cit. on pp. 29, 53).

[109] N. Marzari, A. A. Mostofi, J. R. Yates, I. Souza, and D. Vanderbilt, "Maximally localized Wannier functions: theory and applications", Rev. Mod. Phys. **84**, 1419 (2012) (cit. on pp. 29, 42).

[110] S. Piscanec, M. Lazzeri, F. Mauri, A. C. Ferrari, and J. Robertson, "Kohn anomalies and electron-phonon interactions in graphite", Phys. Rev. Lett. **93**, 185503 (2004) (cit. on p. 32).

[111] M. Lazzeri, C. Attaccalite, L. Wirtz, and F. Mauri, "Impact of the electron-electron correlation on phonon dispersion: failure of LDA and GGA DFT functionals in graphene and graphite", Phys. Rev. B **78**, 081406 (2008) (cit. on p. 37).

[112] W. Zhang, C.-P. Chuu, J.-K. Huang, C.-H. Chen, M.-L. Tsai, Y.-H. Chang, C.-T. Liang, Y.-Z. Chen, Y.-L. Chueh, J.-H. He, M.-Y. Chou, and L.-J. Li, "Ultrahigh-gain photodetectors based on atomically thin graphene-MoS_2 heterostructures", Sci. Rep. **4**, 3826 (2014) (cit. on p. 37).

[113] D. De Fazio, I. Goykhman, D. Yoon, M. Bruna, A. Eiden, S. Milana, U. Sassi, M. Barbone, D. Dumcenco, K. Marinov, A. Kis, and A. C. Ferrari, "High responsivity, large-area graphene/MoS_2 flexible photodetectors", ACS Nano **10**, 8252 (2016) (cit. on p. 37).

[114] M. Massicotte, P. Schmidt, F. Vialla, K. Watanabe, T. Taniguchi, K.-J. Tielrooij, and F. H. Koppens, "Photo-thermionic effect in vertical graphene heterostructures", Nat. Commun. **7**, 12174 (2016) (cit. on p. 37).

[115] M. Trushin, "Theory of photoexcited and thermionic emission across a two-dimensional graphene-semiconductor Schottky junction", Phys. Rev. B **97**, 195447 (2018) (cit. on p. 37).

[116] D. Yadav, M. Trushin, and F. Pauly, "Thermalization of photoexcited carriers in two-dimensional transition metal dichalcogenides and internal quantum efficiency of van der waals heterostructures", arXiv:1910.05216 (cit. on p. 39).

[117] C. Clavero, "Plasmon-induced hot-electron generation at nanoparticle/metal-oxide interfaces for photovoltaic and photocatalytic devices", Nat. Photon. **8**, 95 (2014) (cit. on p. 39).

[118] H. Kawai, G. Giorgi, A. Marini, and K. Yamashita, "The mechanism of slow hot-hole cooling in lead-iodide perovskite: first-principles calculation on carrier lifetime from electron–phonon interaction", Nano Lett. **15**, 3103 (2015) (cit. on p. 40).

[119] H.-H. Fang, S. Adjokatse, S. Shao, J. Even, and M. A. Loi, "Long-lived hot-carrier light emission and large blue shift in formamidinium tin triiodide perovskites", Nat. Commun. **9**, 243 (2018) (cit. on p. 40).

[120] M. Mittendorff, T. Winzer, E. Malic, A. Knorr, C. Berger, W. A. de Heer, H. Schneider, M. Helm, and S. Winnerl, "Anisotropy of excitation and relaxation of photogenerated charge carriers in graphene", Nano Lett. **14**, 1504 (2014) (cit. on p. 40).

[121] F. Kadi, T. Winzer, A. Knorr, and E. Malic, "Impact of doping on the carrier dynamics in graphene", Sci. Rep. **5**, 16841 (2015) (cit. on p. 40).

[122] S. Z. Butler, S. M. Hollen, L. Cao, Y. Cui, J. A. Gupta, H. R. Guti érrez, T. F. Heinz, S. S. Hong, J. Huang, A. F. Ismach, E. Johnston-Halperin, M. K., V. V. Plashnitsa, R. D. Robinson, R. S. Ruoff, S. Salahuddin, J. Shan, L. Shi, M. G. Spencer, M. Terrones, W. Windl, and J. E. Goldberger, "Progress, challenges, and opportunities in two-dimensional materials beyond graphene", ACS Nano **7**, 2898 (2013) (cit. on p. 40).

[123] S. Das, J. A. Robinson, M. Dubey, H. Terrones, and M. Terrones, "Beyond graphene: progress in novel two-dimensional materials and van der Waals solids", Annu. Rev. Mater. Res. **45**, 1 (2015) (cit. on p. 40).

[124] Q. H. Wang, K. Kalantar-Zadeh, A. Kis, J. N. Coleman, and M. S. Strano, "Electronics and optoelectronics of two-dimensional transition metal dichalcogenides", Nat. Nanotechnol. **7**, 699 (2012) (cit. on pp. 40, 52).

[125] E. N. Voronina, L. S. Novikov, and T. V. Rakhimova, "Properties and potential applications of quasi-two-dimensional molybdenum disulfide for nanoelectronic elements", Inorg. Mater. Appl. Res. **9**, 175 (2018) (cit. on p. 40).

[126] M. M. Furchi, A. Pospischil, F. Libisch, J. Burgdörfer, and T. Mueller, "Photovoltaic effect in an electrically tunable van der Waals heterojunction", Nano Lett. **14**, 4785 (2014) (cit. on p. 40).

[127] L. Britnell, R. M. Ribeiro, A. Eckmann, R. Jalil, B. D. Belle, A. Mishchenko, Y.-J. Kim, R. V. Gorbachev, T. Georgiou, S. V. Morozov, A. N. Grigorenko, A. K. Geim, C. Casiraghi, A. H. C. Neto, and K. S. Novoselov, "Strong light-matter interactions in heterostructures of atomically thin films", Science **340**, 1311 (2013) (cit. on p. 40).

[128] W. J. Yu, Y. Liu, H. Zhou, A. Yin, Z. Li, Y. Huang, and X. Duan, "Highly efficient gate-tunable photocurrent generation in vertical heterostructures of layered materials", Nat. Nanotechnol. **8**, 952 (2013) (cit. on p. 40).

[129] Q. A. Vu, J. H. Lee, V. L. Nguyen, Y. S. Shin, S. C. Lim, K. Lee, J. Heo, S. Park, K. Kim, Y. H. Lee, and W. J. Yu, "Tuning carrier tunneling in van der Waals heterostructures for ultrahigh detectivity", Nano Lett. **17**, 453 (2017) (cit. on p. 40).

[130] S. Wang, J. Wang, W. Zhao, F. Giustiniano, L. Chu, I. Verzhbitskiy, J. Z. Yong, and G. Eda, "Efficient carrier-to-exciton conversion in field emission tunnel diodes based on MIS-type van der Waals heterostack", Nano Lett. **17**, 5156 (2017) (cit. on p. 40).

[131] Z. Nie, R. Long, L. Sun, C.-C. Huang, J. Zhang, Q. Xiong, D. W. Hewak, Z. Shen, O. V. Prezhdo, and Z.-H. Loh, "Ultrafast carrier thermalization and cooling dynamics in few-layer MoS_2", ACS Nano **8**, 10931 (2014) (cit. on pp. 40, 47, 50).

[132] H. Shi, R. Yan, S. Bertolazzi, J. Brivio, B. Gao, A. Kis, D. Jena, H. G. Xing, and L. Huang, "Exciton dynamics in suspended monolayer and few-layer MoS_2 2D crystals", ACS Nano **7**, 1072 (2013) (cit. on pp. 40, 48).

[133] D. Sun, Y. Rao, G. A. Reider, G. Chen, Y. You, L. Brézin, A. R. Harutyunyan, and T. F. Heinz, "Observation of rapid exciton-exciton annihilation in monolayer molybdenum disulfide", Nano Lett. **14**, 5625 (2014) (cit. on p. 40).

[134] Y. Yu, Y. Yu, C. Xu, A. Barrette, K. Gundogdu, and L. Cao, "Fundamental limits of exciton-exciton annihilation for light emission in transition metal dichalcogenide monolayers", Phys. Rev. B **93**, 201111 (2016) (cit. on p. 40).

[135] Q. Cui, F. Ceballos, N. Kumar, and H. Zhao, "Transient absorption microscopy of monolayer and bulk WSe_2", ACS Nano **8**, 2970 (2014) (cit. on pp. 40, 47 sq.).

[136] H. Wang, C. Zhang, and F. Rana, "Ultrafast dynamics of defect-assisted electron-hole recombination in monolayer MoS_2", Nano Lett. **15**, 339 (2015) (cit. on p. 40).

[137] T. Yan, S. Yang, D. Li, and X. Cui, "Long valley relaxation time of free carriers in monolayer WSe_2", Phys. Rev. B **95**, 241406 (2017) (cit. on p. 40).

[138] A. Molina-Sánchez, D. Sangalli, L. Wirtz, and A. Marini, "Ab initio calculations of ultrashort carrier dynamics in two-dimensional materials: valley depolarization in single-layer WSe_2", Nano Lett. **17**, 4549 (2017) (cit. on p. 40).

[139] F. Langer, C. P. Schmid, S. Schlauderer, M. Gmitra, J. Fabian, P. Nagler, C. Schüller, T. Korn, P. G. Hawkins, J. T. Steiner, U. Huttner, S. W. Koch, M. Kira, and R. Huber, "Lightwave valleytronics in a monolayer of tungsten diselenide", Nature **557**, 76 (2018) (cit. on p. 40).

[140] R. Wang, B. A. Ruzicka, N. Kumar, M. Z. Bellus, H.-Y. Chiu, and H. Zhao, "Ultrafast and spatially resolved studies of charge carriers in atomically thin molybdenum disulfide", Phys. Rev. B **86**, 045406 (2012) (cit. on p. 40).

[141] L. Wang, C. Xu, M.-Y. Li, L.-J. Li, and Z.-H. Loh, "Unraveling spatially heterogeneous ultrafast carrier dynamics of single-layer WSe_2 by femtosecond time-resolved photoemission electron microscopy", Nano Lett. **18**, 5172 (2018) (cit. on p. 40).

[142] A. G. Cabo, J. A. Miwa, S. S. Grønborg, J. M. Riley, J. C. Johannsen, C. Cacho, O. Alexander, R. T. Chapman, E. Springate, M. Grioni, J. V. Lauritsen, P. D. C. King, P. Hofmann, and S. Ulstrup, "Observation of ultrafast free carrier dynamics in single layer MoS_2", Nano Lett. **15**, 5883 (2015) (cit. on pp. 40, 50).

[143] G. Moody, C. K. Dass, K. Hao, C.-H. Chen, L.-J. Li, A. Singh, K. Tran, G. Clark, X. Xu, G. Berghäuser, E. Malic, A. Knorr, and X. Li, "Intrinsic homogeneous linewidth and broadening mechanisms of excitons in monolayer transition metal dichalcogenides", Nat. Commun. **6**, 8315 (2015) (cit. on p. 40).

[144] C. Ruppert, A. Chernikov, H. M. Hill, A. F. Rigosi, and T. F. Heinz, "The role of electronic and phononic excitation in the optical response of monolayer WS_2 after ultrafast excitation", Nano Lett. **17**, 644 (2017) (cit. on p. 40).

[145] M. Palummo, M. Bernardi, and J. C. Grossman, "Exciton radiative lifetimes in two-dimensional transition metal dichalcogenides", Nano Lett. **15**, 2794 (2015) (cit. on pp. 40, 48).

[146] L. Waldecker, R. Bertoni, H. Hübener, T. Brumme, T. Vasileiadis, D. Zahn, A. Rubio, and R. Ernstorfer, "Momentum-resolved view of electron-phonon coupling in multilayer WSe_2", Phys. Rev. Lett. **119**, 036803 (2017) (cit. on p. 40).

[147] X. Guo, H. Chen, X. Wen, and J. Zheng, "Electron-phonon interactions in MoS_2 probed with ultrafast two-dimensional visible/far-infrared spectroscopy", J. Chem. Phys. **142**, 212447 (2015) (cit. on p. 40).

[148] M. Trushin, "Theory of thermionic emission from a two-dimensional conductor and its application to a graphene-semiconductor Schottky junction", Appl. Phys. Lett. **112**, 171109 (2018) (cit. on pp. 42 sq.).

[149] L. D. Landau and E. M. Lifshitz, *Quantum mechanics: non-relativistic theory* (Butterworth-Heinemann, Oxford, 2004) (cit. on pp. 42 sq.).

[150] R. Coehoorn, C. Haas, J. Dijkstra, C. J. F. Flipse, R. A. de Groot, and A. Wold, "Electronic structure of $MoSe_2$, MoS_2, and WSe_2. I. Band-structure calculations and photoelectron spectroscopy", Phys. Rev. B **35**, 6195 (1987) (cit. on p. 43).

[151] J. Kang, S. Tongay, J. Zhou, J. Li, and J. Wu, "Band offsets and heterostructures of two-dimensional semiconductors", Appl. Phys. Lett. **102**, 012111 (2013) (cit. on p. 43).

[152] A. Ramasubramaniam, "Large excitonic effects in monolayers of molybdenum and tungsten dichalcogenides", Phys. Rev. B **86**, 115409 (2012) (cit. on p. 43).

[153] D. Y. Qiu, F. H. da Jornada, and S. G. Louie, "Optical spectrum of MoS_2: many-body effects and diversity of exciton states", Phys. Rev. Lett. **111**, 216805 (2013) (cit. on p. 43).

[154] Y. Ding, Y. Wang, J. Ni, L. Shi, S. Shi, and W. Tang, "First principles study of structural, vibrational and electronic properties of graphene-like MX_2 (M=Mo, Nb, W, Ta; X=S, Se, Te) monolayers", Physica B **406**, 2254 (2011) (cit. on p. 45).

[155] A. Molina-Sánchez and L. Wirtz, "Phonons in single-layer and few-layer MoS_2 and WS_2", Phys. Rev. B **84**, 155413 (2011) (cit. on p. 45).

[156] L. Wang, Z. Wang, H.-Y. Wang, G. Grinblat, Y.-L. Huang, D. Wang, X.-H. Ye, X.-B. Li, Q. Bao, A.-S. Wee, S. A. Maier, Q.-D. Chen, M.-L. Zhong, C.-W. Qiu, and H.-B. Sun, "Slow cooling and efficient extraction of C-exciton hot carriers in MoS_2 monolayer", Nat. Commun. **8**, 13906 (2017) (cit. on p. 47).

[157] D. Yadav, F. Pauly, and M. Trushin, "Charge carrier thermalization in bulk and monolayer cdte: a first principles study", arXiv:1910.05216 (cit. on p. 51).

[158] F. Wald, "Applications of cdte. a review", Rev. Phys. Appl. **12**, 277 (1977) (cit. on p. 51).

[159] J. Britt and C. Ferekides, "Thin-film CdS/CdTe solar cell with 15.8% efficiency", Appl. Phys. Lett. **62**, 2851 (1993) (cit. on p. 51).

[160] S. Ithurria, M. D. Tessier, B. Mahler, R. P. S. M. Lobo, B. Dubertret, and A. L. Efros, "Colloidal nanoplatelets with two-dimensional electronic structure", Nat. Mater. **10**, 936 (2011) (cit. on p. 51).

[161] R. B. Vasiliev, E. P. Lazareva, D. A. Karlova, A. V. Garshev, Y. Yao, T. Kuroda, A. M. Gaskov, and K. Sakoda, "Spontaneous folding of CdTe nanosheets induced by ligand exchange", Chem. Mater. **30**, 1710 (2018) (cit. on p. 51).

[162] J. S. Son, X.-D. Wen, J. Joo, J. Chae, S.-I. Baek, K. Park, J. H. Kim, K. An, J. H. Yu, S. G. Kwon, S.-H. Choi, Z. Wang, Y.-W. Kim, Y. Kuk, R. Hoffmann, and T. Hyeon, "Large-scale soft colloidal template synthesis of 1.4 nm thick CdSe nanosheets", Angew. Chem., Int. Ed. Engl. **48**, 6861 (2009) (cit. on p. 51).

[163] P. Heeyeon, C. Haegeun, and K. Woong, "Synthesis of ultrathin wurtzite ZnSe nanosheets", Mater. Lett. **99**, 172 (2013) (cit. on p. 51).

[164] H. Zheng, X.-B. Li, N.-K. Chen, S.-Y. Xie, W. Q. Tian, Y. Chen, H. Xia, S. B. Zhang, and H.-B. Sun, "Monolayer II-VI semiconductors: a first-principles prediction", Phys. Rev. B **92**, 115307 (2015) (cit. on p. 52).

[165] J. Wang, J. Meng, Q. Li, and J. Yang, "Single-layer cadmium chalcogenides: promising visible-light driven photocatalysts for water splitting", Phys. Chem. Chem. Phys. **18**, 17029 (2016) (cit. on p. 52).

[166] E. Unsal, R. T. Senger, and H. Sahin, "Stable monolayer α-phase of CdTe: strain-dependent properties", J. Mater. Chem. C **5**, 12249 (2017) (cit. on p. 52).

[167] M. Osada and T. Sasaki, "Two-dimensional dielectric nanosheets: novel nanoelectronics from nanocrystal building blocks", Adv. Mater. **24**, 210 (2012) (cit. on p. 52).

[168] E. Bianco, S. Butler, S. Jiang, O. D. Restrepo, W. Windl, and J. E. Goldberger, "Stability and exfoliation of germanane: a germanium graphane analogue", ACS Nano **7**, 4414 (2013) (cit. on p. 52).

[169] H. Liu, A. T. Neal, Z. Zhu, Z. Luo, X. Xu, D. Tománek, and P. D. Ye, "Phosphorene: an unexplored 2d semiconductor with a high hole mobility", ACS Nano **8**, 4033 (2014) (cit. on p. 52).

[170] X. Li, D. Xie, H. Park, M. Zhu, T. H. Zeng, K. Wang, J. Wei, D. Wu, J. Kong, and H. Zhu, "Ion doping of graphene for high-efficiency heterojunction solar cells", Nanoscale **5**, 1945 (2013) (cit. on p. 52).

[171] M. Bernardi, M. Palummo, and J. C. Grossman, "Extraordinary sunlight absorption and one nanometer thick photovoltaics using two-dimensional monolayer materials", Nano Lett. **13**, 3664 (2013) (cit. on p. 52).

[172] M. Shanmugam, C. A. Durcan, and B. Yu, "Layered semiconductor molybdenum disulfide nanomembrane based Schottky-barrier solar cells", Nanoscale **4**, 7399 (2012) (cit. on p. 52).

[173] H. Ma, Z. Jin, G. Ma, W. Liu, and S. H. Tang, "Photon energy and carrier density dependence of spin dynamics in bulk CdTe crystal at room temperature", Appl. Phys. Lett. **94**, 241112 (2009) (cit. on pp. 52, 57).

[174] P. Nahàlkovà, P. Němec, D. Sprinzl, E. Belas, P. Horodyskỳ, J. Franc, P. Hlìdek, and P. Malỳ, "Spin dynamics in bulk CdTe at room temperature", Mater. Sci. Eng., B **126**, 143 (2006) (cit. on pp. 52, 57).

[175] H. Ma and J. Leng, "Ultrafast electron spin dynamics in bulk CdTe investigated by femtosecond pump-probe reflection spectroscopy", Phys. Lett. A **377**, 1974 (2013) (cit. on pp. 52, 57).

[176] X. He, N. Punpongjareorn, C. Wu, I. A. Davydov, and D.-S. Yang, "Ultrafast carrier dynamics of CdTe: surface effects", J. Phys. Chem. C **120**, 9350 (2016) (cit. on p. 52).

[177] H. M. Tütüncü, R. Miotto, and G. P. Srivastava, "Phonons on II-VI (110) semiconductor surfaces", Phys. Rev. B **62**, 15797 (2000) (cit. on p. 52).

[178] A. A. Mostofi, J. R. Yates, G. Pizzi, Y.-S. Lee, I. Souza, D. Vanderbilt, and N. Marzari, "An updated version of Wannier90: a tool for obtaining maximally-localised Wannier functions", Comput. Phys. Commun. **185**, 2309 (2014) (cit. on p. 53).

[179] R. J. Nelmes and M. I. McMahon, *Semiconductors and semimetals*, Vol. 54 (Academic Press, San Diego, 1998), pp. 145–246 (cit. on p. 53).

[180] Y. Sun, Z. Sun, S. Gao, H. Cheng, Q. Liu, J. Piao, T. Yao, C. Wu, S. Hu, S. Wei, and Y. Xie, "Fabrication of flexible and freestanding zinc chalcogenide single layers", Nat. Commun. **3**, 1057 (2012) (cit. on p. 53).

[181] F. Iyikanat, B. Akbali, J. Kang, T. Senger, Y. Selamet, and H. Sahin, "Stable ultra-thin CdTe crystal: a robust direct gap semiconductor", J. Phys.: Condens. Matter **29**, 485302 (2017) (cit. on pp. 53 sq.).

[182] S. Lalitha, S. Z. Karazhanov, P. Ravindran, S. Senthilarasu, R. Sathyamoorthy, and J. Janabergenov, "Electronic structure, structural and optical properties of thermally evaporated CdTe thin films", Phys. B (Amsterdam, Neth.) **387**, 227 (2007) (cit. on p. 54).

[183] A. D. Corso, S. Baroni, R. Resta, and S. de Gironcoli, "*Ab-initio* calculation of phonon dispersions in II-VI semiconductors", Phys. Rev. B **47**, 3588 (1993) (cit. on p. 54).

[184] P. Ščajev, S. Miasojedovas, A. Mekys, D. Kuciauskas, K. G. Lynn, S. K. Swain, and K. Jarašiūnas, "Excitation-dependent carrier lifetime and diffusion length in bulk CdTe determined by time-resolved optical pump-probe techniques", J. Appl. Phys. **123**, 025704 (2018) (cit. on p. 55).

[185] E. Mooser and M. Schlüter, "The band-gap excitons in gallium selenide", Il Nuovo Cim. B (1971-1996) **18**, 164 (1973) (cit. on pp. 59, 63).

[186] M. Schlüter, "The electronic structure of gase", Il Nuovo Cimento B (1971-1996) **13**, 313–360 (1973) (cit. on p. 59).

[187] Y. Tang, K. C. Mandal, J. A. McGuire, and C. W. Lai, "Layer- and frequency-dependent second harmonic generation in reflection from gase atomic crystals", Phys. Rev. B **94**, 125302 (2016) (cit. on p. 59).

[188] S. Lei, L. Ge, Z. Liu, S. Najmaei, G. Shi, G. You, J. Lou, R. Vajtai, and P. M. Ajayan, "Synthesis and photoresponse of large gase atomic layers", Nano Letters **13**, 2777–2781 (2013) (cit. on p. 59).

[189] D. J. Late, B. Liu, H. S. S. R. Matte, C. N. R. Rao, and V. P. Dravid, "Rapid characterization of ultrathin layers of chalcogenides on sio2/si substrates", Advanced Functional Materials **22**, 1894–1905 (2012) (cit. on p. 59).

[190] V. Capozzi, L. Pavesi, and J. L. Staehli, "Exciton-carrier scattering in gallium selenide", Phys. Rev. B **47**, 6340–6349 (1993) (cit. on p. 59).

[191] R. Le Toullec, N. Piccioli, and J. C. Chervin, "Optical properties of the band-edge exciton in gase crystals at 10 k", Phys. Rev. B **22**, 6162–6170 (1980) (cit. on p. 59).

[192] D. Andres-Penares, A. Cros, J. P. Martınez-Pastor, and J. F. Sánchez-Royo, "Quantum size confinement in gallium selenide nanosheets: band gap tunability versus stability limitation", Nanotechnology **28**, 175701 (2017) (cit. on p. 60).

[193] D. V. Rybkovskiy, A. V. Osadchy, and E. D. Obraztsova, "Transition from parabolic to ring-shaped valence band maximum in few-layer gas, gase, and inse", Phys. Rev. B **90**, 235302 (2014) (cit. on pp. 60 sq.).

[194] T. Cao, Z. Li, and S. G. Louie, "Tunable magnetism and half-metallicity in hole-doped monolayer gase", Phys. Rev. Lett. **114**, 236602 (2015) (cit. on p. 60).

[195] X. Deng and L. Santos, "Entanglement spectrum of one-dimensional extended bose-hubbard models", Phys. Rev. B **84**, 085138 (2011) (cit. on p. 60).

[196] T. Winzer, E. Mali ć, and A. Knorr, "Microscopic mechanism for transient population inversion and optical gain in graphene", Phys. Rev. B **87**, 165413 (2013) (cit. on p. 60).

[197] G. Antonius, D. Y. Qiu, and S. G. Louie, "Orbital symmetry and the optical response of single-layer mx monochalcogenides", Nano Lett. **18**, 1925 (2018) (cit. on pp. 60, 63).

[198] X. Li, M.-W. Lin, A. A. Puretzky, J. C. Idrobo, C. Ma, M. Chi, M. Yoon, C. M. Rouleau, I. I. Kravchenko, D. B. Geohegan, and K. Xiao, "Controlled vapor phase growth of single crystalline, two-dimensional gase crystals with high photoresponse", Sci. Rep. **4**, 5497 (2014) (cit. on pp. 60 sq.).

[199] P. Rudolph, "Fundamental studies on bridgman growth of cdte", Prog. Cryst. Growth Charact. Mater **29**, 275 (1994) (cit. on p. 60).

[200] P. Li and I. Appelbaum, "Symmetry, distorted band structure, and spin-orbit coupling of group-iii metal-monochalcogenide monolayers", Phys. Rev. B **92**, 195129 (2015) (cit. on p. 63).

[201] O. Madelung, *Semiconductors: data handbook* (Springer, 1993) (cit. on p. 63).

[202] M. Trushin, "Tightly bound excitons in two-dimensional semiconductors with a flat valence band", Phys. Rev. B **99**, 205307 (2019) (cit. on p. 63).